Online Active Condition Monitoring of Power Equipment Using Natural Power Disturbances

By

Xi Wang

A thesis submitted in partial fulfillment of the requirements for the degree of

Doctor of Philosophy
in
Energy Systems

Department of Electrical and Computer Engineering
University of Alberta

Abstract

Power equipment condition monitoring is an important practice of utility companies. It helps to prevent unexpected outages of power systems and reduces maintenance costs. There are two general approaches to condition monitoring: passive and active. Passive condition monitoring is conducted by detecting abnormal signals generated by the equipment of interest. This approach is reactive since it waits for abnormal equipment conditions to occur. Active condition monitoring is conducted by injecting a test signal and analyzing the equipment response. It is a proactive approach. However, due to its intrusive nature, active condition monitoring can only be performed occasionally in an offline mode, and it involves high costs.

The proposed Ph.D. research aims to transform active condition monitoring from offline to online. This is achieved by utilizing natural power disturbances as the test signals. The proposed approach has the potential to enable frequent and automatic testing of equipment once the monitoring system is set up. In addition, the statistical trends of equipment responses under repetitive tests will provide a much more accurate picture of equipment conditions. In this research, the proposed concept is applied to solving two challenging problems: substation grounding grid condition monitoring and open conductor detection.

This thesis presents two online methods for monitoring the substation grounding grid impedance and thus revealing the conditions of the substation grounding grid. Natural disturbances in the form of a ground-fault current and a 3rd harmonic current are used as test signals, respectively. Both methods' performance and effectiveness are demonstrated through analytical studies and extensive verification, sensitivity, and application studies. This thesis further presents two online schemes to detect the open conductor condition in power plants. Natural voltage sag disturbance and 3rd

harmonic power are used as test signals, respectively. The performance and practicability of both methods have been demonstrated using simulation and experimental studies. These two methods can work individually or in a parallel way to increase the effectiveness and reliability of the open conductor detection.

The power-disturbance-based condition monitoring concept as presented in this thesis has the potential to transform many offline, intrusive condition monitoring methods into online automatic condition monitoring methods, thus creating a new opportunity to improve the “smartness” of power equipment and power systems.

Preface

Chapter 2 of this thesis has been published as two journal articles:

- **X. Wang**, J. Yong, and W. Xu, "An online method for monitoring substation grounding grid impedances - Part I: Methodology," *IEEE Transactions on Power Delivery*, Accepted for publication (Early Access Online).

- **X. Wang**, J. Yong, and W. Xu, "An online method for monitoring substation grounding grid impedances - Part II: Verifications and applications," *IEEE Transactions on Power Delivery*, Accepted for publication (Early Access Online).

Chapter 4 of this thesis has been published as two journal articles:

- **X. Wang**, T. Ding, and W. Xu, "An open conductor condition monitoring scheme using natural voltage and current disturbances," *IEEE Transactions on Power Delivery*, vol. 34, no. 3, pp. 1193-1202, Jun. 2019.

- **X. Wang**, and W. Xu, "A 3rd harmonic power based open conductor detection scheme," *IEEE Transactions on Power Delivery*, vol. 36, no. 2, pp. 1041-1050, Apr. 2021.

Acknowledgments

First and foremost, I would like to express my sincere gratitude and appreciation to my supervisor Dr. Wilsun Xu for his guidance, encouragement, and support in the past years. It would not have been possible to complete this thesis without his excellent supervision. His profound knowledge, sharp insight, and enthusiasm for research have always guided my thoughts and analysis and have enabled me to become a mature researcher. I will always be indebted to him, and I will always be proud to say that I had the privilege of being his student.

I would also like to sincerely thank the other professors from my Ph.D. examining committee, Dr. Hao Liang and Dr. Venkata Dinavahi, for reviewing my thesis and providing valuable comments.

I also thank all my friends and colleagues in the PDS-LAB for their help and company. Special thanks go to Dr. Jing Yong for her generous assistance during various stages of my Ph.D. program.

I cannot express how much the support of my family means to me, especially that of my parents, Degui Wang and Shudong Yin, whose devotion and endless love are visible in all my accomplishments to date. I owe them a massive debt of gratitude. This appreciation also extends to my parents-in-law, Tiecheng Lin and Xiulan Fu, whose kindness has been a source of motivation for me. I thank my wife, Nan Lin, and two lovely children, Yonghao and Isabella, for their encouragement, support, and company in this academic pursuit in Canada.

Table of Contents

List of Tables

List of Figures

Chapter 1: Introduction

Power equipment must operate appropriately for power system reliability and personnel safety. However, some power equipment, especially aging equipment, may work with abnormalities. These undetected abnormalities may result in power equipment damage, which may escalate into a wide range of failures of power systems. For example, a report showed that a failing coupling capacitor voltage transformer (CCVT) exploded and sent shrapnel yards away, causing other equipment failures [1]. Thus, condition monitoring has been widely performed to detect abnormalities within power equipment and prevent adverse consequences. In fact, there is an industry trend towards using online equipment condition information to provide essential recommendations on operation actions and asset management. A new product embodying this idea is Siemens's Integrated Substation Condition Monitoring (ISCM) system [2].

Condition monitoring is generally performed in two ways: passively and actively. Passive condition monitoring is performed by detecting abnormal signatures generated by the equipment of interest. Some unique signatures can be extracted in the current and voltage waveforms before permanent failures so that the corresponding abnormalities within power equipment are monitored. Typical examples are the detections of sub-cycle and multi-cycle incipient faults to signal that the power cable's permanent failure is approaching [3, 4]. More examples of passive condition monitoring applications for different power equipment are presented in Table1.1. In recent years, the potential of passive condition monitoring has been further explored due to the availability of synchronized waveform data [5]. However, passive condition monitoring is reactive, i.e., it waits for abnormal signals from the equipment. It could be too late for equipment failure prevention by the time when abnormal signatures are successfully captured and confidently confirmed.

Active condition monitoring is conducted by injecting a test signal and receiving an associated response or responses. The test signal and response are then jointly analyzed to develop an indicator whose critical change could indicate the condition of the power equipment. A typical example is the cable voltage withstand test [6]. A test voltage higher than the nominal is applied on a power cable, and the partial discharge signals produced are chosen as the responses to indicate the cable's condition. More examples of active condition monitoring applications for different

power equipment are presented in Table 1.1 [7-11]. Artificial test signals are used in particular for different applications. Active condition monitoring has unique and irreplaceable applications, and it can provide valuable information in comparison with passive condition monitoring. However, active condition monitoring can only be performed occasionally in an offline mode due to its intrusive nature. The de-energization of the power equipment under assessment may be required, which strongly discourages utilities from performing active condition monitoring. In addition, active condition monitoring is conducted by skilled maintenance crews. As a result, active condition monitoring is very costly. Therefore, active condition monitoring is typically performed on new equipment and regularly on operating equipment at long time intervals. More importantly, it is often too late, as power equipment may have been damaged between two rounds of tests [12]. In view of the performance advantage but usage limitation of active condition monitoring, there is strong interest in improving active condition monitoring techniques.

Table 1.1 Examples of passive and active condition monitoring applications for different power equipment

Power equipment	Testing content	Passive condition monitoring	Active condition monitoring	
			Indicators	**Artificial test signals**
Cable	Insulation degradation	Partial discharge signals generated by the operating voltage	Dissipation factor (Tan Delta)	Voltage of very low frequencies (0.01Hz to 1Hz) and in $1.5V_0$*
Transformer	Winding deformation	Not available	Short circuit inductance or transfer admittance function	Voltage of a varying frequency
Substation grounding grid	Grounding condition	Not available	Grounding resistance	Current of power frequency or certain frequencies
Capacitor	Insulation degradation	Leakage current generated by the operating voltage	Capacitance or equivalent series resistance (ESR)	Voltage of certain frequencies

* $\boldsymbol{V_0}$ is the nominal voltage of the cable under test

This Ph.D. research aims to transform active condition monitoring from occasional offline assessment to continuous online monitoring. The idea is to use natural power disturbances as the test signals. Natural power disturbances are the voltage/current waveform changes caused by various regular or unexpected events in power systems, such as short-circuit faults or equipment

energizations. This is an important strategy to overcome the disadvantages of the traditional active condition monitoring methods while maintaining their advantages [5]. Online monitoring can perform more effectively and cost-efficiently since it can generate an indicator frequently and automatically. The statistical trend provides a much more accurate picture of the condition of the equipment than a single change of the indicator. The proposed power-disturbance-based condition monitoring approach will increase the awareness of equipment conditions, reduce the risk of equipment failure, and improve the reliability of power systems.

1.1 The Concept of Power-Disturbance-Based Condition Monitoring

Power-disturbance-based condition monitoring can generally be described using the diagram in Figure 1.1. Typically, a natural power disturbance such as a short circuit fault caused large current is generated somewhere in the system. This disturbance may transmit to the power equipment of interest. Since the power disturbance has an electrical impact on the equipment, it can be used as a test signal. Multiple equipment responses associated with this test signal are recorded and stamped with precision time tags. The measurements of power disturbances and equipment responses at different locations are transmitted to a processing unit via a communication network and then jointly analyzed to draw a conclusion on the condition of the equipment. The main components of the proposed approach are explained as follows.

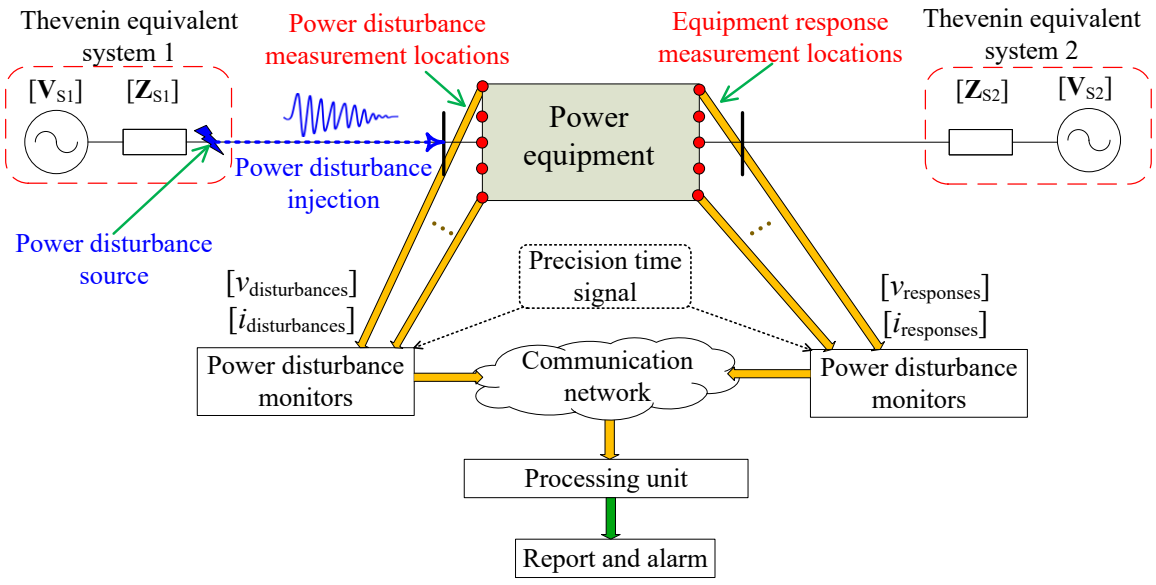

Figure 1.1 Illustration of power-disturbance-based condition monitoring

- **Natural power disturbance:** natural power disturbances refer to electrical disturbances naturally existing in power systems. They are produced by various regular and unexpected events at different locations in the power systems. Examples are voltage/current transients caused by faults, energizations, switching activities and so on. Power disturbances manifest as deviations, which can be in transient and steady-state, from steady-state power-frequency voltage/current waveforms. For example, when a short-circuit fault occurs on a feeder, it results in a voltage sag on the distribution bus. Such a voltage sag is a typical power disturbance. Natural power disturbances are quite common in the power systems, and they have been intensively studied involving classification, detection, and measurement [13].

- **Power disturbance monitor:** the power disturbance monitor refers to a device with synchronized measurement capability, such as a digital fault recorder, digital relay, power quality monitor, and dedicated condition monitor. The locations, types, and numbers of the power disturbance monitors are application/case-dependent. Such devices record voltage and current waveforms that contain disturbances. The sampling rate is application/case-dependent, with a rate of 64 samples/cycle is commonly seen.

- **Precision time signal:** the precision time information is assigned to each measurement data at the power disturbance monitors. As a result, all the measurements of power disturbances and equipment responses at different locations can be synchronized. Several methods are available to obtain the precision time information [14-20]. Generally, substation clock signals such as Inter-Range Instrumentation Group (IRIG)-B and Precision Time Protocol (PTP) are preferable if all power disturbance monitors are within one power facility such as a substation. The GPS-timestamping is useful if some monitors are located outside the substations.

- **Communication network:** a communication network is needed to transmit the measurement data at different locations to a central location for processing by the processing unit. If all monitors are inside a substation, substation Ethernet is sufficient for this purpose. If the monitors are located at different substations or outside the substations, the synchronous optical network (SONET), cellular and other communication networks could be used. Since condition monitoring does not require immediate actions, real-time transmission and processing of the

data at a central location are not necessary [5]. As a result, the requirement for communication networks is not very stringent.

- **Processing unit:** a processing unit is used to collect and synchronize the measurement data from all power disturbance monitors. The processing of the data is completed according to the algorithms developed to achieve different condition monitoring functions. This unit can also be designed to have data storage, reporting, and other necessary functions. Multiple processing units of different condition monitoring functions could be combined into one unified unit, such as Siemens's Assetguard MVC [21].

The proposed approach transforms active condition monitoring from offline with occasional tests to online with continuous monitoring. Thus, it has significant advantages. First, it shortens the testing interval and increases the abnormality detection rate. Second, it does not interrupt the operations of power equipment and power systems since the monitored equipment does not need to be de-energized. More importantly, it can address some challenges that both passive and active condition monitoring are ineffective to solve. Cost efficiency is another advantage. The proposed power-disturbance-based condition monitoring approach requires neither specialized monitoring devices nor manual work from skilled workers once the setup is done. Instead, it performs online active condition monitoring through the data collected by power disturbance monitors, which in many cases may already be deployed for other applications.

1.2 Research Topics

This Ph.D. research aims to develop online active condition monitoring methods using natural power disturbances for two subjects: substation grounding grid condition monitoring and open conductor detection. Literature reviews on the existing techniques and the motivations of both research topics are presented in this section.

1.2.1 Substation Grounding Grid Condition Monitoring

A grounding grid is an essential component of a substation. It supports the operation of substation equipment by providing proper ground potential and serves as an essential means to protect personnel safety. Unfortunately, a grounding grid can deteriorate over time due to corrosion, aging,

vandalism, and other factors. As a result, utility companies need to evaluate the grounding grid conditions of their substations regularly.

Accordingly, a lot of research has been conducted to develop substation grounding grid condition monitoring techniques [22-48]. The majority of the methods, such as the far-away method [31-38] and the fall-of-potential method [39-46], target the measurement of the grounding grid impedance. It has been reasoned that such an impedance can reveal, indirectly, the condition of the grounding grid. If unusual impedances are observed, detailed and costly diagnostics such as touch and step voltages testing and grounding grid integrity testing are then pursued [22, 49].

In grounding impedance measurement, a current is injected into the substation grounding grid and the resulting Ground Potential Rise (GPR) of the grid is measured using auxiliary electrodes (i.e., current electrode and potential electrode), as illustrated in Figure 1.2. The grounding impedance is estimated by calculating the ratio of the measured GPR to the injected current.

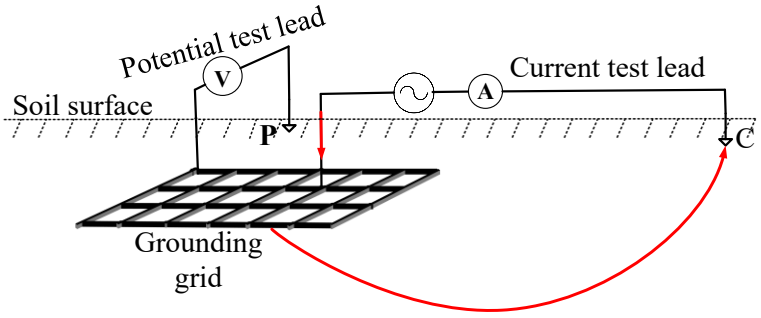

Figure 1.2 Illustration of grounding impedance measurement setup

As is further shown in Figure 1.2, the success of the measurement requires an elaborate setup:

- A dedicated power source is indispensable for injecting a test current and generating a GPR.
- A current electrode is needed to collect the return current. It should be at a substantial distance away from the grounding grid. This requirement aims to ensure the current flows through the grounding grid and into the deep soil.
- A potential electrode is needed to provide a reference for the GPR measurement. It should be placed at a location of zero soil potential. This location can be obtained at the remote earth or

at a specific point between the grounding grid and the current electrode, as shown in Figure 1.3.

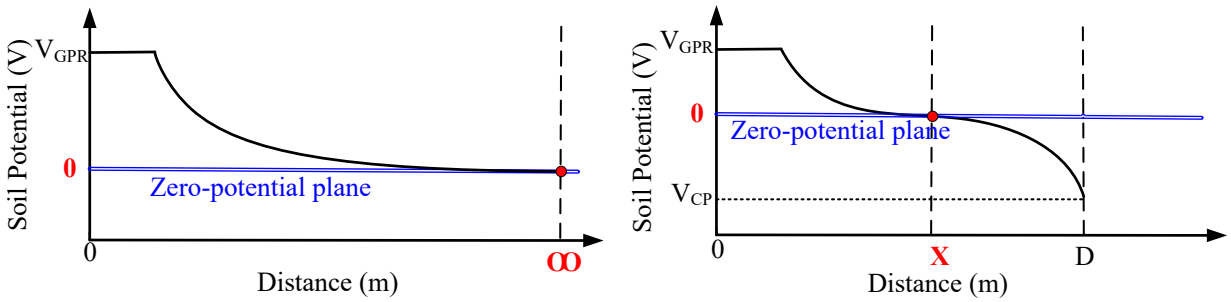

(a) Remote earth (b) A specific point

Figure 1.3 Examples of zero soil potential locations

Depending on how to locate the potential electrode, the existing methods of grounding impedance measurement can be mainly categorized into two major streams: the far-away method and the fall-of-potential method. The far-away method achieves the zero potential point at the remote earth, as shown in Figure 1.3(a). The remote earth is determined by trying different distances to find a point beyond which the measured impedance no longer varies. Thus, this method requires a very long test lead, and it is time-consuming and laborious. In comparison, the fall-of-potential method gets a specific zero potential point between the tested grounding grid and the current electrode, as demonstrated in Figure 1.3(b). Specifically, a zero potential point was first found at 61.8% away from the center of the grounding grid, known as the 0.618 method [39, 40]. The angle offset method [42] further expends this single point to a closed curve. These findings assume hemispherical electrodes and uniform soil [22, 50]. A computer-aid method [44] was proposed to find an exact zero potential point to locate the potential electrode by calculating the potential distribution at the soil surface via computer simulation studies.

Many improvements have been made to improve the methods' accuracy and reliability in terms of eliminating the inductive interference of the test current and background noise [47, 48, 51, 52]. The improvements require more complicated measurement setups and operation procedures.

It can be concluded from the above literature review that almost all the existing techniques are offline types, i.e., they require elaborate manual setup by specialists and can only be performed

occasionally. Surveys have shown that the typical testing intervals are five to ten years for utilities in North America [49, 53]. If a substation is in a crowded area, there are also considerable difficulties in conducting the measurement due to space constraints. Moreover, grounding impedance is dependent on not only grounding grid conditions but also on the soil resistivity that can be affected by various factors, such as temperature, weather, and season at the moment of testing [54, 55]; therefore, the results obtained through occasional measurements described above are insufficient to reveal the true condition of a grounding grid in a timely manner. This situation motivates researchers to develop online methods to monitor substation grounding grid conditions continuously and automatically.

1.2.2 Open Conductor Detection

An open conductor is an abnormal operating condition in which one of the three-phase conductors is open. Undetected open conductor conditions expose power plants to a potentially risky situation that may develop into a severe failure. One representative example is Exelon's Byron Nuclear Station incident in 2012 [56]. An open conductor made the reactor coolant pump motors unable to start when required, which resulted in the shutdown of Unit 2 at the nuclear station. The open conductor condition shown in Figure 1.4 has occurred in many conventional and nuclear power plants, and detecting the open conductor condition involving the backup system has become an essential requirement, especially for nuclear power plants [57, 58]. There have also been incidents where an open conductor condition has affected the operation of distributed generators [59, 60]. IEEE Standard 1547-2018 has also established a requirement for detecting the open conductor condition [61].

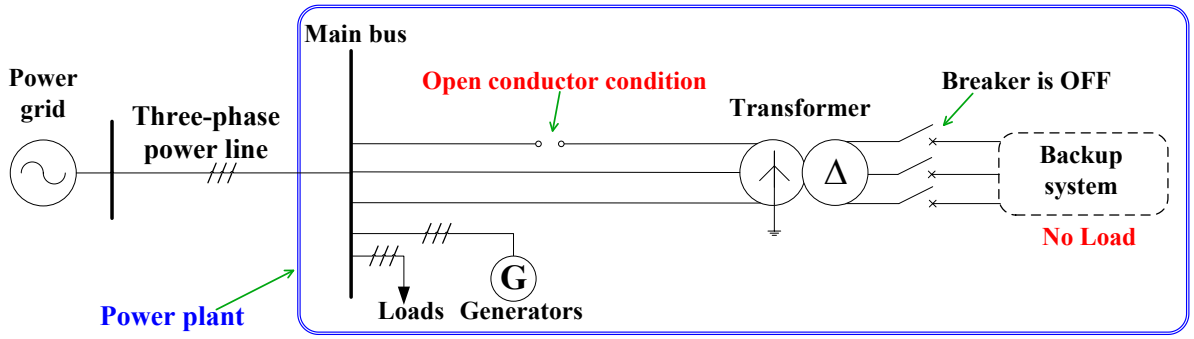

Figure 1.4 Description of the open conductor problem in power plants

Detecting the open conductor condition described in Figure 1.4 is especially difficult because it causes no apparent current and voltage abnormalities. Specifically, the phase current is almost zero since the transformer supplies no load. Moreover, such a transformer can recreate a "normal" voltage on the open phase through electrical or electromagnetic coupling from the two intact phases [62]. As a result, conventional current- and voltage-based open-phase detection methods are ineffective [63-65]. To solve this problem, General Electric (GE) proposes a solution to use high-accuracy optical CTs installed at the primary side of the transformer to differentiate the "expected" low magnetizing current on the opened phase from normal magnetizing currents on the two intact phases. The performance of this solution was further tested from field experiments not very desirable due to the influence of the measurement error of CTs and the capacitive coupling between the three-phase conductors, considering normal magnetizing currents can be as low as a few tens of milliamps [66]. In recent years, Electric Power Research Institute (EPRI) has conducted a series of research to solve this problem, but the methods proposed so far are not very desirable [67, 68]. The first of EPRI's methods suggests monitoring the 1^{st}, 3^{rd}, 5^{th}, and other harmonic components in the transformer neutral current and using the change of dominant components to indicate the open conductor condition. However, the technical justifications behind this method are not clear. The threshold is difficult to set since the measured harmonics could be affected by other factors such as harmonic resonance. As a result, it is difficult to conclude whether this approach would be applicable to many other cases. The second of EPRI's methods is to apply a voltage source at the transformer neutral and measure the corresponding excited current. The open conductor condition is detected if the current is low. This method is expensive and complex as it requires an additional voltage source. This unsatisfactory situation shows a need for researchers to develop effective and practical open conductor detection schemes.

1.3 Thesis Scope and Outline

The scope of this thesis is to establish the concept of power-disturbance-based condition monitoring by developing multiple condition monitoring methods for different types of power equipment. Specifically, the thesis aims to solve the substation grounding grid condition monitoring and open conductor detection problems described in the previous section.

This thesis is divided into two main parts. The first part concentrates on substation grounding grid condition monitoring and is presented in Chapters 2 and 3. The second part focuses on the open conductor detection problem, and the findings are presented in Chapter 4. The individual chapters are organized as follows.

Chapter 2 presents an online method for monitoring the substation grounding impedance and thus the substation grounding grid conditions. The proposed method continuously and automatically monitors the substation grounding impedance using natural fault currents. The trend of the impedance change can be observed, providing much more reliable information on the substation grounding grid conditions than that provided by offline methods. The idea, algorithm, and setup of the proposed method are explained. Extensive verification, sensitivity, and application studies are conducted to prove the feasibility and effectiveness of the method using industrial data. A guide for the implementation and operation of the proposed method is presented.

Chapter 3 presents an improved method over that presented in Chapter 2. The new method uses a novel test lead consisting of multiple measuring wires, permanently installed in a transmission line corridor or on a distribution feeder, to eliminate the inductive and soil potential interferences in the GPR measurement. In addition, by utilizing the 3^{rd} harmonic current as test signals, the method can estimate the substation grounding grid impedance at short time intervals. The proposed improvements also make it possible to monitor transmission and distribution substations that contain transformers with all types of winding connections.

Chapter 4 begins by explaining why an open conductor condition in power plants fails to be detected by all the existing methods, thus resulting in significant consequences and losses. Two power-disturbance-based detection methods using natural voltage disturbances and 3^{rd} harmonic power, respectively, are proposed to address this challenging issue. Good performance by both methods is proved using extensive simulation and experimental studies. Implementation and practical considerations are discussed so that both methods may be developed into applicable schemes. These two methods can work individually or in a parallel way to increase the effectiveness and reliability of the detection.

Chapter 5 concludes the thesis, highlights its contributions and provides suggestions for future research.

Chapter 2: Substation Grounding Grid Condition Monitoring Using Natural Fault Currents

This chapter presents the initial research completed for the substation grounding grid condition monitoring topic identified in Chapter 1. Through this research, an online method is proposed to monitor the substation grounding impedance and thus the grounding grid conditions. The proposed method utilizes phase-to-ground faults occurring in downstream feeders as the "test current" sources and a specially selected feeder neutral as the electrode for the Ground Potential Rise (GPR) measurement. The measured fault currents and GPRs are used to estimate the substation grounding impedance. Once established, the proposed online method can continuously and automatically monitor the substation grounding impedance. Since short-circuit faults frequently occur in distribution systems, the method can estimate the grounding impedance continuously and thus discover the trend of the grounding impedance change. As a result, the proposed method can yield much more reliable information on the substation grounding grid conditions than that gleaned by offline methods. The proposed online method also overcomes many disadvantages of the offline techniques.

2.1 Substation Grounding Grid

A grounding grid of a substation is an essential component to provide protective functions for the safety of substation equipment and personnel, especially during faults and other contingencies. A substation grounding grid typically comprises numerous square or rectangle metallic grounding conductors, vertical grounding rods, and other auxiliary electrodes such as counterpoises. Such a grounding grid is buried underground the substation in a size of approximately as large as the substation footprint. Figure 2.1 illustrates an example of a simple substation and its grounding grid.

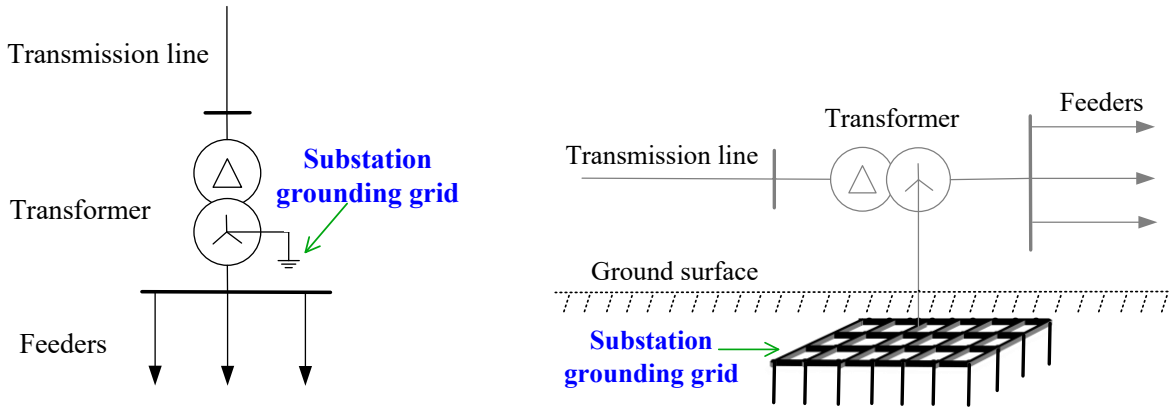

(a) Layout of electrical components (b) Illustration of substation groudning grid

Figure 2.1 An example of a simple substation and its grounding grid

A grounding grid may have external interconnections in substations, such as transmission line shield wires and feeder neutrals. The entire interconnecting grounding structure for a substation is called the substation grounding system. Figure 2.2 shows a representative substation grounding system for distribution substations in North America. Specifically, a substation grounding grid shown in the center is the main component of the substation grounding system. The upstream transmission lines may have shield wires for lightning protection. These shield wires are directly connected to the substation grounding grid. The downstream feeders often have multi-grounded neutrals. The multi-grounding neutrals refer to the neutral wires grounded at multiple points along the feeder. The feeder neutrals are interconnected with the substation transformer neutral, which is grounded to the substation grounding grid. Generally, there are three configurations for feeder neutrals in North American power systems. (1) Some neutrals may be connected to the substation grounding grid, as shown in Feeder 1 in Figure 2.2. This configuration is called the full multi-grounded neutral. (2) Some neutrals may not be connected to the substation grounding grid, as shown in Feeder 2 in Figure 2.2. Such a configuration is called the isolated multi-grounded neutral. (3) A few lightly loaded feeders may have no neutral to save installation costs, such as Feeder 3 in Figure 2.2. Such feeders use earth only as a return path for the zero sequence currents.

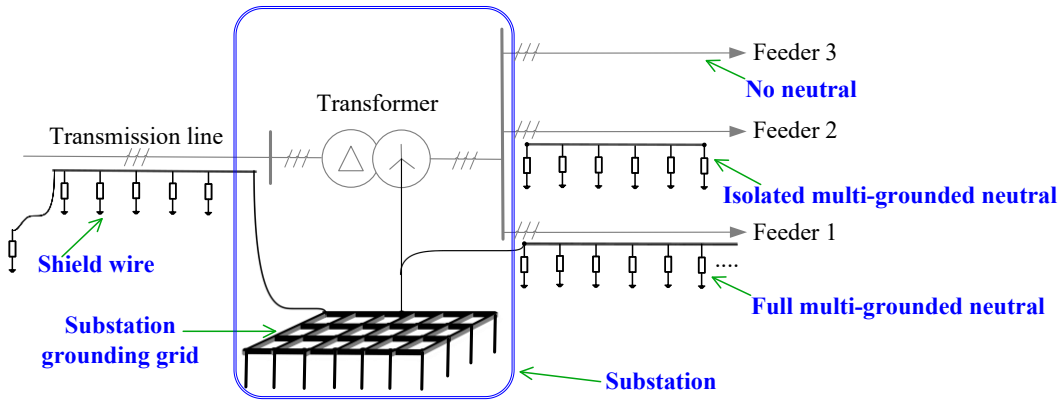

Figure 2.2 Illustration of a typical substation grounding system in North America

The protective capability of a grounding grid is dependent on its conditions. A well-installed and maintained grounding grid creates an effectively low grounding impedance path for the ground current dissipation down to the remote earth. As a result, the maximum Ground Potential Rise (GPR) can be limited within an acceptable range for all possible faults. Moreover, a grounding grid in good condition can reduce the potential difference on the earth's surface in and around the substation and thus eliminate the possible step and touch voltages hazards to personnel safety.

Unfortunately, the condition of a grounding grid can degrade due to various factors such as grid corrosion, conductor discontinuity, and even conductor theft. Corrosion is the most dangerous since it is hard to visualize and predict among all these factors. The corrosion can damage effective connections among conductors in a grounding grid. It would be worsened if critical conductors such as vertical grounding rods were corroded and broken off the grounding grid. The corrosion rate can reach up to 8.0mm per year for the copper grounding grid. The rate would be even faster for the steel grounding grid, which is widely used for economic considerations. Undetected condition degradation or damage of the substation grounding grid may eventually fail the protective functions, resulting in severe consequences such as personnel injury and death.

Therefore, the condition of a substation grounding grid needs to be assessed as frequently as possible throughout its service life. The assessment is done by means of grounding impedance measurement, touch and step voltages testing, and grounding grid integrity testing, depending on the expert judgement of the condition of the grid [22, 23]. In practice, North American utilities periodically conduct the grounding impedance measurement every five to ten years unless a

problem occurs or a substation expansion [49, 53]. Once a large grounding impedance is observed, diagnostic testing of grounding grid integrity and touch and step voltages is then performed at all possible locations in and around the substation to locate the suspected degradation and damage. Only the damaged and corroded parts of the grounding grid will be replaced based on the test results. This industry practice implies a strong need for technologies that can frequently measure the grounding impedance and thus timely confirm the condition of the substation grounding grid.

2.2 The Proposed Online Monitoring Method

The proposed method was conceived based on the following observation. When an unbalanced ground fault occurs in a feeder, a zero sequence fault current flows into the substation grounding grid through substation transformer neutrals, producing a GPR. This current can be treated as the "test current" used in offline methods. Estimating the substation grounding impedance becomes possible if one can measure this current and the corresponding GPR.

2.2.1 Main Idea and Setup of the Proposed Method

The proposed method needs to set up a current loop and a potential loop for current and GPR measurements. The measured data are then processed using a relay-like processing unit installed inside the protection and control cabin of the substation. Figure 2.3 shows the overall setup of the proposed method. The main components of the proposed method are explained as follows.

- **Current Loop:** The feeder experiencing a phase-to-ground fault serves as the current loop. The current loop varies with faulted feeders. However, the "test current" is invariably recorded by a permanently installed current monitor at the transformer neutral, although a portion of the fault current may return through some neutral rods and conductors if the faulted feeder has a neutral. Figure 2.3 illustrates the test current loop without showing actual fault current distributions. A substation typically supplies multiple feeders, and faults may occur on any of them. Consequently, more feeders bring more opportunities for injecting the "test current".

- **Potential Loop:** In North America, the downstream feeders of a substation often have multi-grounded neutrals. One specific multi-grounded neutral (called neutral M) is selected for the proposed method to establish the potential loop. A neutral that does not connect to the

substation grounding grid is not uncommon in North American systems. This is a permanent setup. The GPR is recorded using a voltage monitor installed at the front-end of the neutral in the substation.

- **Synchronized Data Processing:** The current and voltage (i.e., GPR) are measured as sampled waveforms. They are precision timestamped using substation clock signals such as PTP or IRIG-B and then transmitted using substation Ethernet to the processing unit installed in the substation. The current and voltage data from all measurement locations are synchronized based on precision timestamps in the processing unit. This unit extracts the changes of current and voltage caused by the fault and estimates the substation grounding impedance. This device can also be designed to store the measured impedances and to perform trend analysis.

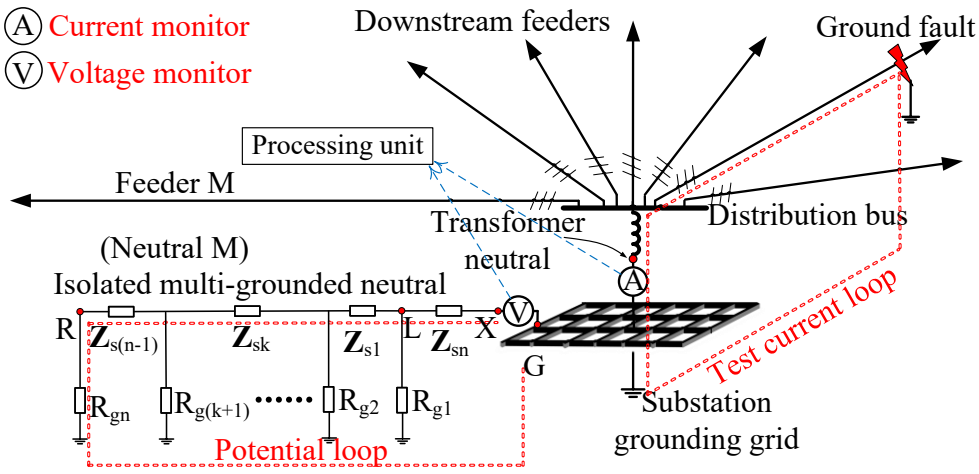

Figure 2.3 Main idea of the proposed online monitoring method

The main advantages of the proposed online method are summarized as follows:

- It takes full advantage of existing facilities, such as using natural faults as the power source of testing, using the faulted feeder as the lead wire for the "test current" injection, and using the isolated multi-grounded neutral to form the GPR measurement loop. Once set up, continuous and automatic monitoring can be achieved.

- It uses the changes of voltage and current during a fault for grounding impedance estimation, thus reducing the interference of background voltages and currents. The large fault current also

enhances the accuracy of the measurements. As a result, more accurate online monitoring becomes possible while the substation continues to operate normally.

- It can produce a large number of estimated impedance results by utilizing frequently occurring faults in multiple feeders and locations. The literature search shows hundreds of ground faults in a single utility's distribution network within three to four years [69, 70]. The continuous repeated measurements reduce the impact of environmental factors on the results and reveal the trend of substation grounding impedance change. Hence, the corrosion of the substation grounding grid in incremental progress can be continuously monitored. Moreover, abrupt changes of the grounding grid conductors due to theft, damage, loss of a detrimental electrode, and any other issues, which are reflected in a considerable increase of substation grounding impedances, can be timely detected.

The proposed method uses an existing multi-grounded neutral for the GPR measurement. If such a neutral does not exist, a dedicated conductor installed along a feeder may be used. Alternatively, the grounded side of a neutralizing transformer (used for communication systems) can also be used.

2.2.2 Algorithm of the Proposed Method

The voltage monitor at the front end of neutral M and the current monitor at the transformer neutral record the voltage and current waveforms before and during the fault. The changes in voltage and current due to the fault can be obtained by subtracting two waveforms as

$$\Delta v(t) = [v_{fault}(t) - v_{prefault}(t - n_0\Delta t)]\,|_{t_0}^{t_0+\Delta t} \tag{2.1}$$

$$\Delta i(t) = [i_{Trn\_fault}(t) - i_{Trn\_prefault}(t - n_0\Delta t)]\,|_{t_0}^{t_0+\Delta t} \tag{2.2}$$

where $\Delta v(t)$ and $\Delta i(t)$ are the extracted fault-caused GPR and transformer neutral current; $v_{prefault}(t - n_0\Delta t)$ and $v_{fault}(t)$ are the measured GPRs before the fault and during the fault steady-state; and $i_{Trn\_prefault}(t - n_0\Delta t)$ and $i_{Trn\_fault}(t)$ are the measured transformer neutral currents before the fault and during the fault steady-state. In (2.1) and (2.2), n_0 is an integer, t_0 is the start point, and Δt is the window length. The window length is selected based

on power frequency, which can be a single cycle or multiple cycles. The window moves from the before-fault waveform to the during-fault waveform.

Then, the Discrete Fourier Transform (DFT) algorithm is applied to find the power frequency components of $\Delta v(t)$ and $\Delta i(t)$. With the help of the synchronization signals, the corresponding phasors of GPR and fault current at power frequency can be obtained. They are denoted as $\bar{V}_{GPR\_measure}$ and $\bar{I}_{test}$.

Finally, the substation grounding impedance $Z_{sys\_measure}$ at power frequency is estimated using

$$Z_{sys\_measure} = \bar{V}_{GPR\_measure} / \bar{I}_{test} \tag{2.3}$$

It is important to notice that the injected current may split into three parts, as shown in Figure 2.4, i.e., the currents passing through the grounding grid $\bar{I}_{grid}$, the shield wires of upstream power lines $\bar{I}_{SW}$ and the feeder neutrals that are connected to the grounding grid $\bar{I}_N$. This suggests that the estimated substation grounding impedance contains the grounding grid impedance Z_{grid}, the grounding impedances of transmission shield wires Z_{SW} and feeder neutrals Z_N in parallel. The true value of this grounding system impedance is denoted as Z_{sys}. The true GPR $\bar{V}_{GPR}$ can be then expressed as $\bar{V}_{GPR} = Z_{sys}\bar{I}_{test}$. Furthermore, one can also have $\bar{V}_{GPR} = Z_{grid}\bar{I}_{grid}$, since the transfer voltages from all the neutral/shield wire rods have negligible impacts on the soil potential at the substation grounding grid. The characteristic of a grounding rod's small zone of influence is concluded and compared with that of a substation grounding grid in Appendix A. The target of the substation grounding grid condition monitoring is the grounding grid, i.e., Z_{grid}. To improve the accuracy, excluding those feeder neutral currents may be necessary if there are many such neutrals. Fortunately, feeder neutrals in North America are often bonded together and then connected to the transformer neutral through one conductor. In this case, an additional current monitor can be installed on this conductor to obtain the synchronized current $\bar{I}_N$. With $\bar{I}_N$ in hand, the substation grounding impedance $Z_{grid\_measure}$ that can better reflect grounding grid conditions can be estimated as

$$Z_{grid\_measure} = \bar{V}_{GPR\_measure} / (\bar{I}_{test} - \bar{I}_N) \tag{2.4}$$

The process to obtain the phasor of $\bar{I}_N$ is the same as that for $\bar{I}_{test}$. This action is not needed for a substation with few or no neutral connections to the grounding grid. For a substation with many neutrals that are not clumped into one conductor, the current on each neutral wire needs to be measured individually using current monitors. The total neutral current $\bar{I}_N$ can be then obtained. Furthermore, the effect of the transfer voltages on neutral rods from the substation grounding grid and the effect of the inductive interference in neutral conductors due to the fault current and any other sources are eliminated by excluding $\bar{I}_N$ in (2.4). Since installing a current monitor on shield wires may not be easy, the estimated substation grounding impedance always includes the grounding impedance of shield wires. Generally, there are only one or two upstream power lines with shield wires for a distribution substation. Moreover, the shield wire tower-footing electrodes (rods) suffer negligible transfer voltages from the substation grounding grid since the transmission line typically has a considerable span length, as seen in Appendix A. The impact of shield wires on the results is limited [50]. It is also the practice of offline measurements not to isolate the shield wires. Thus, the substation grounding impedance can be considered to be the results calculated using either (2.3) or (2.4).

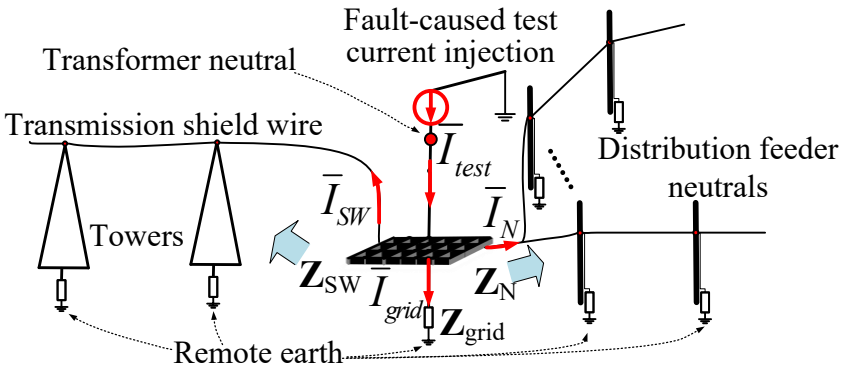

Figure 2.4 Fault-caused test current splits within the substation grounding system

2.3 Interference Issues

Although the proposed method is simple in concept, its successful application requires solving several challenging interference issues. The main issues are identified and analyzed in this section.

2.3.1 Interference Due to Fault Current Injection Caused Substation Soil Potential Change

When a fault current flows into the substation grounding grid, the soil potential will change. This implies that the soil near the substation will also experience a non-zero potential. As a result, the neutral M rods nearing the substation are not at zero potential. This can be understood using the extra voltage sources ($\bar{V}_{S1}$, ⋯, $\bar{V}_{Sn}$) added to each rod of neutral M, as shown in Figure 2.5. These extra voltages fade with the increased distance from the substation. With this interference, the voltage at point X is no longer zero, and the GPR obtained by the voltage monitor is not exactly equal to the true GPR.

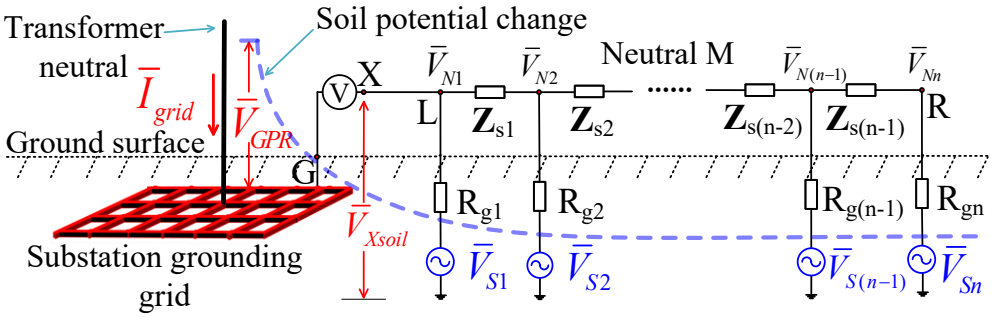

Figure 2.5 Impact of the soil potential interference on GPR measurement

The circuit theory shows that if neutral M is long enough, the soil potential change has a negligible impact on the voltage at point X (i.e., the reference of GPR measurement). Now, the question becomes how long it is necessary for neutral M to measure the GPR with acceptable accuracy. To obtain the answer, an index $\bar{\varepsilon}_{soil}$ is introduced to quantify the GPR measurement error due to the soil potential interference.

$$\bar{\varepsilon}_{soil} = \bar{V}_{Xsoil} / \bar{V}_{GPR} \tag{2.5}$$

where $\bar{V}_{Xsoil}$ is the voltage at point X due to the soil potential interference. $\bar{V}_{GPR}$ is the true GPR of the substation grounding grid.

The equation to calculate $\bar{\varepsilon}_{soil}$ is derived by nodal analysis using the neutral M circuit shown in Figure 2.5. In this circuit, node X is considered open since there is a very large impedance of the voltage monitor. The nodal voltages from node L to node R are denoted as $\bar{V}_{Nk}$ $(k = 1, 2, \cdots, n)$. The nodal voltage equation for the neutral M circuit can be written as

$$\left[\bar{V}_{Nk}\right]_{n\times 1} = \mathbf{Y}_M^{-1}\left[\bar{V}_{Sk}/R_{gk}\right]_{n\times 1} \tag{2.6}$$

where n is the number of rods of neutral M, and R_{gk} is the grounding resistance of the k^{th} rod. $\boldsymbol{Y}_M$ is the admittance matrix of the neutral M circuit in the dimension of $n \times n$. It can be written as follows:

$$\begin{bmatrix}
\frac{1}{R_{g1}}+\frac{1}{Z_{s1}} & -\frac{1}{Z_{s1}} & 0 & 0 & 0 \\
-\frac{1}{Z_{s1}} & \frac{1}{R_{g2}}+\sum_{i=1}^{2}\frac{1}{Z_{si}} & -\frac{1}{Z_{s2}} & 0 & 0 \\
0 & \ddots & \ddots & \ddots & 0 \\
0 & 0 & -\frac{1}{Z_{s(n-2)}} & \frac{1}{R_{g(n-1)}}+\sum_{i=n-2}^{n-1}\frac{1}{Z_{si}} & -\frac{1}{Z_{s(n-1)}} \\
0 & 0 & 0 & -\frac{1}{Z_{s(n-1)}} & \frac{1}{R_{gn}}+\frac{1}{Z_{s(n-1)}}
\end{bmatrix}$$

where Z_{sk} is the series impedance of the k^{th} span conductor of neutral M.

The voltage $\bar{V}_{Xsoil}$ at point X is equal to the voltage $\bar{V}_{N1}$ at node L, and it can be calculated as follows:

$$\bar{V}_{Xsoil} = \bar{V}_{N1} = \mathbf{T}\mathbf{Y}_M^{-1}\left[\bar{V}_{Sk}/R_{gk}\right]_{n\times 1} \tag{2.7}$$

where vector $\mathbf{T}=[1 \quad 0 \quad \cdots \quad 0]$ in the dimension of $1 \times n$.

Since the k^{th} rod of neutral M is at some distance from the substation grounding grid, the transfer voltage at the k^{th} rod can be roughly estimated by (2.8) [22].

$$\bar{V}_{Sk} = \rho\bar{I}_{grid}/(2\pi d_k) \tag{2.8}$$

where d_k is the distance between the k^{th} rod of neutral M and the center of the grounding grid. $\bar{I}_{grid}$ is the fault current flowing into the grounding grid. If there are some shield wires or feeder neutrals connected to the substation grounding grid, $\bar{I}_{grid}$ is only a part of the fault current.

Substituting (2.8) into (2.7), one can have

$$\bar{V}_{Xsoil} = \mathbf{T}\mathbf{Y}_M^{-1}\mathbf{G}\rho\bar{I}_{grid}/2\pi \tag{2.9}$$

where vector $\mathbf{G} = [1/(d_1R_{g1}) \quad \cdots \quad 1/(d_nR_{gn})]^T$ in the dimension of $n \times 1$.

Upon substitution of (2.9) and $\bar{V}_{GPR} = Z_{grid}\bar{I}_{grid}$ into (2.5), the error is obtained as

$$\bar{\varepsilon}_{soil} = \mathbf{T}\mathbf{Y}_M^{-1}\mathbf{G}\Big/\left(2\pi S_{grid}\right) = f_1(S_{grid}, R_{gk}, Z_{sk}, d_k, n) \tag{2.10}$$

where $S_{grid} = Z_{grid}/\rho$. Since the grounding impedance is always in proportion to soil resistivity ρ [22], S_{grid} is actually an indicator of the conditions of the metallic grounding grid.

It is revealed in (2.10) that the error $\bar{\varepsilon}_{soil}$ is dependent on the parameters of neutral M and S_{grid}. The deterioration of the metallic grounding grid, i.e., the increase of S_{grid}, will reduce the error, which is good for grounding grid condition monitoring. The neutral M circuit in Figure 2.5 also indicates that the soil potential change cancels a part of the true GPR, which tends to reduce the estimated substation grounding impedance results.

It is worthwhile noting that some neutrals and shield wires (including the neutral in the faulted feeder if there is one) may exist connecting to the substation grounding grid. Unlike the substation grounding grid, neutral/shield wire rods have a small zone of influence due to their slender structures, as shown in Appendix A. Therefore, all the neutral/shield wire rods can be considered to have little impact on the soil potential at the substation grounding grid and the neutral M rods.

2.3.2 Interference Due to Fault-Caused Voltage Sag

When a fault occurs, the faulted phase experiences a voltage sag. This voltage sag may result in a noticeable load current change in this phase, causing an unbalanced three-phase load. The unbalanced load current in the feeder M will induce an electromotive force (EMF) in each span of neutral M, interfering in the GPR measurement. This phenomenon is described in Figure 2.6, where these EMFs are denoted as $\bar{V}_{ind1}$, …, $\bar{V}_{ind(n-1)}$, and $\bar{V}_{indn}$.

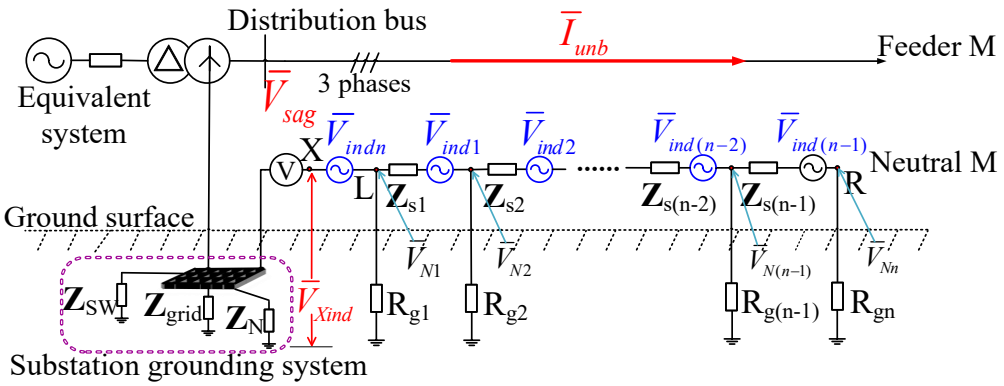

Figure 2.6 Impact of the voltage-sag-caused inductive interference on GPR measurement.

To quantify the GPR measurement error caused by these induced voltages, the index $\bar{\varepsilon}_{ind}$ is introduced in (2.11).

$$\bar{\varepsilon}_{ind} = \bar{V}_{Xind} / \bar{V}_{GPR} \tag{2.11}$$

where $\bar{V}_{Xind}$ is the voltage at point X due to the fault-caused voltage sag.

In neutral M, the voltage-sag-caused induced EMF $\bar{V}_{indk}$ on the k^{th} span can be expressed by

$$\bar{V}_{indk} = Z_{amk}\bar{I}_{\Delta Ma} + Z_{bmk}\bar{I}_{\Delta Mb} + Z_{cmk}\bar{I}_{\Delta Mc} \tag{2.12}$$

where $\bar{I}_{\Delta Ma}$, $\bar{I}_{\Delta Mb}$, and $\bar{I}_{\Delta Mc}$ are the changes of three-phase load currents in feeder M due to the fault-caused voltage sag on the distribution bus. Z_{amk}, Z_{bmk}, and Z_{cmk} are mutual impedances between the three-phase and neutral M conductors in the k^{th} span, respectively.

One can assume that $Z_{amk} = Z_{bmk} = Z_{cmk} = Z_{mk}$ since the distances between the neutral and three-phase conductors are almost equal. Thus, (2.12) can be rewritten as

$$\bar{V}_{indk} = Z_{mk}(\bar{I}_{\Delta Ma} + \bar{I}_{\Delta Mb} + \bar{I}_{\Delta Mc}) = 3Z_{mk}\bar{I}_{\Delta M0} \tag{2.13}$$

where $\bar{I}_{\Delta M0}$ is the change of zero sequence load current in feeder M during and before the fault.

$\bar{I}_{\Delta M0}$ can be determined by the zero sequence circuits shown in Figure 2.7. In the figure, Z_{T0} is the zero sequence impedance of the substation transformer, Z_{M0} and $Z_{eq.others0}$ are the

equivalent zero sequence impedances of feeder M and all other feeders, including loads, seeing from the distribution bus. Z_{sys} is the substation grounding system impedance, including shield wires and feeder neutrals.

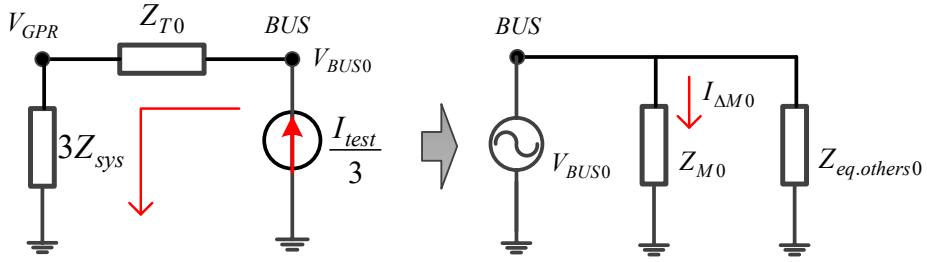

Figure 2.7 Zero sequence circuit for determination of the unbalanced current

Since the zero sequence impedance of the system side is much less than that of the load side, it is reasonable to assume that the whole fault current flows into the system side. The zero sequence voltage at the distribution bus can be approximated by

$$\bar{V}_{BUS0} = (3Z_{sys} + Z_{T0})\frac{\bar{I}_{test}}{3} \tag{2.14}$$

Since $\bar{I}_{test} = \bar{V}_{GPR}/Z_{sys}$, one can have

$$\bar{I}_{\Delta M0} = \frac{\bar{V}_{BUS0}}{Z_{M0}} = \frac{3Z_{sys} + Z_{T0}}{3Z_{sys}Z_{M0}}\bar{V}_{GPR} \tag{2.15}$$

Substituting (2.15) into (2.13), the voltage-sag-caused induced EMF $\bar{V}_{indk}$ on the k^{th} span is given by:

$$\bar{V}_{indk} = \frac{3Z_{sys} + Z_{T0}}{Z_{sys}Z_{M0}} Z_{mk}\bar{V}_{GPR} \tag{2.16}$$

Following the same nodal analysis approach in section 2.3.1, the nodal voltage on the neutral M conductor, $\bar{V}_{Nk}$, can be determined by

$$\left[\bar{V}_{Nk}\right]_{n\times 1} = \mathbf{Y}_M^{-1}\begin{bmatrix} \bar{V}_{ind1}/Z_{s1} \\ \bar{V}_{ind2}/Z_{s2} - \bar{V}_{ind1}/Z_{s1} \\ \vdots \\ \bar{V}_{ind(n-1)}/Z_{s(n-1)} - \bar{V}_{ind(n-2)}/Z_{s(n-2)} \\ -\bar{V}_{ind(n-1)}/Z_{s(n-1)} \end{bmatrix}_{n\times 1} \tag{2.17}$$

Substituting (2.16) into (2.17), the voltage at the node L is given by:

$$\bar{V}_{N1} = \mathbf{T}\mathbf{Y}_M^{-1}\mathbf{H}\frac{3Z_{sys}+Z_{T0}}{Z_{sys}Z_{M0}}\bar{V}_{GPR} \tag{2.18}$$

where vector $\mathbf{H}$ is in the dimension of $n\times 1$ as

$$\left[Z_{m1}/Z_{s1} \quad \left[Z_{m(i+1)}/Z_{s(i+1)} - Z_{mi}/Z_{si}\right]_{1\times(n-2)} \quad -Z_{m(n-1)}/Z_{s(n-1)}\right]^T,\ i=1,2,\cdots n-2.$$

Thus, the voltage at point X due to the voltage-sag-caused inductive interference can be expressed as

$$\bar{V}_{Xind} = \bar{V}_{N1} + \bar{V}_{indn} = (\mathbf{T}\mathbf{Y}_M^{-1}\mathbf{H} + Z_{mn})\frac{3Z_{sys}+Z_{T0}}{Z_{sys}Z_{M0}}\bar{V}_{GPR} \tag{2.19}$$

where Z_{mn} is the mutual impedance between the connection wire X-L and phase conductors, and $\bar{V}_{indn}$ is the induced EMF on the connection wire X-L.

Finally, the error $\bar{\varepsilon}_{ind}$ can be expressed as

$$\bar{\varepsilon}_{ind} = (\mathbf{T}\mathbf{Y}_M^{-1}\mathbf{H} + Z_{mn})\frac{3Z_{sys}+Z_{T0}}{Z_{sys}Z_{M0}} = f_2(Z_{sys}, Z_{T0}, Z_{M0}, R_{gk}, Z_{mk}, Z_{sk}, Z_{mn}, n) \tag{2.20}$$

It can be seen in (2.20) that the error $\bar{\varepsilon}_{ind}$ is determined by the parameters of neutral M and the substation transformer, the load level of feeder M, and the grounding system impedance. Since the lower the load level, the higher the zero sequence impedance Z_{M0}, it is preferred that the feeder with lower loads is considered as feeder M. Equation (2.20) also shows that the increase of

grounding system impedance Z_{sys}, which is caused by the grounding grid deterioration, reduces the error. There is no out-of-control error increase with deteriorated grounding grid conditions.

2.3.3 Interferences Due to Fault Location

The fault location may impose interferences on GPR measurement in three ways, as illustrated in Figure 2.8. First, the fault changes the soil potential near the fault location and thus changes the substation GPR if the fault is too close to the substation. Second, the transfer voltages in the soil coupled on the neutral M rods ($\bar{V}_{S1}^{F}$, ⋯, $\bar{V}_{Sn}^{F}$) may interfere in the GPR measurement if the fault occurs too close to neutral M. Third, the fault current in the faulted feeder may induce an EMF on each span of neutral M as $\bar{V}_{ind1}^{F}$, ⋯, $\bar{V}_{ind(n-1)}^{F}$, and $\bar{V}_{indn}^{F}$, if the neutral M is close enough to the faulted feeder. These induced voltages will result in a non-zero voltage at terminal X and cause errors on the measured GPRs.

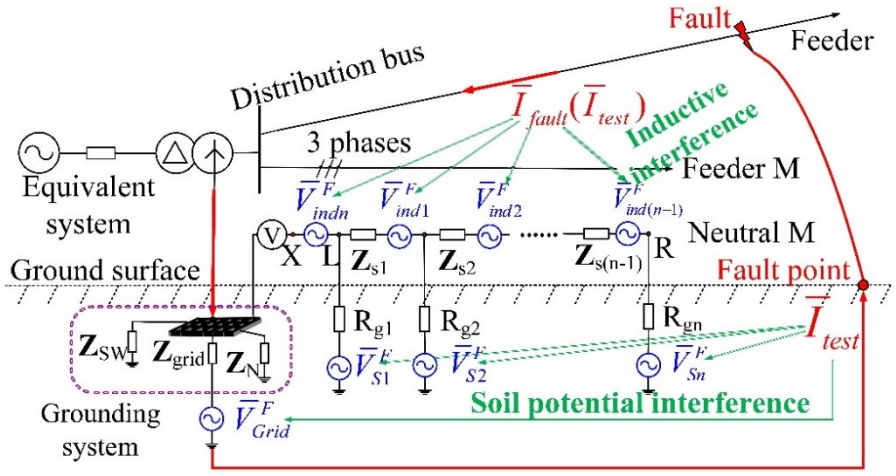

Figure 2.8 Impacts of fault current's interferences on GPR measurement

2.3.3.1 Soil Potential Change at Substation

The impact of soil potential change, when a fault is close to the substation, can be understood by Figure 2.9, where $Z_{g.fault}$ indicates the grounding impedance at the fault location. The measured GPR of the substation grounding grid is reduced by the soil potential dip due to the soil potential change at the fault location. As the fault point should be at some distance from the substation, this change can be approximately estimated by [22]

$$\bar{V}_{Grid}^{F} = \rho \bar{I}_{test} \Big/ \left(2\pi d_f\right) \tag{2.21}$$

where $\bar{V}_{Grid}^{F}$ is the transfer voltage from the fault point to the substation grounding grid, and d_f is the distance between the fault point and the substation.

Since $\bar{I}_{test} = \bar{V}_{GPR}/Z_{sys}$, the error caused by the transfer voltage is introduced as

$$\bar{\varepsilon}_{Fgrid} = \bar{V}_{Grid}^{F} \Big/ \bar{V}_{GPR} = 1/(2\pi d_f S_{sys}) = f_3(S_{sys}, d_f) \tag{2.22}$$

where S_{sys} is defined as Z_{sys}/ρ.

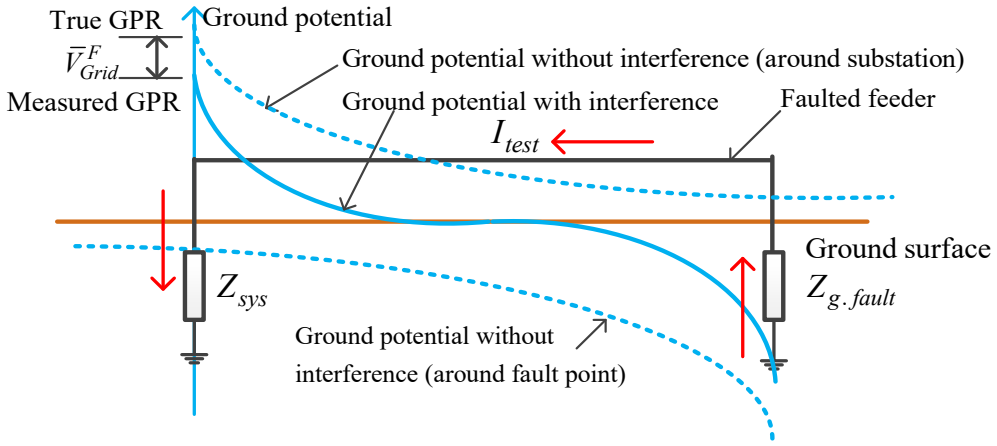

Figure 2.9 Illustration of the impact caused by the fault close to the substation

It is revealed in (2.22) that the error $\bar{\varepsilon}_{Fgrid}$ is determined by the distance between the substation and the fault location, and S_{sys}. Again, the deterioration of the grounding grid always reduces the error. This error can be significantly reduced if the fault is at some distance from the substation.

2.3.3.2 Soil Potential Change at Rods of Neutral M

Similarly, the rods of neutral M may experience soil potential change if the fault point is close to neutral M, as described by $\bar{V}_{S1}^{F}$, ⋯, $\bar{V}_{Sn}^{F}$, in Figure 2.8. This decreases the potential of the neutral M rods, resulting in a negative potential at point X and an increase of the GPR read. To quantify this error, the index $\bar{\varepsilon}_{Fsoil}$ is introduced as follows:

$$\bar{\varepsilon}_{Fsoil} = \bar{V}^{F}_{Xsoil} \big/ \bar{V}_{GPR} \tag{2.23}$$

where $\bar{V}^{F}_{Xsoil}$ is the voltage at point X under fault-current-caused soil potential change at each rod of neutral M.

$\bar{\varepsilon}_{Fsoil}$ is derived following the same nodal analysis approach in section 2.3.1. The nodal voltage $\bar{V}_{Nk}$ is determined by

$$\left[\bar{V}_{Nk}\right]_{n\times 1} = \mathbf{Y}_{M}^{-1}\left[\bar{V}^{F}_{Sk} \big/ R_{gk}\right]_{n\times 1} \tag{2.24}$$

where $\bar{V}^{F}_{Sk}$ is the soil potential change at the k^{th} rod of neutral M due to the transfer voltages from the fault point. It can be roughly estimated using (2.25), as the fault point should be at some distance from each rod of neutral M.

$$\bar{V}^{F}_{Sk} = \rho \bar{I}_{test} \big/ \left(2\pi d_{fk}\right) \tag{2.25}$$

where d_{fk} is the distance between the fault point and the k^{th} rod of neutral M.

Substituting (2.25) into (2.24), one can have

$$\bar{V}^{F}_{Xsoil} = \bar{V}_{N1} = \mathbf{T}\mathbf{Y}_{M}^{-1}\mathbf{P}\rho \bar{I}_{test} \big/ 2\pi \tag{2.26}$$

where vector $\mathbf{P} = [1/(d_{f1}R_{g1}) \quad \cdots \quad 1/(d_{fn}R_{gn})]^{T}$ in the dimension of $n \times 1$.

Substituting (2.26) and $\bar{V}_{GPR} = \bar{I}_{test}Z_{sys}$ into (2.23), the error is expressed as

$$\bar{\varepsilon}_{Fsoil} = \mathbf{T}\mathbf{Y}_{M}^{-1}\mathbf{P} \big/ \left(2\pi S_{sys}\right) = f_4(S_{sys}, d_{fk}, R_{gk}, Z_{sk}, n) \tag{2.27}$$

It can be seen from (2.27) that the error $\bar{\varepsilon}_{Fsoil}$ is determined by the parameters of neutral M, the distance between the fault point and neutral M rods, and S_{sys}. Again, the deterioration of the grounding grid always reduces the error. The error can be significantly reduced when keeping the neutral M an adequate distance from the faulted feeder by properly selecting faulted feeders.

2.3.3.3 Fault Current Caused Induction on Neutral M

If the faulted feeder is close enough, the fault current may induce significant EMFs on neutral M. The mechanism of this interference is the same as the one presented in section 2.3.2. To quantify the error, the index $\bar{\varepsilon}_{Find}$ is introduced in (2.28), where $\bar{V}_{Xind}^{F}$ is the voltage at point X due to the fault current induction.

$$\bar{\varepsilon}_{Find} = \bar{V}_{Xind}^{F} / \bar{V}_{GPR} \tag{2.28}$$

$\bar{\varepsilon}_{Find}$ can be studied using the same nodal analysis approach in section 2.3.2. The final equation can be obtained as

$$\bar{\varepsilon}_{Find} = (\mathbf{T}\mathbf{Y}_{M}^{-1}\mathbf{Q} + Z_{mn}^{F}) / Z_{sys} = f_5(Z_{sys}, Z_{mk}^{F}, R_{gk}, Z_{sk}, n) \tag{2.29}$$

where Z_{mn}^{F} is the mutual impedance between the connection wire X-L and the faulted feeder. $\mathbf{Q}$ is a $n \times 1$ vector, $\left[Z_{m1}^{F}/Z_{s1} \quad \left[Z_{m(i+1)}^{F}/Z_{s(i+1)} - Z_{mi}^{F}/Z_{si}\right]_{1\times(n-2)} \quad -Z_{m(n-1)}^{F}/Z_{s(n-1)}\right]^{T}$.

The error $\bar{\varepsilon}_{Find}$ is determined by the parameters of neutral M, the distance between the faulted feeder and neutral M, and Z_{sys}. Once again, the deterioration of the grounding grid always reduces the error. The proper selection of the faulted feeder to give neutral M enough space from the faulted feeder can significantly reduce this error.

It is worthwhile noting that the impedances Z_N and Z_{SW} are represented in a concentrated way in Figure 2.8; however, the location of these neutral/shield wire rods is diffuse. Due to the transfer voltages from the fault point to these grounding rods, the estimated errors $\bar{\varepsilon}_{Fgrid}$ and $\bar{\varepsilon}_{Fsoil}$ may have a slight difference, especially when observing the grounding system impedance $Z_{sys\_measure}$ using (2.3). In addition, the fault current flowing through the neutrals of adjacent feeders can induce EMFs in the neutral M and thus changes the error $\bar{\varepsilon}_{Find}$. However, this is a minor impact because sufficient distances between the selected neutral M and the other feeders have been a requirement proposed by the methodology.

2.4 Discussion on the Interference-Caused Errors

The interferences essentially originate from the fault current. This fault-caused disturbance affects the GPR measurement in different and independent ways. Each interference-caused error is added at either terminal X or terminal G, as shown in Figure 2.10. The true value of GPR, $\bar{V}_{GPR}$, can therefore be obtained by (2.30).

$$\bar{V}_{GPR} - \bar{V}^{F}_{Grid} = \bar{V}_{GPR\_measure} + \bar{V}_{Xsoil} + \bar{V}_{Xind} - \bar{V}^{F}_{Xsoil} - \bar{V}^{F}_{Xind} \tag{2.30}$$

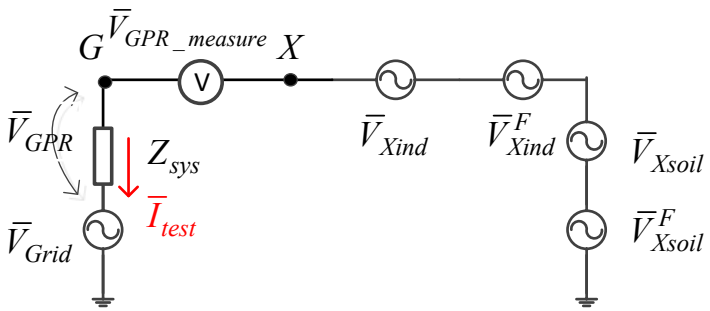

Figure 2.10 GPR measurement with various interferences

The total substation grounding impedance estimation error $\bar{\varepsilon}$ can therefore be expressed as

$$\bar{\varepsilon} = \bar{\varepsilon}_{soil} + \bar{\varepsilon}_{ind} + \bar{\varepsilon}_{Fgrid} - \bar{\varepsilon}_{Find} - \bar{\varepsilon}_{Fsoil} \tag{2.31}$$

2.4.1 Characteristics of Interference-Caused Errors

According to the analysis and expressions of the five errors, one can find that all these errors are independent of the fault current. This suggests that the magnitude of the fault current does not affect the measurement accuracy. During the fault, these errors exist simultaneously, but they do not impact each other.

The deterioration of the substation grounding grid always reduces the errors, which is good for guaranteeing the accuracy of measurements since the concern arises when the grounding grid condition worsens.

The parameters of neural M are involved in all the errors. This means that the neutral M must be carefully selected to reduce the interferences.

The analysis has shown that the interference caused by the substation soil potential change due to the nearby fault and the interference caused by the neutral M rod potential change due to the substation potential rise during the fault reduce the GPR read, while the interference caused by the neutral M rod potential change due to the nearby fault increases the GPR read. The phasor diagrams in Figure 2.11 give us a rough idea of how the two inductive interferences affect the substation grounding impedance measurements. Figure 2.11(a) shows the phasor diagram for the voltage-sag-caused inductive interference. If the fault occurs at phase A, the voltage sag appears at phase A. The unbalanced current $\bar{I}_{unb}$ has the opposite direction of $\bar{V}_A$ when the load is of high power factor. The induced EMF on the neutral M $\bar{V}_{ind}$ lags $\bar{I}_{unb}$ almost 90°. Figure 2.11(b) shows the phasor diagram for the fault-current-caused inductive interference. In this case, the fault current lags $\bar{V}_A$ 90°. The induced EMF $\bar{V}_{ind}^{F}$ is therefore in the opposite direction of $\bar{V}_A$. In both cases, the induced EMF tends to increase the GPR read, leading to a higher grounding impedance measurement. The above observations suggest that all the errors do not simply add up to make things worse, making our expectations optimistic when dealing with interference issues.

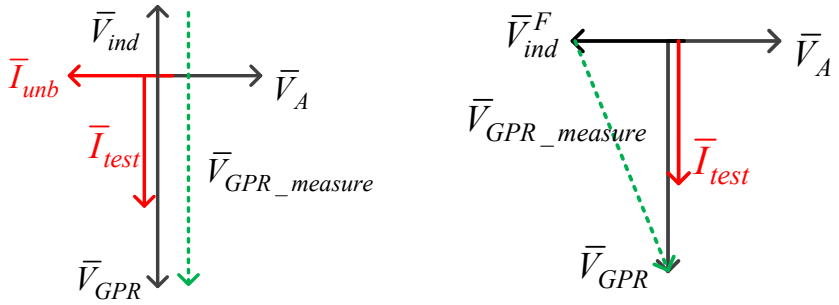

(a) Impact of error $\bar{\varepsilon}_{ind}$ (b) Impact of error $\bar{\varepsilon}_{Find}$

Figure 2.11 Phasor diagrams to explain the impact of inductive interferences

2.4.2 Ideas to Reduce or Limit Errors

Each error should be limited to an acceptable range for the proposed method to work. Based on the analysis conducted in the previous sections, possible solutions to reduce errors can be identified and are explained here:

- For the interference caused by substation soil potential change due to fault current injection, the neutral M should be long enough to limit the error. The minimal length of neutral M needs to be determined.

- For the interference caused by voltage sag, the load impedance plays an important role. A lower load level results in a smaller error. Therefore, a feeder with lighter loads is preferred when selecting feeder M.

- For the interference caused by substation soil potential change due to a nearby fault, the closest distance of the fault point to the substation, resulting in acceptable errors, should be identified.

- For the interference caused by the potential change of the neutral M rod due to a nearby fault, the minimal distance between the fault point and the neutral M should be determined.

- For the interference caused by induction from the faulted feeder, the fault occurring at the feeder that is too close to feeder M should not be used.

In summary, it is possible to achieve reasonable accuracy by selecting a proper feeder as feeder M and by using only a selected set of faults for grounding impedance estimation. These ideas need to be investigated using realistic data from actual cases. The investigation is presented in the following sections.

2.5 Verification Studies

To verify the proposed method, simulation studies were performed using a realistic case based on industry data.

2.5.1 Description of the Study Case

The overall system of this study case is shown in Figure 2.12. A 138/25kV transformer in Δ-Y_g connection is powered by a transmission line with an equivalent power supply. There are four feeders, at the end of which all the loads are in Y_g connection with a 0.95 lagging power factor. The parameters of the transmission line and the feeders are presented in Figure 2.13 and Table 2.1.

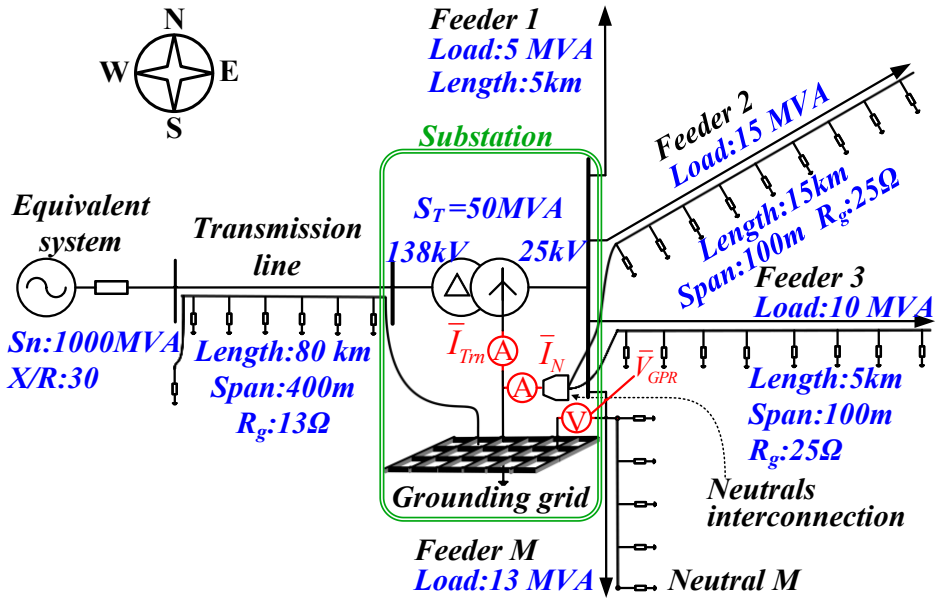

Figure 2.12 The layout of the study case

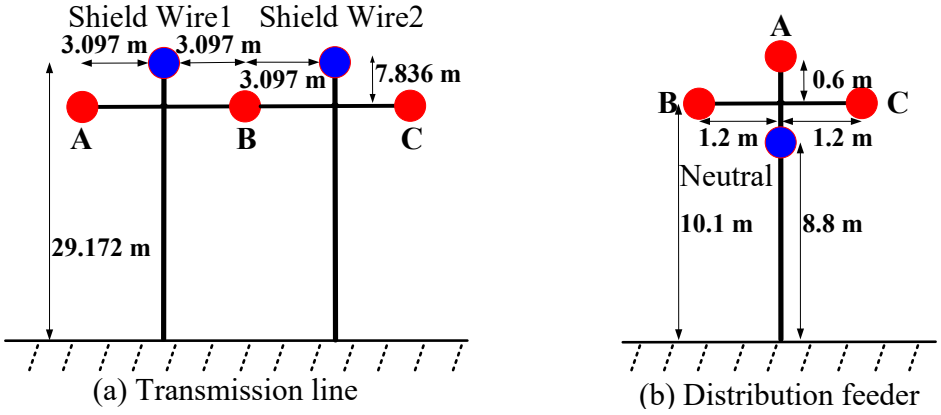

Figure 2.13 Physical structures of power lines

The details of the neutral of the 4th feeder (selected as neutral M for the GPR measurement) and the substation grounding grid are shown in Figure 2.14 and Figure 2.15, respectively. Feeders 1~3 are at an angle of 180°, 135°, and 90° clockwise to neutral M, respectively. The soil resistivity is assumed as 100Ωm. To exclude the impact of feeder neutrals that are connected to the substation grounding grid, a current monitor is installed at the neutral bonding conductor, as shown in Figure 2.12.

Table 2.1 Conductors of transmission line/distribution feeders

	Three-phase conductor	Ground conductor
Outer radius (m)	0.0203454 / 0.006375	0.0055245 / 0.0039
DC resistance (Ω/km)	0.03206 / 0.3375	2.8645 / 0.8530
Type	Chukar / 3/0 Pigeon	½ High Strength Steel / #2 Haddock

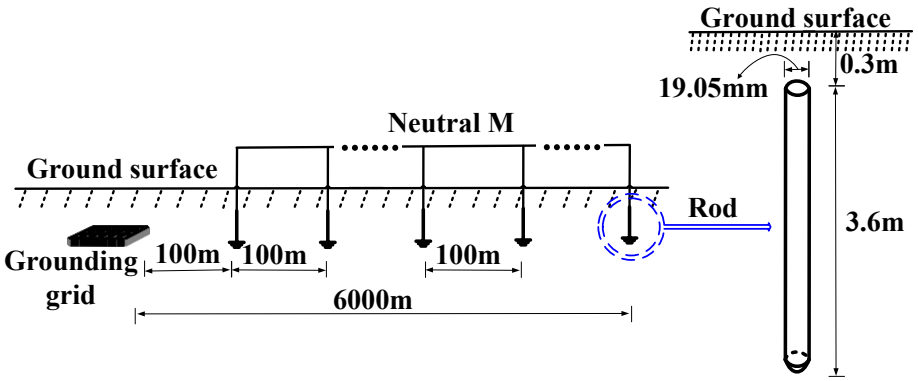

Figure 2.14 Layout and parameters of neutral M

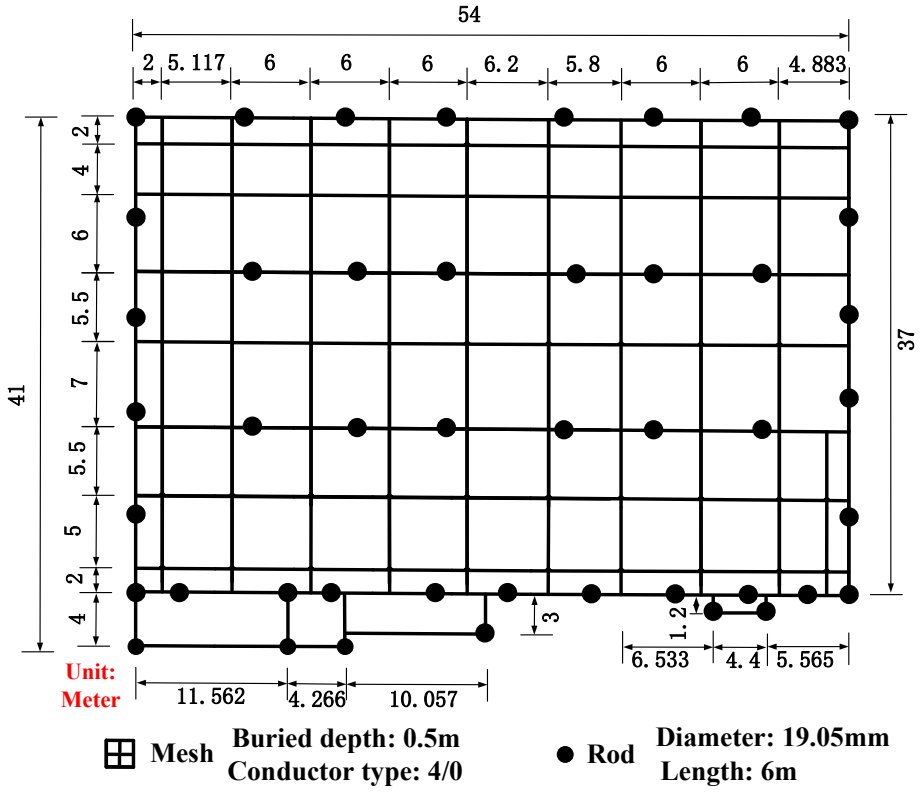

Figure 2.15 Layout and parameters of the substation grounding grid

2.5.2 Simulation Platform and Parameter Determination

This study involves grounding studies and fault studies at the power system level in the time domain. No single software can directly conduct such simulations to verify the proposed method. Thus, a combined simulation is used. This simulation can reflect all the interferences that exist in the measurement of the substation grounding impedance. The key idea is that the CDEGS software is firstly used to calculate the substation grounding grid impedance and the transfer voltages on all the neutral/shield wire rods from the grounding grid by using the complete substation grounding grid, all the neutral/shield wire rods, soil resistivity information, and a 1A test current injection. It should be noted that the calculated transfer voltage on each neutral/shield wire rod can be used as the mutual impedance coefficient of the current controlled voltage source module, which functions as the transfer voltage from the grounding grid, in the following simulation in Simulink. In this way, a time-varying transfer voltage controlled by a time-varying grounding grid current $i_{grid}(t)$ is built at each neutral/shield wire rod. The fault current, GPR and transfer voltages can be simultaneously triggered by a fault in one simulation in Simulink. The simulation process is presented in the following.

Step 1: A test system consisting of modules of power equipment and interferences is structured in Simulink. The transfer voltage from the substation grounding grid on each neutral/shield wire rod in the soil is modelled as a current controlled voltage source module with a mutual impedance coefficient.

Step 2: Parameters of power equipment and interferences are prepared using the numerical calculation embedded in the MATLAB codes and assigned to the corresponding modules in Simulink, except for the grounding grid impedance and its transfer voltages on each neutral/shield wire rod.

Step 3: The grounding grid impedance is simulated in CDEGS by building the complete substation grounding grid and setting the soil resistivity information. This impedance is fed into the corresponding impedance module in Simulink.

Step 4: As the grounding grid, all the neutral/shield wire rods and the soil resistivity are set up in CDEGS, a transfer voltage on each neutral/shield wire rod is obtained by injecting a 1A current at the center of the substation grounding grid. The transfer voltages are respectively fed into the current controlled voltage sources as mutual impedance coefficients at the corresponding neutral/shield wire rods in Simulink.

Step 5: As all the test system parameters are prepared in Simulink, a time-domain simulation is conducted (with a single-phase-to-ground fault). The outputs of interest are obtained to run the proposed algorithm.

It is shown in Appendix A that the transfer voltage from the neutral/shield wire rod decays quickly to a negligibly low value in a short distance (e.g., the transfer voltage from a regular rod is reduced to 1% of its GPR in about 50m). In consideration of their separated distance in practice and for the sake of simplification in the simulations, there is no need to consider the neutral/shield wire rods' mutual impact and their influence on the substation grounding grid unless two grounding electrodes are too close.

In this study, the self- and mutual impedances of the transmission and distribution lines are determined using the equations in [71]. Mutual impedances between conductors of each neutral M span and other feeders are determined using the method introduced in [72]. The substation grounding grid impedance Z_{grid} is determined as 0.8734Ω almost in resistive in CDEGS simulations. The grounding resistance of neutral M rods is determined as 27.9Ω using (2.32) [22].

$$R_g = \frac{\rho}{2\pi L_{rod}} (\ln \frac{4L_{rod}}{r_{rod}} - 1) \tag{2.32}$$

where ρ is soil resistivity, L_{rod} and r_{rod} are the length and the radius of the grounding rod as shown in Figure 2.14.

2.5.3 Simulation Results of Substation Grounding Impedance

Assume that a phase C to ground fault occurs on Feeder 1, 3km from the substation. The current waveforms on Feeder 1 are shown in Figure 2.16. The voltage waveforms on the distribution bus

are presented in Figure 2.17. During the fault, the ground potential profile around the substation is shown in Figure 2.18. The fault occurs at 0.2s and is cleared at 0.4s.

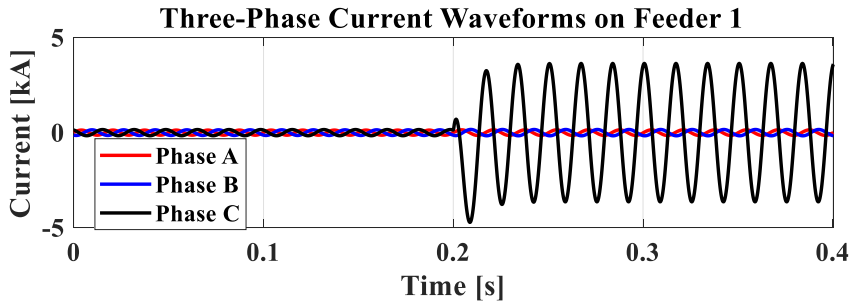

Figure 2.16 Three-phase current waveforms on feeder 1

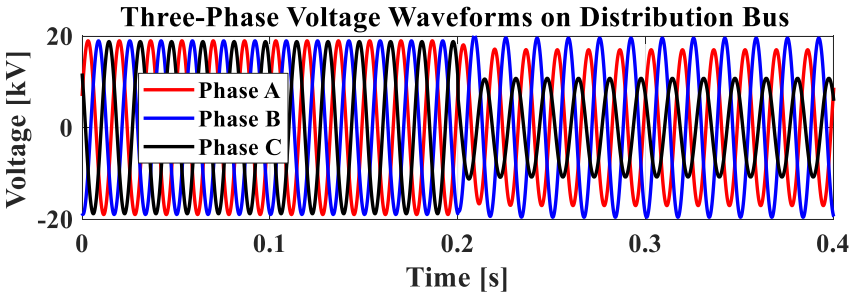

Figure 2.17 Three-phase voltage waveforms on distribution bus

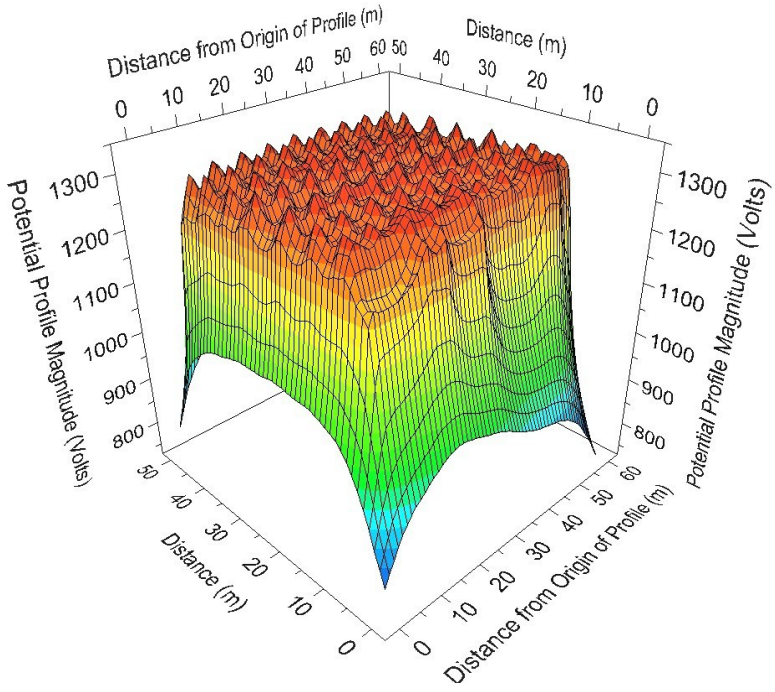

Figure 2.18 Ground potential profile around the substation during the fault

The waveforms of transformer neutral current, feeder neutral current and substation grounding grid voltage are "recorded" by the current and voltage monitors (seen in Figure 2.12). They are presented in Figure 2.19 and Figure 2.20, respectively. The phase A voltage at the distribution bus is taken as the reference. Before the fault, the currents and voltage at 60Hz are 48+j72A, 24+j40A, and 13+j22V, respectively. They are mainly caused by unbalanced loads. When the fault enters steady-state, the 60Hz currents and voltage are 3166-j982A, 1194-j703A, and 1231-j254V, respectively.

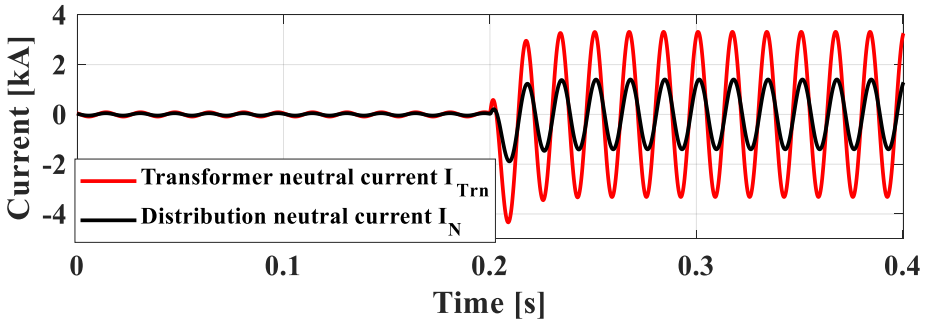

Figure 2.19 The waveforms of transformer and feeder neutral currents

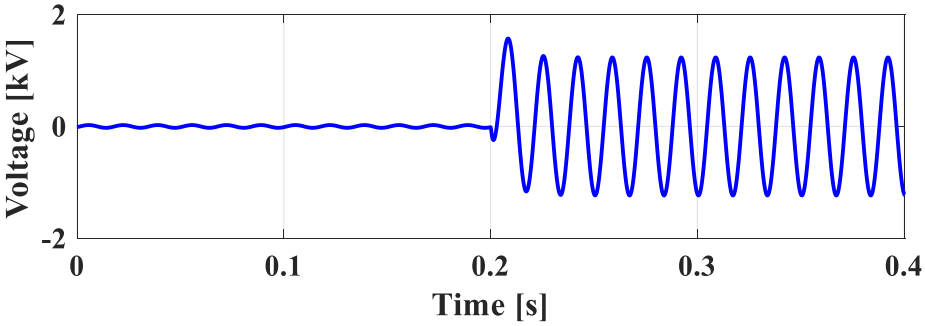

Figure 2.20 The waveform of the substation grounding grid voltage

The substation grounding impedances, including and excluding the contribution of feeder neutrals, $Z_{sys\_measure}$ and $Z_{grid\_measure}$ are 0.3773+j0.0391Ω and 0.6317-j0.0407Ω, respectively. They are close to the true values of 0.3961+j0.0865Ω and 0.6903+j0.0337Ω, respectively.

The absolute percentages of five GPR measurement errors, $\bar{\varepsilon}_{soil}$, $\bar{\varepsilon}_{ind}$, $\bar{\varepsilon}_{Fgrid}$, $\bar{\varepsilon}_{Fsoil}$, and $\bar{\varepsilon}_{Find}$, are 3.1%, 5.2%, 1.3%, 1.0% and 6.3%, respectively. Those errors have different phase angles, and their phasor summation results in an estimated total error of 13.9%. This estimated total error is very close to the simulation error of 13.7% when observing $Z_{grid\_measure}$. The simulation results

also suggest that the impact of the feeder neutrals is not negligible if many neutrals are connected to the substation grounding grid. If users intend to include the contributions of the feeder neutrals to the overall performance of substation grounding, there is no need to measure the current of feeder neutrals.

More simulation results of eleven phase C to ground faults at different locations are presented in Table 2.2.

Table 2.2 Simulation results of more fault events

Fault event	Faulted feeder	Distance to substation	$Z_{grid\_measure}$ (Ω)	Simulation error (%)
$\mathbf{F_1}$	Feeder 1	1km	0.6304-j0.0371	13.42%
$\mathbf{F_2}$	Feeder 1	2km	0.6316-j0.0396	13.59%
$\mathbf{F_3}$	Feeder 1	4km	0.6317-j0.0415	13.79%
$\mathbf{F_4}$	Feeder 1	5km	0.6318-j0.0423	13.88%
$\mathbf{F_5}$	Feeder 2	1km	0.6434-j0.0333	11.83%
$\mathbf{F_6}$	Feeder 2	5km	0.6540-j0.0463	12.71%
$\mathbf{F_7}$	Feeder 2	8km	0.6550-j0.0526	13.49%
$\mathbf{F_8}$	Feeder 2	15km	0.6610-j0.0670	15.17%
$\mathbf{F_9}$	Feeder 3	1km	0.6652-j0.0045	6.61%
$\mathbf{F_{10}}$	Feeder 3	3km	0.6748-j0.0064	6.22%
$\mathbf{F_{11}}$	Feeder 3	5km	0.6726-j0.0074	6.29%

One can see from Table 2.2 that the simulated substation grounding impedances vary with fault locations due to the contributions of various interferences. Specifically, the errors are similar for faults in the same feeder. Their differences are slightly larger for faults in different feeders, mainly due to the impacts of inductive interference from the fault current. Similar to the base case, the simulation errors in Table 2.2 are close to the corresponding estimated errors from the direct calculation. Take the F_5 case as an example: the estimated error is 12.74%, while the simulation error is 11.83%. The slight difference (i.e., 6mΩ for 0.9%) may be due to the neglect of the transfer

voltages on shield wire rods from the substation grounding grid and the neglect of the inductive interferences in neutral M from shield wires and neutrals in the estimated calculation. More importantly, the total errors for these cases are always acceptable. This confirms that the proposed method has adequate accuracy in measuring the substation grounding impedance.

2.6 Sensitivity Studies

Three types of interferences are expected by the proposed method. Each interference may result in a GPR measurement error. This section presents the sensitivity studies and the findings on those errors.

The analytical expressions of the GPR measurement errors were obtained in section 2.4. They are:

- The error $\bar{\varepsilon}_{soil}$ due to fault-current injection caused substation soil potential change: $\bar{\varepsilon}_{soil} = \mathbf{T}\mathbf{Y}_M^{-1}\mathbf{G} \Big/ \left(2\pi S_{grid}\right)$ as shown in (2.10).

- The error $\bar{\varepsilon}_{ind}$ due to voltage-sag caused induction: $\bar{\varepsilon}_{ind} = (\mathbf{T}\mathbf{Y}_M^{-1}\mathbf{H} + Z_{mn})\left(3Z_{sys} + Z_{T0}\right) \Big/ \left(Z_{sys} Z_{M0}\right)$ as shown in (2. 20).

- The errors $\bar{\varepsilon}_{Fgrid}$, $\bar{\varepsilon}_{Fsoil}$ and $\bar{\varepsilon}_{Find}$ due to the fault current: $\bar{\varepsilon}_{Fgrid} = 1 \big/ (2\pi d_f S_{sys})$, $\bar{\varepsilon}_{Find} = (\mathbf{T}\mathbf{Y}_M^{-1}\mathbf{Q} + Z_{mn}^F) \big/ Z_{sys}$ and $\bar{\varepsilon}_{Fsoil} = \mathbf{T}\mathbf{Y}_M^{-1}\mathbf{P} \Big/ \left(2\pi S_{sys}\right)$ as shown in (2.22), (2.27) and (2.29), respectively.

It is also shown in (3.31) that the total substation grounding impedance estimation error $\bar{\varepsilon}$ is $\bar{\varepsilon} = \bar{\varepsilon}_{soil} + \bar{\varepsilon}_{ind} + \bar{\varepsilon}_{Fgrid} - \bar{\varepsilon}_{Find} - \bar{\varepsilon}_{Fsoil}$.

The parameters in all the errors' analytical equations of (2.10), (2.20), (2.22), (2.27), and (2.29) are detailed and listed as follows:

$\boldsymbol{Y}_M$ is the admittance matrix of the neutral M circuit in the dimension of $n \times n$. n is the number of grounding rods of neutral M. This matrix is composed of the grounding resistance R_{gk} of each

rod, and the series impedance Z_{sk} in each span. The subscript "k" denotes a specific rod or span. $k = 1, 2, \cdots, n$.

$$\mathbf{T} = [1 \quad 0 \quad \cdots \quad 0]$$

$$\mathbf{G} = [1/(d_1 R_{g1}) \quad \cdots \quad 1/(d_n R_{gn})]^T$$

$$\mathbf{H} = \left[Z_{m1}/Z_{s1} \quad \left[Z_{m(i+1)}/Z_{s(i+1)} - Z_{mi}/Z_{si}\right]_{1\times(n-2)} \quad - Z_{m(n-1)}/Z_{s(n-1)}\right]^T$$

$$\mathbf{P} = [1/(d_{f1} R_{g1}) \quad \cdots \quad 1/(d_{fn} R_{gn})]^T$$

$$\mathbf{Q} = \left[Z^F_{m1}/Z_{s1} \quad \left[Z^F_{m(i+1)}/Z_{s(i+1)} - Z^F_{mi}/Z_{si}\right]_{1\times(n-2)} \quad - Z^F_{m(n-1)}/Z_{s(n-1)}\right]^T$$

d_k is the distance between the k^{th} rod of neutral M and the center of the grounding grid.

d_{fk} is the distance between the k^{th} rod of neutral M and the fault point on the ground surface.

Z_{mk} is the mutual impedance between neutral M and phase conductors in the k^{th} span.

Z^F_{mk} is the mutual impedance between neutral M and the faulted feeder in the k^{th} span.

Z_{M0} is the zero sequence impedance downstream feeder M.

Z_{T0} is the zero sequence impedance of the substation transformer.

Z_{sys} is the substation grounding system impedance, including the substation grounding grid, transmission shield wires, and feeder neutrals that are connected to the substation grounding grid.

S_{sys} is defined as Z_{sys}/ρ.

Z_{grid} is the substation grounding grid impedance.

S_{grid} is defined as Z_{grid}/ρ. It can be approximately estimated using (2.33) [22], where A is the area occupied by the substation grounding grid. The approximations of S_{grid} for some typical sizes of distribution substations are shown in Table 2.3.

$$S_{grid} = \frac{Z_{grid}}{\rho} \approx \frac{1}{4}\sqrt{\frac{\pi}{A}} \tag{2.33}$$

Table 2.3 Approximations of $\boldsymbol{S_{grid}}$ for typical sizes of distribution substations

Size (m×m)	**30×30**	**50×50**	**90×90**	**100×100**	**150×150**
$\boldsymbol{S_{grid}}$	0.0148	0.0087	0.0049	0.0043	0.0030

For simplicity of investigation, it is first assumed that neutral M lies in a straight line and uses the same conductor in each span. Thus, two independent parameters of neutral M, span length L_s and total length L_M, can be used to replace the contributing factors d_k, Z_{sk}, Z_{mk}, and n identified in the error equations of (2.10), (2.20), (2.22), (2.27) and (2.29), since $d_k = d_1 + (k-1)L_s$, $Z_{sk} = Z_s L_s$, $Z_{mk} = Z_m L_s$, and $n = L_M/L_s$, where d_1 is the distance between the 1st rod of neutral M and the center of the grounding grid, Z_s is the self-impedance of the neutral M conductor per meter (in Ω/m), Z_m is the mutual impedance of neutral M and phase conductors per meter (in Ω/m).

2.6.1 Error Due to Fault-Current Injection Caused Substation Soil Potential Change

The absolute value of this error, ε_{soil}, can be written as

$$\varepsilon_{soil} = \left|\frac{S_{grid.B}}{S_{grid}}\right|\left|\frac{\mathbf{TY}_M^{-1}\mathbf{G}}{2\pi S_{grid.B}}\right| = k_{Sgrid}\varepsilon_{soil.B} \tag{2.34}$$

where the subscript 'B' indicates the base case shown in section 2.5. $S_{grid.B} = 0.0087$. k_{Sgrid}=$\left|S_{grid.B}/S_{grid}\right|$.

Equation (2.34) shows that the error is caused by two factors: neutral M and S_{grid}. The base case error $\varepsilon_{soil.B}$ only varies with the total length, span length, and grounding resistance of neutral M. In practice, the neutral span length is generally between 50m and 400m [73], and the grounding resistance may vary from 5Ω to 100Ω due to the soil resistivity variation. Notice that the neutral's grounding resistance should be normally maintained at around 25Ω or less [74]. The base case errors with varied total length, span length, and grounding resistance of neutral M are shown in Figure 2.21.

As expected, $\varepsilon_{soil.B}$ decreases with the increase of the total length of neutral M and approaches a saturated value when neutral M is longer than 2~4km. This can be understood as follows: the transfer voltages in the soil at the first several rods of neutral M are much higher than those at the remote rods. As a result, the resulting voltage at the substation terminal of neutral M stays a constant, and thus the error is no longer changed when more spans are added to the remote end, i.e., neutral M becomes longer. Also, $\varepsilon_{soil.B}$ increases with the decrease of grounding resistance and span length of neutral M.

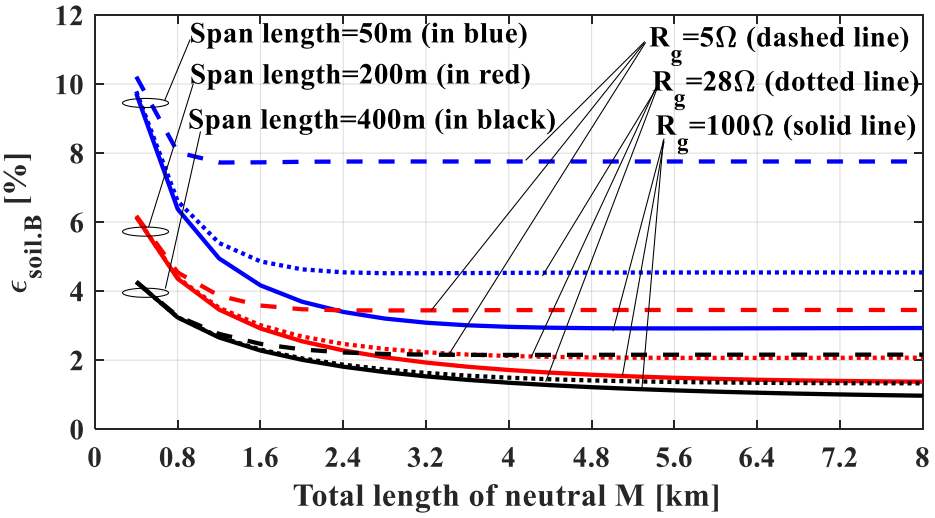

Figure 2.21 Error $\boldsymbol{\varepsilon_{soil.B}}$ for neutral M with different total lengths, span lengths, and grounding resistances

Furthermore, the coefficient k_{Sgrid} in (2.34) suggests that S_{grid} for any other grounding grids may result in 0.59~2.91 times of error $\varepsilon_{soil.B}$. In the worst-case situation in which the substation

area is 150m×150m, the maximum value of error ε_{soil} is about 23% if the neutral M is longer than 1km. This error increases with the increase of the substation grounding grid area.

The coefficient k_{Sgrid} can also be interpreted as the indicator of the deterioration of the grounding grid for a given substation. When the grounding grid condition becomes worse, the value of k_{Sgrid} becomes smaller, resulting in a lower error.

Additionally, when neutral M does not leave the substation in a straight route in some suburban situations, the substation grounding grid's transfer voltages on some neutral M rods, especially the far-end rods, will be higher than those of the straight-line case used in the base case. This will only slightly increase the error ε_{soil}, due to the neutral M rods experiencing similar transfer voltages when they are more than $5D_{grid}$ (D_{grid} stands for the diameter of the grounding grid) from the center of the grounding grid as shown in Appendix A. In a very unfavourable situation adapted from the base case that the neutral M has its first 2 rods (i.e., the first 200m) in a straight route and the other rods are all 200m away from the grounding grid, the error ε_{soil} is 8.42%, which is still acceptably low. If the straight route section is 400m and the other rods are 400m away from the substation grounding grid, the error ε_{soil} is 5.19%. The increase is only 2.06%, compared with the base case error $\varepsilon_{soil.B}$ of 3.13%. For substations situated in downtowns, more research is needed as ungrounded feeder neutrals are more likely used for power distributions.

2.6.2 Error Due to Voltage Sag Caused Induction

The absolute value of this error ε_{ind} can be written as

$$\varepsilon_{ind} = \left| \frac{(3+\frac{Z_{T0}}{Z_{sys}})}{(3+\frac{Z_{T0.B}}{Z_{sys.B}})} \right| \left| \frac{Z_{M0.B}}{Z_{M0}} \right| \left| \frac{(\mathbf{T}\mathbf{Y}_M^{-1}\mathbf{H} + Z_{mn})(3Z_{sys.B} + Z_{T0.B})}{Z_{sys.B}Z_{M0.B}} \right| = k_{T0}k_{M0}\varepsilon_{ind.B} \tag{2.35}$$

where $k_{T0} = \left|(3 + Z_{T0}/Z_{sys})/(3 + Z_{T0.B}/Z_{sys.B})\right|$, $k_{M0} = |Z_{M0.B}/Z_{M0}|$. $Z_{sys.B} = 0.4054\Omega$, $Z_{T0.B} = 0.9446\Omega$, and $Z_{M0.B} = 48\Omega$.

There are two coefficients. The first one, k_{T0}, is determined by both the grounding system impedance and the zero sequence impedance of the substation transformer. The second one, k_{M0}, is determined by the zero sequence impedance of feeder M and its downstream loads.

The base case error, $\varepsilon_{ind.B}$, varies with the neutral length and its span length and grounding rod resistance, as shown in Figure 2.22. The error increases with the increase of the total length, span length, and grounding resistance of neutral M. The error becomes constant when the total length exceeds certain values. The shorter span length and the lower grounding resistance of neutral M are beneficial in reducing the error. If the total length of neutral M is less than 7km, the base case error can be limited to below 10%.

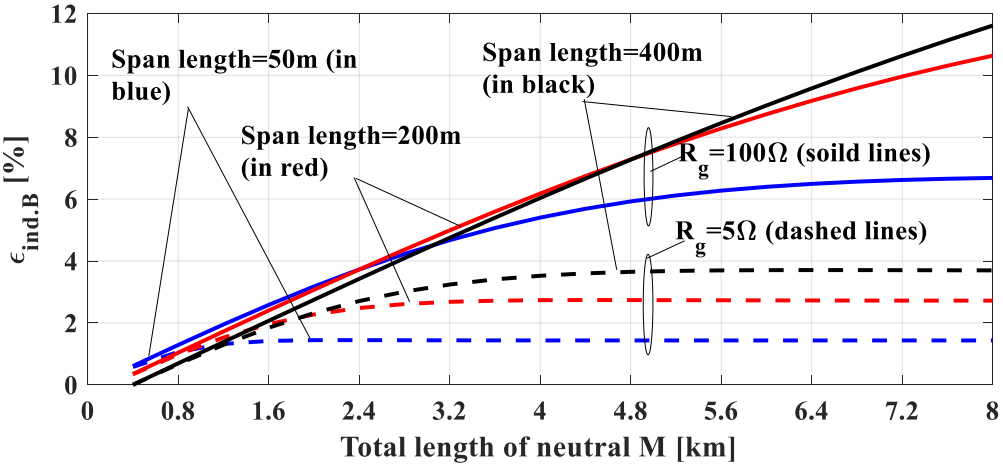

Figure 2.22 Error $\varepsilon_{ind.B}$ for neutral M with different total lengths, span lengths, and grounding resistances

Coefficient k_{T0} contains Z_{sys} and zero sequence impedance of transformer, Z_{T0}. The size of transformers in distribution substations may range from 25MVA to 250MVA. Their Z_{T0} seen at the secondary side is in a range of 1.25Ω~0.125Ω at the base of 25kV (assume Z_{T0}%=5%). If Z_{sys} is fixed at the base value 0.4054Ω, the transformer size will change k_{T0} between 0.62~1.14, causing a limited impact on error ε_{ind}. If a base value 0.9446Ω is assigned to Z_{T0}, k_{T0} changes from 1.45~0.65 when Z_{sys} increases from 0.2Ω to 2Ω. The maximum range for k_{T0} is 0.57~1.74.

Coefficient k_{M0} mainly depends on the load level of feeder M. The lighter the loading is, the larger the impedance will be. In the base case, $Z_{M0.B}$ is 48Ω as the feeder M has a Y_g connected loading of 13MVA, neglecting the zero sequence impedance of feeder M conductors. Table 2.4 shows the values of Z_{M0} for different loadings in the Y_g connection. Hence, k_{M0} can be in a range of 0.19~1.92, when the loading ranges from 2.5MVA ~ 25MVA. Therefore, the low loading significantly helps to reduce the error.

Table 2.4 Interpretation of $\boldsymbol{Z_{M0}}$ from loadings of a 25kV feeder

Loading (MVA)	**25**	**12.5**	**8.3**	**5**	**2.5**
$\boldsymbol{Z_{M0}}$ **(Ω)**	25	50	75	125	250

It should be noted that some industrial loads can be supplied by three-phase service transformers connected in Delta [75]. These loads provide no zero sequence currents to the fault-caused voltage sag. Hence, the actual Z_{M0} can be larger than the above loading-based estimations, which in turn will decrease the coefficient k_{M0} and the error ε_{ind}.

Combining the ranges of k_{T0} and k_{M0}, one can have

$$\varepsilon_{ind} = (0.11 \sim 3.34) \times \varepsilon_{ind.B} \tag{2.36}$$

Equation (2.36) shows that all factors other than neutral M may result in 0.11~3.34 times the variation on the base case error. This error should be reduced. Since the substation grounding impedance is not under control, using a low load feeder M is critical to reducing this error.

2.6.3 Errors Due to Fault Current

The fault current causes errors from three aspects, changing the soil potential at the substation, inducing EMFs in the neutral M, and changing the soil potential at grounding rods of neutral M. They are studied in the following.

2.6.3.1 Soil Potential Change at Substation

The absolute error ε_{Fgrid} can be written as

$$\varepsilon_{Fgrid} = \left|\frac{\rho S_{sys.B}}{\rho S_{sys}}\right| \left|\frac{1}{2\pi d_f S_{sys.B}}\right| = k_{Zsys}\varepsilon_{Fgrid.B} \tag{2.37}$$

where k_{Zsys}=$\left|Z_{sys.B}/Z_{sys}\right|$.

This error is inversely proportional to S_{sys} and d_f, i.e., the distance between the fault point and the substation. The sensitivity study results are shown in Figure 2.23. The base case error $\varepsilon_{Fgrid.B}$<3.9% when d_f>1km. Since Z_{sys} may range between 0.2Ω~2Ω and the base case $Z_{sys.B}$ is 0.4054Ω, k_{Zsys} can range between 0.2~2. Hence, ε_{Fgrid}<7.8%.

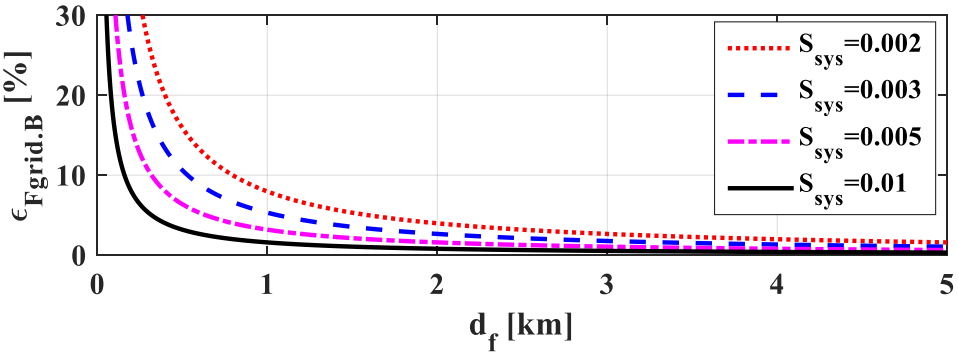

Figure 2.23 Error $\varepsilon_{Fgrid.B}$ for different fault locations

2.6.3.2 Inducing Voltages on Neutral M Conductors

The severity of the inductive interference is strongly dependent on the distance between the current-carrying feeder and the targeted conductor. Since all feeders start from the substation, the angle θ between the faulted feeder and neutral M becomes an essential factor affecting the induction caused error, as shown in Figure 2.24.

The absolute value of this error ε_{Find} can be written as

$$\varepsilon_{Find} = \left| \frac{Z_{sys.B}}{Z_{sys}} \right| \left| \frac{\mathbf{TY}_M^{-1}\mathbf{Q} + Z_{mn}^F}{Z_{sys.B}} \right| = k_{Zsys}\varepsilon_{Find.B} \tag{2.38}$$

For the base case d_f=3km, the variation of error $\varepsilon_{Find.B}$ with the separation angle θ is shown in Figure 2.25. The results for different d_f are also compared in this figure. One can see from Figure 2.25 that the angle θ is indeed the dominant contributing factor to error $\varepsilon_{Find.B}$. By contrast, the fault distance d_f has negligible impacts on this error when $d_f \geq$1km. The error is less than 12% if $45° \leq \theta \leq 315°$ is satisfied.

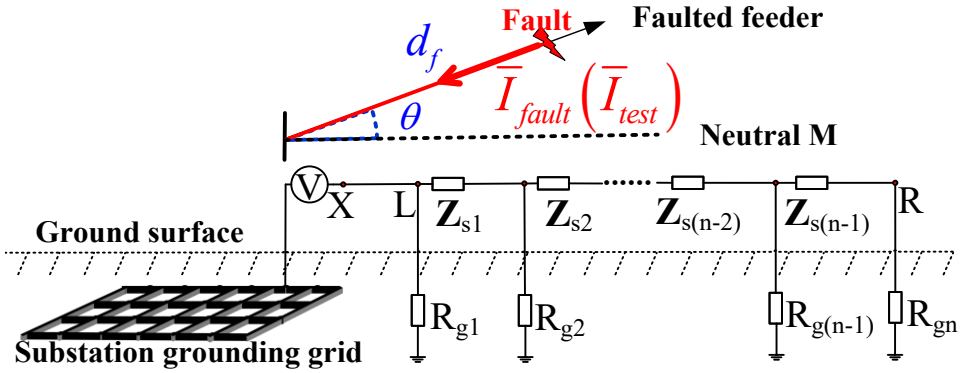

Figure 2.24 Illustrations of the faulted feeder at an angle $\boldsymbol{\theta}$ to neutral M and the fault point location to the substation

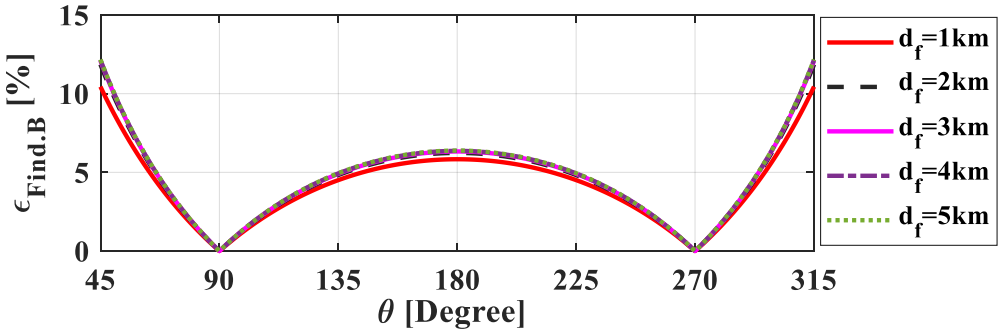

Figure 2.25 Error $\boldsymbol{\varepsilon_{Find.B}}$ for different fault point locations and angles between the faulted feeder and neutral M

Furthermore, at the angles of θ=45° and θ=180°, the error ε_{Find} caused by different neutral M parameters, using the base case data (d_f=3km), is shown in Figure 2.26. One can see that the error ε_{Find} increases with the increase of the total length, span length, and grounding resistance of

neutral M. When the total length is longer than 2~4km, this error enters the saturated area. This error is sensitive to the span length. A shorter span length is beneficial for reducing this error. With angles of θ=45° and θ=180°, the error ranges from 7~16% and 4.5~7.5%, respectively.

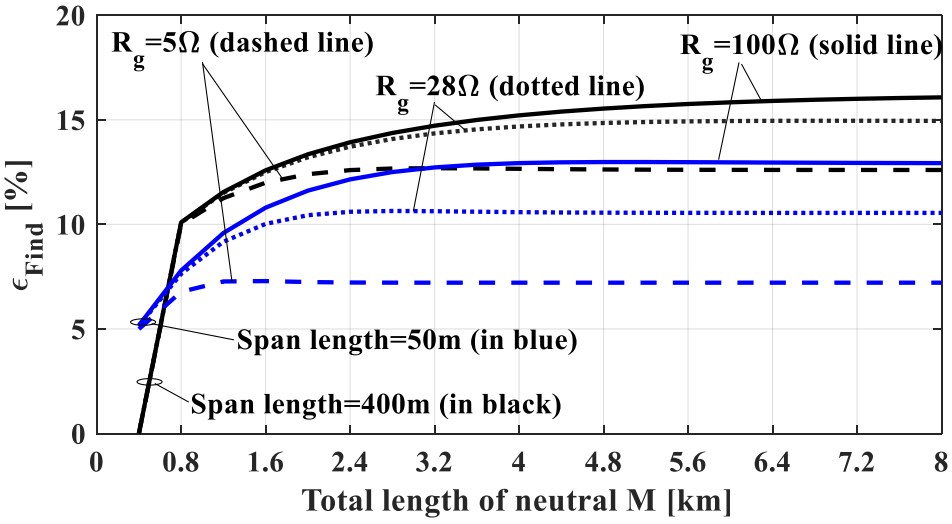

(a) θ=45°

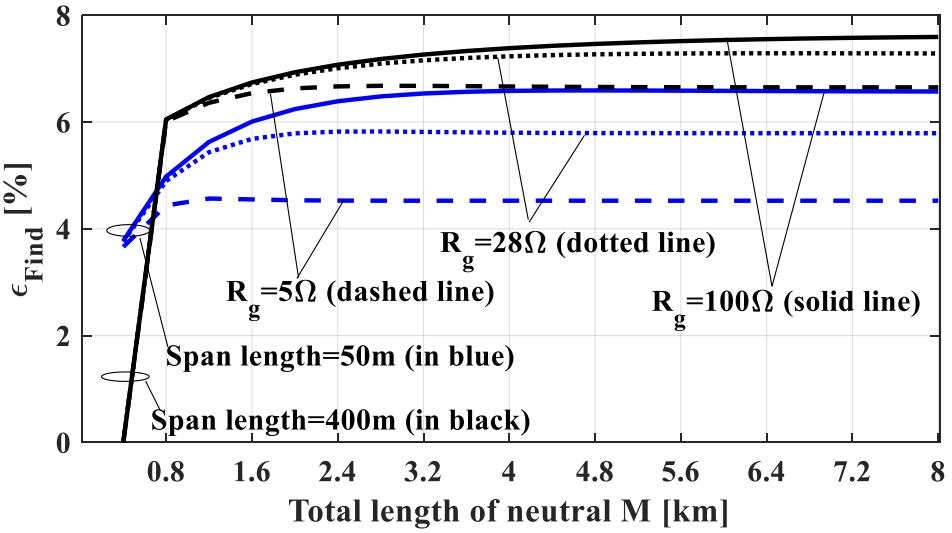

(b) θ=180°

Figure 2.26 Error ε_{Find} for neutral M with different total lengths, span lengths, and grounding resistances

As k_{Zsys} may range between 0.2~2, the maximum value of this error ε_{Find} can be about 32% in an extreme case. Fortunately, this case only happens when the impedance Z_{sys} is very small as

0.2Ω, i.e., the substation grounding grid is under excellent condition. Once the substation grounding grid condition declines, the error decreases dramatically.

Additionally, the angle θ between 45° and 315° is only for the beginning section of the faulted feeder. Take the most adverse situation as an example: assume that the faulted feeder has its beginning section in θ=45° and the rest section of infinite length is parallel with neutral M. The error ε_{Find} for different distances between the rest section of the faulted feeder and neutral M is shown in Figure 2.27.

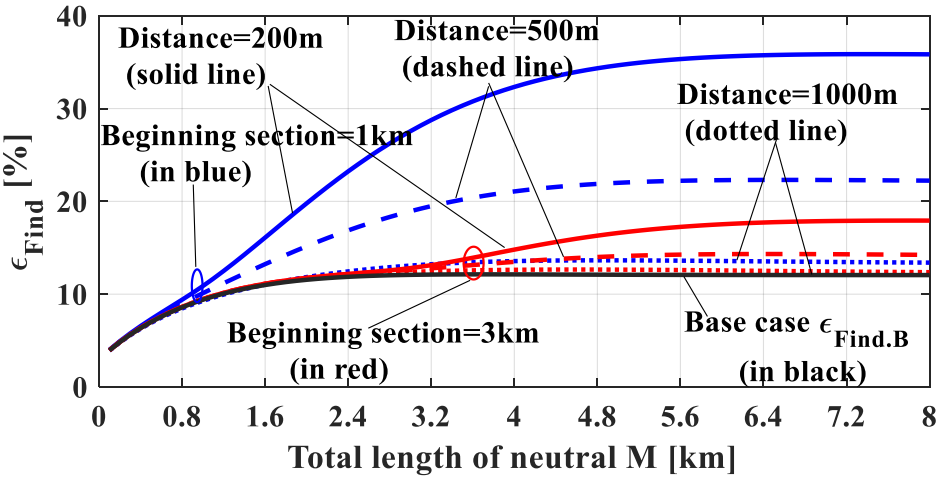

Figure 2.27 Error $\boldsymbol{\varepsilon_{Find}}$ for different distances between neutral M and the rest section of the faulted feeder when $\boldsymbol{\theta}$ is 45° for the beginning section of the faulted feeder

One can see from Figure 2.27 that the error ε_{Find} is almost unchanged if the rest section of the faulted feeder is parallel to the neutral M with a separated distance of 1000m. The error is 35.8% at most when the distance is reduced to 200m. Considering the different routes of outgoing feeders in practice, $45° \leq \theta \leq 315°$ is only required for the first 1km around the substation. The rest section of the faulted feeder would have an insignificant impact on the error ε_{Find} unless it is in a close parallel with neutral M.

2.6.3.3 Soil Potential Change at Neutral M Rods

The absolute value of this error ε_{Fsoil} can be written as

$$\varepsilon_{Fsoil} = \left| \frac{\rho S_{sys.B}}{\rho S_{sys}} \right| \left| \frac{\mathbf{T}\mathbf{Y}_M^{-1}\mathbf{P}}{2\pi S_{sys.B}} \right| = k_{Zsys}\varepsilon_{Fsoil.B} \tag{2.39}$$

For the base case, the error $\varepsilon_{Fsoil.B}$ is expressed using the green contour lines in Figure 2.28. One can see that the error $\varepsilon_{Fsoil.B}$ is lower than 4% when the fault occurs in the red highlighted area in the figure, i.e., $d_f \geq$1km and 45° $\leq \theta \leq$315°.

As discussed, k_{Zsys} may range between 0.2~2. The error ε_{Fsoil} for any substations can always be lower than 8%.

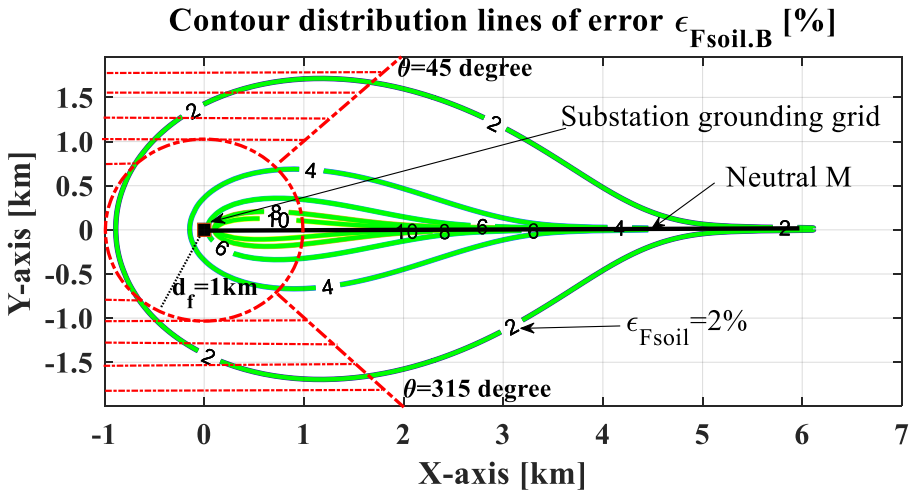

Figure 2.28 Error $\varepsilon_{Fsoil.B}$ for different fault locations

2.6.4 Impact of Non-Uniform Neutral M Parameters

So far, the sensitivity studies assume that the parameters of neutral M are uniform. However, grounding resistance and span length may vary in a neutral M at different rods and span sections. Thus, some study results are presented here to show the impacts of non-uniform grounding resistance and span length of neutral M on the estimation error $\bar{\varepsilon}$. The studies are done by conducting Monte Carlo Simulations on the case for the verification studies in section 2.5.

2.6.4.1 Non-Uniform Grounding Resistance of Neutral M

In this Monte Carlo Simulation, each grounding resistance of neutral M is randomly selected from a lognormal distribution with a median value of 100Ωm and 95% below 2000Ωm [76]. The absolute value of error $\bar{\varepsilon}$ is then computed. The error results from one million simulation events are presented in Figure 2.29. It can be found that 95% of the simulation events have an error $\bar{\varepsilon}$ less than 14.33%, and all the errors are within 9.5%~16.5%. They are close to the error of 13.91% in the uniform grounding resistance case. Hence, one can conclude that the non-uniform grounding resistance of neutral M has no significant influence on the proposed method.

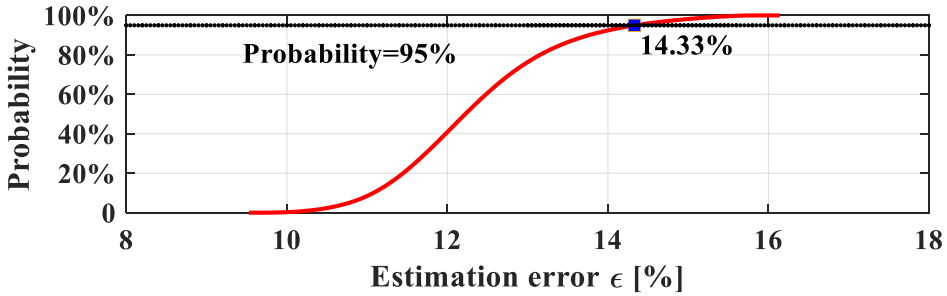

Figure 2.29 Monte Carlo Simulation results of $\boldsymbol{\varepsilon}$ for soil resistivity variation

2.6.4.2 Non-Uniform Span Length of Neutral M

A truncated lognormal distribution is used to select the non-uniform span length. The lognormal distribution has a median value of 100m, with 95% below 150m and a cutoff at 500m. The Monte Carlo Simulation is done according to the following steps. An individual value is randomly generated from the model for one neutral M span. This step is repeated until the lengths of all the spans are randomly assigned. The total error is then computed. The simulation is repeated one million times, and the results are presented in Figure 2.30. It can be found that 95% of the simulation events have an estimation error $\bar{\varepsilon}$ less than 14.21%, and all the errors are in a small range between 13% and 15%. Therefore, one can conclude that the non-uniform span length of neutral M has a negligible impact on the proposed method.

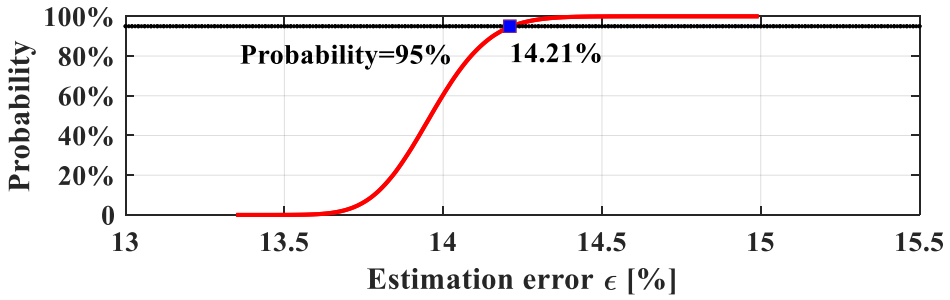

Figure 2.30 Monte Carlo Simulation results of $\boldsymbol{\varepsilon}$ for non-uniform span length

2.6.5 Summary of Findings and Implementation Guide

The sensitivity studies show that many factors may affect measurement accuracy. All errors can be expressed as a base case error multiplied by their coefficients. The coefficients and the base case errors for the five errors are summarized in Table 2.5. The conditions to obtain those value ranges are also presented.

Table 2.5 Value ranges for each coefficient and base case error

Error	k and ε	Value range	Conditions
ε_{soil}	k_{Sgrid}	0.59~2.91	When S_{grid} increases
	$\varepsilon_{soil.B}$	<8%	When neutral M length > 1km
ε_{ind}	k_{T0}	0.57~1.74	When Z_{T0} increases and Z_{sys} decreases
	k_{M0}	0.19~1.92	When the load level increases
	$\varepsilon_{ind.B}$	<10%	When neutral M length < 7km
ε_{Fgrid}	k_{Zsys}	2~0.2	When Z_{sys} increases
	$\varepsilon_{Fgrid.B}$	<3.9%	When the fault is 1km away from the substation, i.e., d_f>1km
ε_{Find}	k_{Zsys}	2~0.2	When Z_{sys} increases
	$\varepsilon_{Find.B}$	<16%	When d_f>1km and the faulted feeder is θ apart from the feeder M (45°<θ<315°) for the first 1km
ε_{Fsoil}	k_{Zsys}	2~0.2	When Z_{sys} increases
	$\varepsilon_{Fsoil.B}$	<4%	When d_f>1km and 45°<θ<315°

The base case error studies suggest the most critical factors are the length of neutral M and the fault location. As long as the neutral M length is within 1~7km, the fault occurs 1km away from the substation, and the faulted feeder is θ=45° apart from the feeder M, the five errors can be limited to 8%, 10%, 5%, 16%, and 4%, respectively, as shown in Table 2.5.

When some parameters — such as the substation grounding grid condition, the substation transformer's zero sequence impedance, the load level of feeder M — are different from those in the base case, coefficients k_{Sgrid}, k_{Zsys}, k_{T0} and k_{M0} are used to qualify their impacts by multiplying the coefficients by the base case error. Furthermore, all the errors are affected by the substation grounding grid condition. However, when the grounding grid condition worsens, all the coefficients k_{Sgrid}, k_{Zsys} or k_{T0} decrease, which means all the errors can be less than the base case error.

Error ε_{ind} has two coefficients, k_{M0} increases with the increase of the load level of feeder M. The light-loaded feeder M can significantly reduce this error. Coefficient k_{T0} is determined by the substation transformer's zero sequence impedance and the grounding system impedance that is mainly dependent on the grounding grid condition. Careful selection of neutral M can help improve measurement accuracy.

The observation and analysis lead to the following guide for the implementation of the proposed method.

1) **Selection of Feeder M/Neutral M:** A feeder far away from other feeders should be selected as feeder M. This allows more faulted feeders to act as the test current loop. This feeder should also have an isolated neutral with a length longer than 1km. The ideal length for neutral M is between 1~7km. If multiple feeders satisfy the above requirements, the light-loaded feeder should be selected first.

2) **Selection of Fault Location:** Only phase-to-ground faults occurred at more than 1km away from the substation and at the feeders that have their first 1km route more than 45° apart from the feeder M are used for the grounding impedance estimation.

3) **Estimation of Error Range**: For a given substation, the substation area and layout, transformer and neutral M parameters, the load level of feeder M are known. Therefore, the base case errors and coefficients can be more accurately estimated. With the estimated error ranges, the accuracy of measurements can be better understood.

2.7 Application Studies

The application process for the proposed online method is presented in this section. The results of an application study prove the feasibility and effectiveness of the proposed method.

2.7.1 Process of Implementation and Application

The proposed method can be implemented according to the following steps:

Step 1 (Applicability Check): The substation should consist of Δ-Y_g connected transformers and feeders with neutrals. This type of substation accounts for most of the rural and urban distribution substations in North America.

Step 2 (Information Collection): Collect the electrical and geographic information of the substation. This includes the configurations of grounding grid and grounding system, power transformer, routes of power lines and ground wires, rough load levels of each feeder, and the total length and span length of each neutral. It is also preferred, but not necessary, to collect historical testing data of soil resistivity and substation grounding impedance.

Step 3 (Installation Planning): Select the neutral M and potential fault feeders based on the guide provided in section 2.6.5. Estimate each error range based on the information obtained in Step 1.

Step 4 (Measurement Setup): The measurement setup is completed by adding a connection wire between the first rod of neutral M and one terminal of a voltage monitor installed in the substation. The other terminal of the voltage monitor is connected to the substation grounding grid. Also, current monitors are placed at each transformer neutral and at the feeder neutral bonding conductor (this is optional). A relay-like processing unit is used to collect the synchronized voltage and

current measurements and the fault-related information. It also processes the raw measurement data and runs the online monitoring.

Step 5 (Online Monitoring): For each selected fault, a substation grounding impedance is estimated based on the guide in section 2.6.5. A trend of multiple grounding impedances can be created over time. An increasing trend will reveal the degradation of grounding grid conditions.

2.7.2 Case Studies

In the application studies, the basic substation information is the same as that used in the verification studies. This study mimics the grounding grid degradation and soil resistivity variation to show what the online monitoring results look like.

The soil is assumed to be in two layers. The resistivity of the top layer soil varies during yearly normal, raining, and freezing seasons, as shown in Table 2.6 [55]. The depth of the top layer is 1.6m. It is further assumed in the base case (see Figure 2.12) that there are nine single-phase-to-ground faults on the feeders 1~3 in each year of the 5-year online monitoring. These faults evenly occur in the three seasons on the feeders 1~3. The locations of all these faults (45 in total) are set randomly and differently at a distance between 1km and 5km away from the substation.

Table 2.6 Soil resistivity information

Soil resistivity (Ωm)	**Normal season**	**Freezing season**	**Raining season**
Top layer	100	1000	10
Bottom layer	100	100	100

The study assumes that the substation grounding grid gradually deteriorates due to corrosion over the monitoring period. The grounding grid degradation process can be represented by an increasing grounding grid impedance Z_{grid}. To achieve this goal, one can incrementally increase the grounding grid parameter S_{grid} in the assumed 45 tests from the base case value of 0.0087 to 0.04 under the seasonal soil resistivities shown in Table 2.6. The simulation results of substation grounding impedance are shown in Figure 2.31.

It can be seen in Figure 2.31 that an increasing trend of these grounding impedances can be found, indicating that the grounding grid is in the process of degradation. The occasional results, such as A, B, and C in the figure, are insufficient to tell this truth. The true values of the substation grounding impedances are also compared in the figure. The total errors are between 4.38% and 13.90%.

Using the given substation information, the errors are estimated and presented in Table 2.7. Compared to those in Table 2.5, the ranges of these errors are narrowed down, providing more confidence in the results.

Table 2.7 Error ranges for the application case

Errors	Coefficients	Base case errors
ε_{soil} < 7.9%~1.3%	k_{Sgrid}=1~0.22	$\varepsilon_{soil.B}$ < 7.9%
ε_{ind} < 8.6%~5.1%	k_{T0}=1.1~0.65 and k_{M0}=1	$\varepsilon_{ind.B}$ < 7.8%
ε_{Fgrid} < 4.7%~0.1%	k_{Zsys}=1.2~0.20	$\varepsilon_{Fgrid.B}$ < 3.9%
ε_{Find} < 17.0%~2.8%	k_{Zsys}=1.2~0.20	$\varepsilon_{Find.B}$ < 14.2%
ε_{Fsoil} < 4.8%~0.8%	k_{Zsys}=1.2~0.20	$\varepsilon_{Fsoil.B}$ < 4.0%

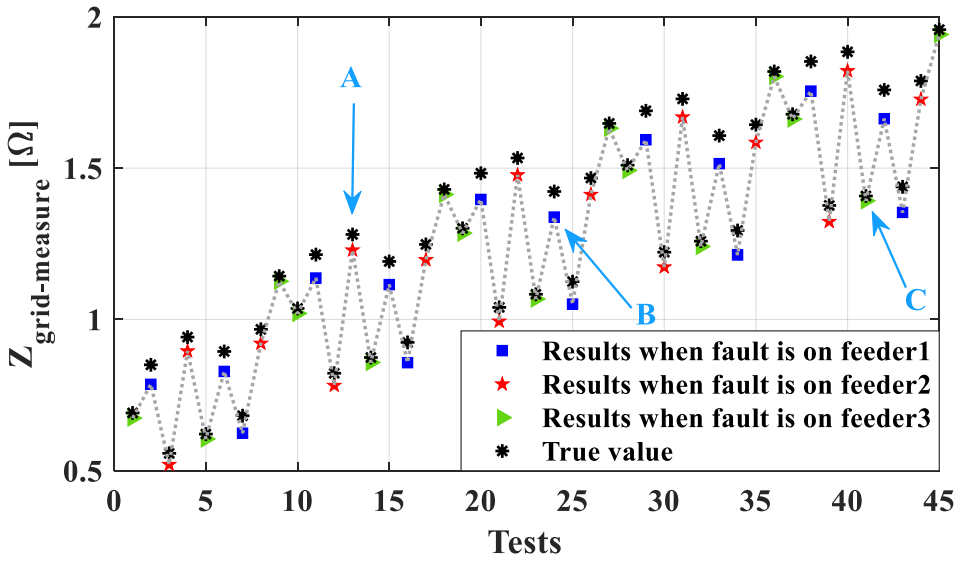

Figure 2.31 Results of substation grounding impedance

2.8 Discussion on the Impact of Substation Configurations

The proposed method is intended for distribution substations in North America. Many of such substations supply feeders using Δ-Y_g connected transformers due to protection requirements. For a distribution or transmission substation consisting of Y_g-Y_g connected transformers, this method may not be applicable. This is mainly because the zero sequence fault current in each incoming transmission line during an unbalanced ground fault may produce an additional but significant induced voltage on the neutral M. To avoid this additional inductive interference and the inductive interference from feeder currents at the same time, one may fail to select a qualified feeder M / neutral M for the GPR measurement. Also, the induced currents in the transmission shield wires will significantly impact measurement accuracy. Fortunately, this issue can be solved by excluding all shield wires in the substation grounding impedance measurement, at the cost of deploying additional current measurements at the connecting points of each shield wire and the grounding grid. The method may be applicable for transmission substations if Δ-Y_g transformers are used. When no outgoing feeders/neutrals are available, a dedicated test lead for the GPR measurement should be designed and permanently installed to act as neutral M, and measurement accuracy should be assessed having regard to different configurations between distribution and transmission facilities.

It is also worth noting that the distribution substations in Asia and Europe may supply ungrounded or resonant grounded feeders. Ground fault currents are very small. The proposed method cannot work for such substations, at least directly. However, further research may show how the method may be extended by utilizing ground fault currents on the transmission lines.

2.9 Conclusion

This chapter presents an online method for continuously and automatically measuring the substation grounding impedance. The proposed method uses naturally occurring fault currents as the test currents. The corresponding GPR is measured using an isolated multi-grounded neutral. The test current and potential loops are installed permanently. Over time, the trend of the grounding impedances estimated using the proposed method can provide a much more detailed picture of grounding grid conditions than an occasional single test result obtained using offline methods. The

main challenges faced by the proposed method are various interferences that can cause measurement inaccuracy. The main factors affecting the interference-caused errors are identified through analytical studies. Multiple ways to mitigate the impacts of those interferences are identified. Based on the sensitivity study results, a guide for selecting the feeder for the GPR measurement and the faults as “test current” sources has been developed. By following the guide and the proposed implementation requirements, reasonable measurement accuracy can be achieved. Furthermore, the estimated ranges of measurement errors due to different interference factors are provided to give users additional confidence in the results. The application study shows that the trend of impedance variation is a more useful indicator of the substation grounding grid conditions.

Chapter 3: Substation Grounding Grid Condition Monitoring Using Natural 3rd Harmonic Currents

This chapter proposes an improved method for online substation grounding grid condition monitoring. The proposed method overcomes the main limitations of the fault-current-based method presented in Chapter 2. As a result, it is applicable for all distribution and transmission substations.

3.1 Limitations of the Fault-Current-Based Method

The fault-current-based method presented in Chapter 2 has limitations. The method aims to take full advantage of existing facilities; specifically, it uses an isolated multi-grounded neutral (called the neutral M) for online GPR measurement. As a result, the neutral M inevitably suffers inductive interferences from the fault current on the power line nearby. Since it is not practical to redesign the existing feeder neutrals, the way to reduce such inductive interferences is to select an available neutral as the neutral M (for the GPR measurement) that is at a distance away from other power lines. This could limit the applications of the method if such a neutral/feeder is unavailable. Secondly, the method cannot work for substations with Y_g-Y_g connected transformers. In this case, transmission lines also contain zero sequence fault currents and thus may generate additional severe inductive interference on the neutral M, considering that outgoing neutrals for a substation are often limited in numbers. A third limitation is that the method requires natural phase-to-ground faults in the downstream distribution systems at certain locations. Thus, valid "test signals" may not occur as frequently as desired. Consequently, the method may fail to draw reliable conclusions on the grounding grid conditions over a specific period when there are insufficient functional natural faults.

3.2 Proposed Improvements

In order to overcome the limitations discussed above, additional research work has been conducted. This research has led to the invention of a multiwire technique for the GPR measurement. Combining this invention with the idea of using the 3rd harmonic current as a test signal has resulted in a much more versatile and effective online monitoring method.

3.2.1 A Multiwire Technique to Reduce Inductive Interference

As discussed earlier, inductive interference can cause difficulties in selecting neutral M for the fault-current-based method. One solution to this problem is to have a dedicated GPR measurement wire. However, this wire can also experience inductive interference. Through extensive research, we have developed a novel idea that can reduce inductive interference on the one hand and provide adequate GPR measurement on the other. The corresponding method is called the "multiwire GPR measurement technique," or simply the "multiwire technique." As shown in Figure 3.1, three measuring wires of different lengths are compacted together and laid below a power line which is the source of interference. It is worth noting that the large separation distances between measuring wires in Figure 3.1 are exaggerated for illustrative purposes only.

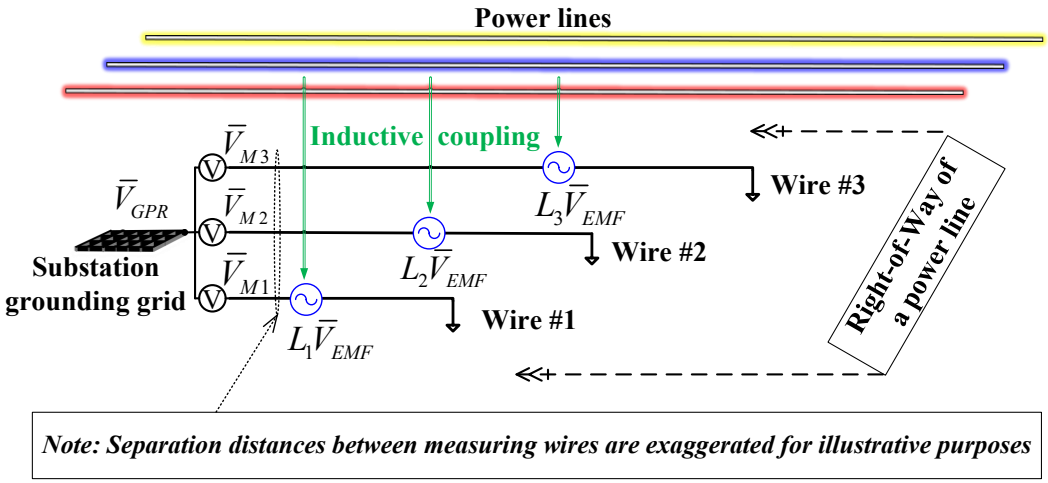

Figure 3.1 Illustration of the proposed multiwire GPR measurement technique

For the ith measuring wire ($i = 1, 2, 3$) in Figure 3.1, one can have the following equation:

$$\bar{V}_{Mi} = \bar{V}_{GPR} - L_i\bar{V}_{EMF} + \bar{e}_{ri} \tag{3.1}$$

where $\bar{V}_{Mi}$ is the voltage measured by the ith measuring wire's voltage monitor. $\bar{V}_{GPR}$ is the GPR of the substation grounding grid to be determined. $\bar{V}_{EMF}$ is the induced electromotive force (EMF per kilometer) on the measuring wire. L_i is the length of the ith measuring wire. $\bar{e}_{ri}$ is the measurement error of the voltage monitor at the ith measuring wire. This noise typically follows the Gaussian distribution [77-79].

Assuming there are three measuring wires, a least-square algorithm can be used to estimate the GPR while minimizing the sum of the squares of the monitors' measurement errors. The resulting solution is as follows:

$$\begin{bmatrix} \bar{V}_{GPR} \\ \bar{V}_{EMF} \end{bmatrix} = \left(\begin{bmatrix} 1 & -L_1 \\ 1 & -L_2 \\ 1 & -L_3 \end{bmatrix}' \begin{bmatrix} 1 & -L_1 \\ 1 & -L_2 \\ 1 & -L_3 \end{bmatrix} \right)^{-1} \begin{bmatrix} 1 & -L_1 \\ 1 & -L_2 \\ 1 & -L_3 \end{bmatrix}' \begin{bmatrix} \bar{V}_{M1} \\ \bar{V}_{M2} \\ \bar{V}_{M3} \end{bmatrix} \tag{3.2}$$

The technique's performance on inductive interference reduction has been verified through extensive field experiments. One illustrative case is presented in the following. As shown in Figure 3.2, a wire of 150m was laid under a 230kV transmission line to mimic an equivalent GPR at point A by receiving the inductive coupling from the overhead power line. This wire was called the "GPR-generating wire." Another four measuring wires in lengths of 25m, 50m, 75m, and 100m were laid in the opposite direction. All the measuring wires received inductive interference from the same power line. Their voltage measurements were used to estimate the equivalent GPR generated at point A by the GPR-generating wire. Each wire was grounded at the far-end using a grounding rod. Two power quality monitors were used in synchronization. Specifically, PQ monitor 1 with four channels was used for the measurements of the four measuring wires, while PQ monitor 2 measured the equivalent GPR at point A. Based on (3.2), the induced EMF per kilometer and the equivalent GPR at point A at both 60Hz and 180Hz were estimated using two measuring wires, three measuring wires, and four measuring wires, respectively. The estimated results were compared with the direct measurements as presented in Figure 3.3.

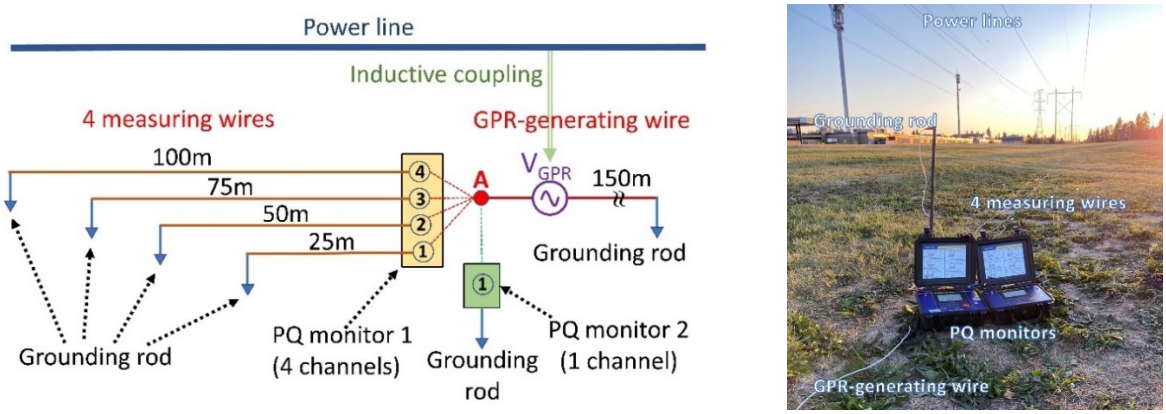

(a) Schematic diagram (b) Site picture

Figure 3.2 Description of the field experiments for the verification of inductive interference reduction

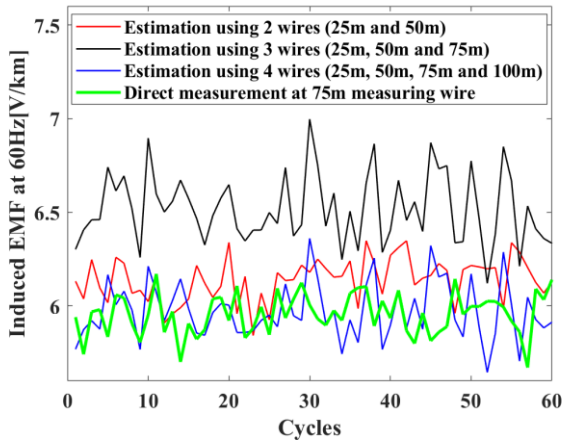

(a) Induced EMFs at 60Hz

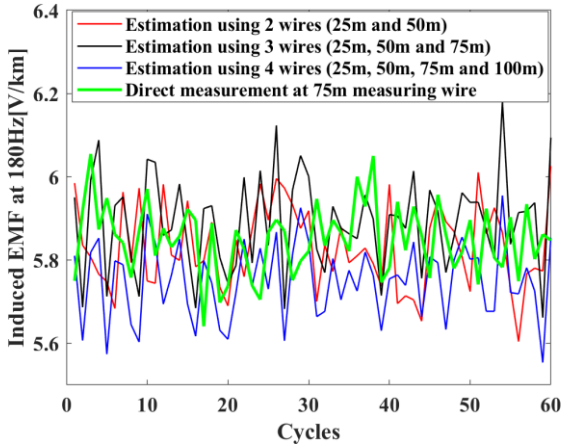

(b) Induced EMFs at 180Hz

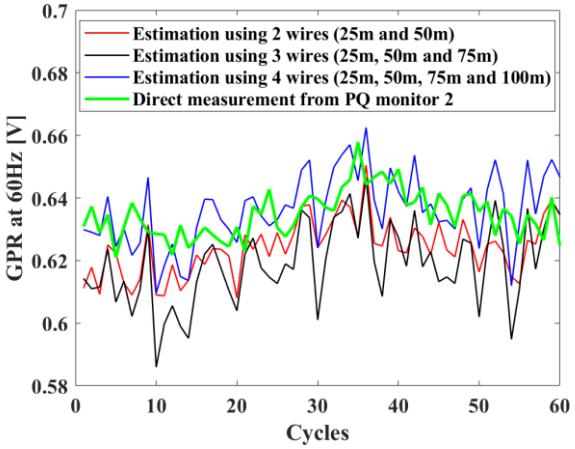

(c) GPR at 60Hz

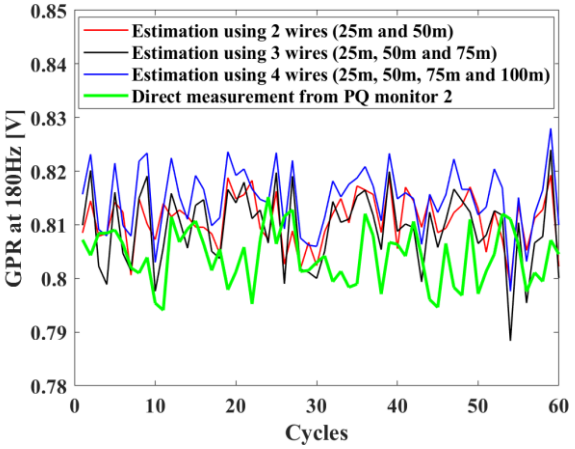

(d) GPR at 180Hz

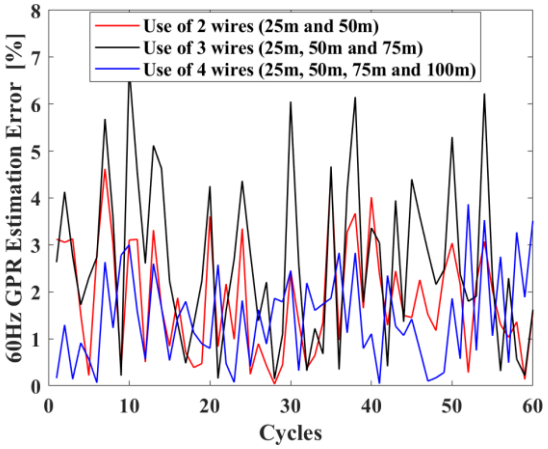

(e) Errors of 60Hz GPR estimation

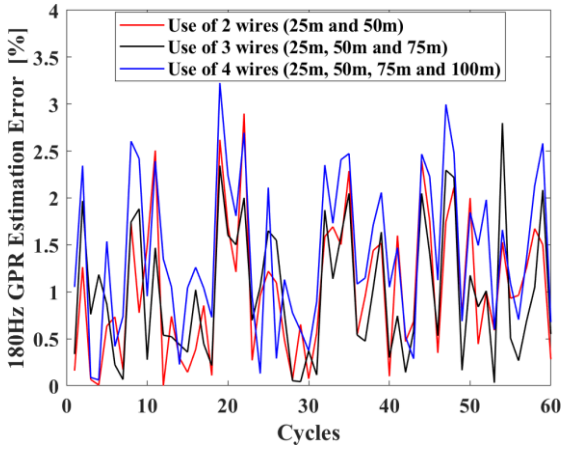

(f) Errors of 180Hz GPR estimation

Figure 3.3 Results of the field experiments for the verification of inductive interference reduction

The field experiment results show that the multiwire technique can significantly reduce the effect of inductive interference and thus estimate the GPR with good accuracy even under situations where the induced EMF is comparable to or higher than the GPR. Moreover, the addition of one or two more measuring wires and the least-square algorithm slightly increases the accuracy of GPR estimation.

The proposed multiwire technique can be easily implemented in a transmission line corridor or on a distribution feeder. The wires are individually grounded at different locations at the far end using regular grounding rods, which should not be very close to any buried metallic objects, such as tower/pole footing. The front end connects to the substation grounding grid with a voltage monitor at the substation edge. It is important to note that the measurements of the voltage monitor should be converted to digital signals first or be transmitted within the substation for processing using audio cables. This avoids inductive interference inside the substation.

- Implementation in a transmission line corridor

Figure 3.4 illustrates the implementation of the multiwire technique in a transmission line corridor using an actual case. The measuring wires can be shallowly buried parallel to the transmission lines in the corridor. No other additional work is needed in this implementation.

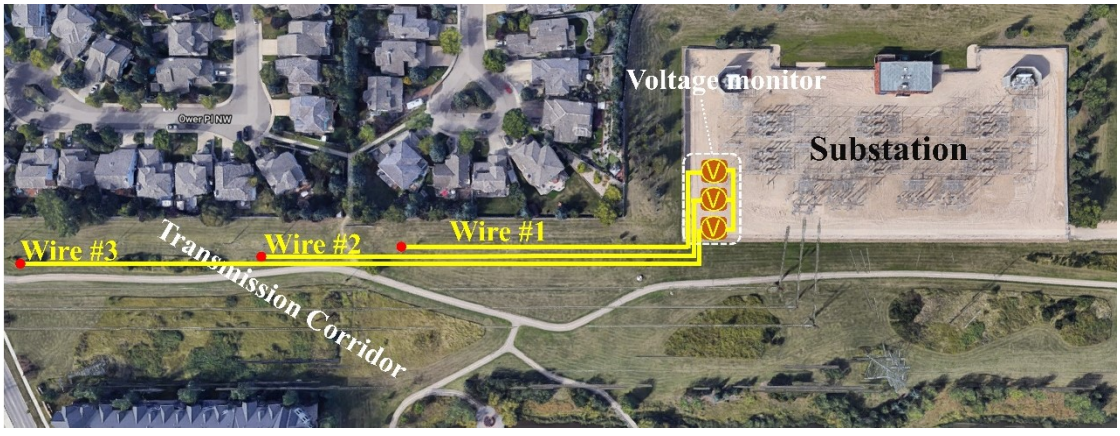

Figure 3.4 Illustration of the implementation in a transmission line corridor

- Implementation in a distribution feeder

The implementation of the multiwire technique in feeders is illustrated using an actual case shown in Figure 3.5(a). The measuring wires are suspended overhead on the poles parallel to the phase and neutral conductors. There are many poles to hold conductors in a feeder. The multi-grounded neutral is not grounded at each pole but at least every three to four poles to achieve a required span length, such as 150m. Thus, the poles without a neutral grounding rod are useful to ground the measuring wires. Considering that the neutral span length may vary between 50m and 400m in practice for various feeders, it is possible to ground the three measuring wires within the first neutral span in some feeders. This practice is the implementation Scenario 1, as illustrated in Figure 3.5(b). For example, the first neutral span is long enough, such as 150m~400m, and the three measuring wires are in lengths of 50m, 75m, and 100m, respectively.

Research has been conducted to determine the usefulness of implementation Scenario 2, which is shown in Figure 3.5(b). This is a more general arrangement where the neutrals are grounded along the measuring wires. Such an implementation lowers the multiwire technique's performance on the inductive interference reduction due to neutral rods will drain currents and thus result in unequal currents among adjacent neutral spans above the measuring wires, which will cause unbalanced EMF inductions on the measuring wires. Study results reported in Appendix B indicate that the errors introduced in this arrangement seem to be high.

Additionally, the multiwire technique can also be implemented in feeders with no neutral or a single-point grounded neutral. This practice is equivalent to implementation Scenario 1.

(a) Bird's eye view

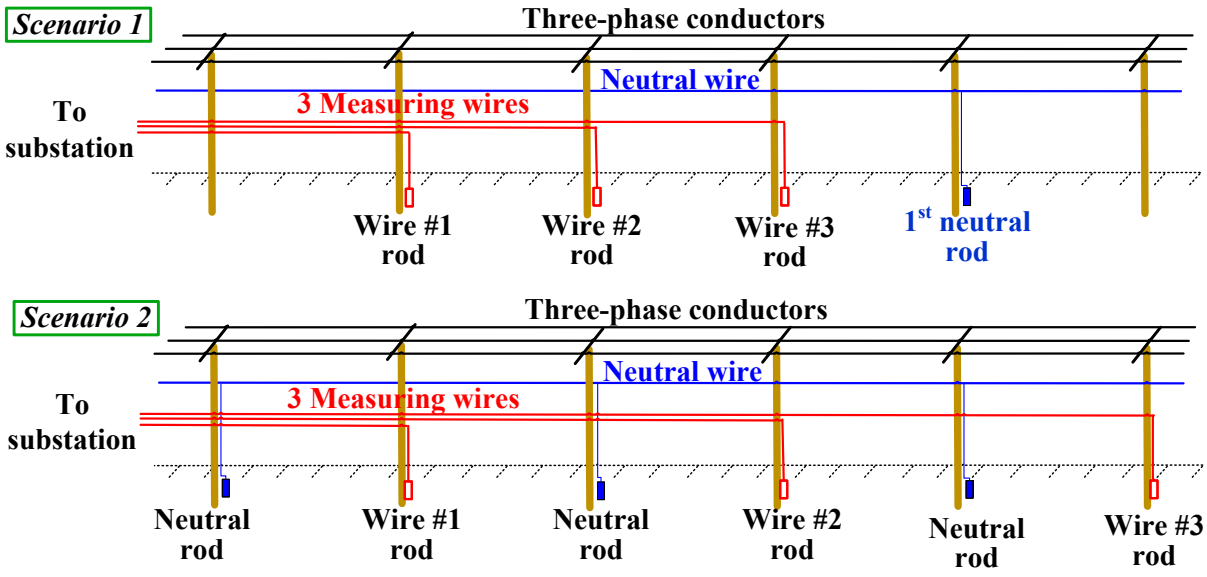

(b) Horizontal view

Figure 3.5 Illustration of the implementation in a distribution feeder

In summary, the proposed multiwire technique can be easily and permanently implemented in a transmission line corridor or on a distribution feeder. Moreover, due to the advantage of inductive interference reduction, the multiwire technique has enabled us to extend the online monitoring method to substations with all types of power transformers, including Y_g-Y_g or Y_g-Y_g-Δ (delta tertiary winding) connected transformers.

3.2.2 Extending the Multiwire Technique to Reduce Soil Potential Inference

Another problem encountered with the GPR measurement is the soil potential inference, as shown in Figure 3.6. Since the measuring wire is short, the grounding rod of each measuring wire experiences a transfer voltage from the substation grounding grid in the soil. In other words, soil potentials at the grounding locations of all the measuring wires are not zero. This phenomenon renders the GPR measurement using one measuring wire less accurate. It turns out that the proposed multiwire technique can also reduce the effect of such soil potential interference, thus resulting in a general method for GPR measurement.

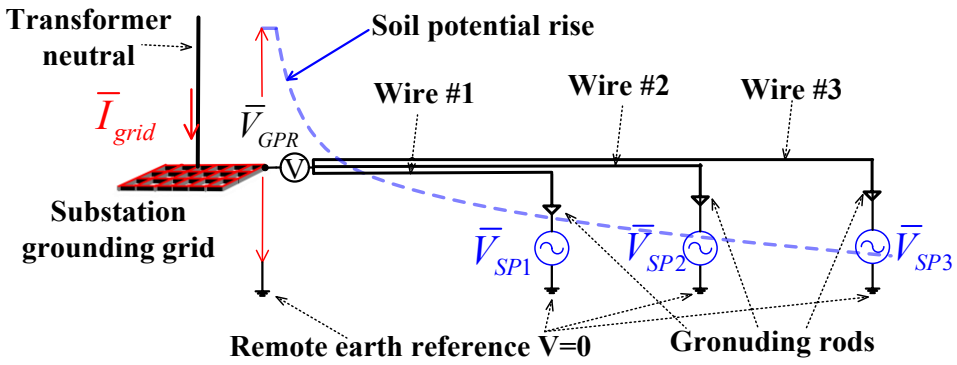

Figure 3.6 Soil potential rise at the grounding locations of the measuring wires

The extension of the multiwire technique for soil potential interference reduction is explained in the following. The profile of the soil potential rise in the surrounding area of a substation is in proportion to the GPR of the grounding grid, and it can be expressed as follows:

$$\bar{V}_{soil}(d) = f(d)\bar{V}_{GPR} \tag{3.3}$$

where $\bar{V}_{soil}(d)$ is the soil potential at a distance d from the edge of the grounding grid, shown as the dotted blue curve in Figure 3.6. $f(d)$ is a function of the structure of the grounding grid, the soil condition, and other structural factors. For the proposed method, we assume that $f(d)$ can be pre-determined using one of the following two approaches:

- The first approach is to simulate the grounding grid using electric-field simulation software such as CDEGS. The simulation result is the GPR profile function $f(d)$. One example is shown in Figure 2.18 in Chapter 2. This approach is used in the proposed method in this Chapter.

- A simpler but less accurate approach approximates the grounding grid as a hemispherical electrode [22]. It can be shown that $f(d)$ can be estimated as $1/\pi S_{grid}(2d + D_{grid})$. According to industry experience, this approach may obtain reasonable accuracy when $d > (1.5\sim2)D_{grid}$, where D_{grid} represents the diameter of the grounding grid [22, 23, 46].

With a pre-determined GPR profile function $f(d)$, the following relationship can be established at the location d_i of the grounding electrode in the ith measuring wire.

$$\bar{V}_{SPi} = p_i \bar{V}_{GPR} \tag{3.4}$$

Where $\bar{V}_{SPi}$ is the soil potential at the grounding electrode of ith measuring wire, and $p_i = f(d_i)$. It is clear that $p_i = 1$ at the edge of the substation since $\bar{V}_{soil} = \bar{V}_{GPR}$ at this location. Accordingly, one can have the following relationship for the ith measuring wire when considering the existence of both inductive interference and soil potential interference:

$$\bar{V}_{Mi} = (1 - p_i)\bar{V}_{GPR} - L_i \bar{V}_{EMF} + \bar{e}_{ri} \tag{3.5}$$

In (3.5), the GPR $\bar{V}_{GPR}$ can be determined by using three or more measuring wires with the help of a least-square algorithm. Results shown later indicate that three wires provide the best trade-off between implementation complexity and GPR estimation accuracy. The corresponding equation to determine the GPR $\bar{V}_{GPR}$ is as follows:

$$\begin{bmatrix} \bar{V}_{GPR} \\ \bar{V}_{EMF} \end{bmatrix} = \left(\begin{bmatrix} 1-p_1 & -L_1 \\ 1-p_2 & -L_2 \\ 1-p_3 & -L_3 \end{bmatrix}' \begin{bmatrix} 1-p_1 & -L_1 \\ 1-p_2 & -L_2 \\ 1-p_3 & -L_3 \end{bmatrix} \right)^{-1} \begin{bmatrix} 1-p_1 & -L_1 \\ 1-p_2 & -L_2 \\ 1-p_3 & -L_3 \end{bmatrix}' \begin{bmatrix} \bar{V}_{M1} \\ \bar{V}_{M2} \\ \bar{V}_{M3} \end{bmatrix} \tag{3.6}$$

In summary, the proposed multiwire technique can overcome the interferences caused by induction and soil potential rise. Thus, the main problems faced by the GPR measurement have been solved. The proposed technique is useful for the online monitoring methods presented in this thesis, and it can also improve the offline methods for grounding grid impedance measurement.

3.2.3 Natural 3rd Harmonic Current as Test Signals

Another advantage of the multiwire GPR measurement technique is that it can measure small GPR signals since interferences from induction and soil potential are reduced significantly. Accordingly, it becomes feasible to use the zero sequence current during normal system operations, instead of during ground faults, as the test signals for substation grounding grid condition monitoring. There are two types of zero sequence currents: the power-frequency current and the 3rd harmonic current. The former is caused by unbalanced loads among three phases. The latter is due to numerous single-phase power electronic devices used in distribution systems. References [80-83] have

shown that the 3rd harmonic current produced by such single-phase devices is mainly in the zero sequence. The aggregate magnitude of such harmonics experienced at the substation can be even higher than that of the zero sequence current at power frequency. Therefore, the 3rd harmonic zero sequence current may be a more suitable candidate as a test signal.

Field measurements have been conducted to verify the above postulation. The GPR of a distribution substation shown in Figure 3.7 was measured. A power quality monitor is placed at the edge of the substation for GPR measurement. It connects the substation fence and a measuring wire of 75m. The measuring wire does not experience inducive interference since it is distanced from and perpendicular to the transmission lines.

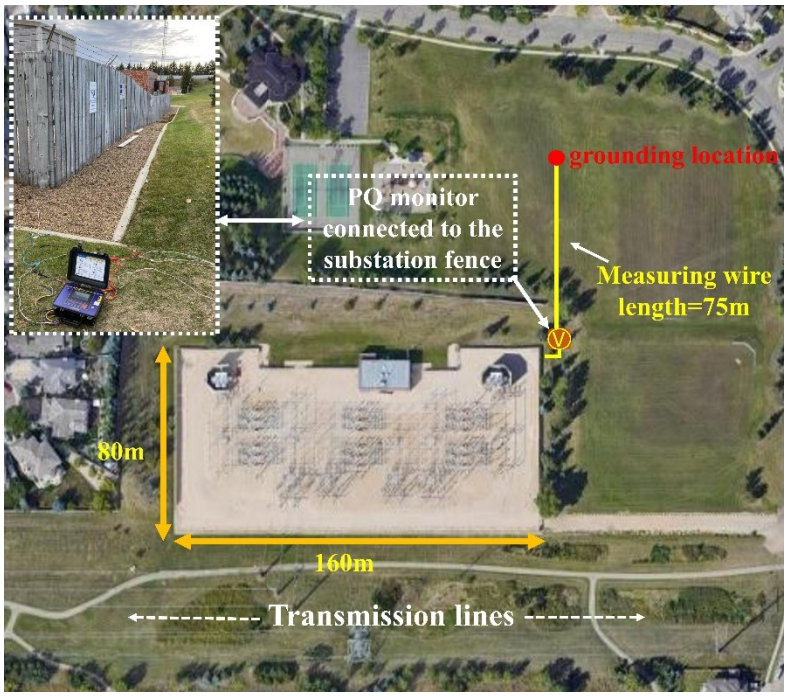

Figure 3.7 Description of the field experiments on substation GPR measurement

Figure 3.8 presents the measured GPR waveform and the spectrum derived from 3 seconds of waveforms. It demonstrates the existence of harmonic components in the substation GPR. The 180Hz GPR is higher than the 60Hz GPR for this substation. It is also worth noting that the 3rd harmonic GPR exists continuously, although its magnitude may vary over time. Such a 3rd harmonic GPR was also widely observed in many other field tests [24, 32, 33].

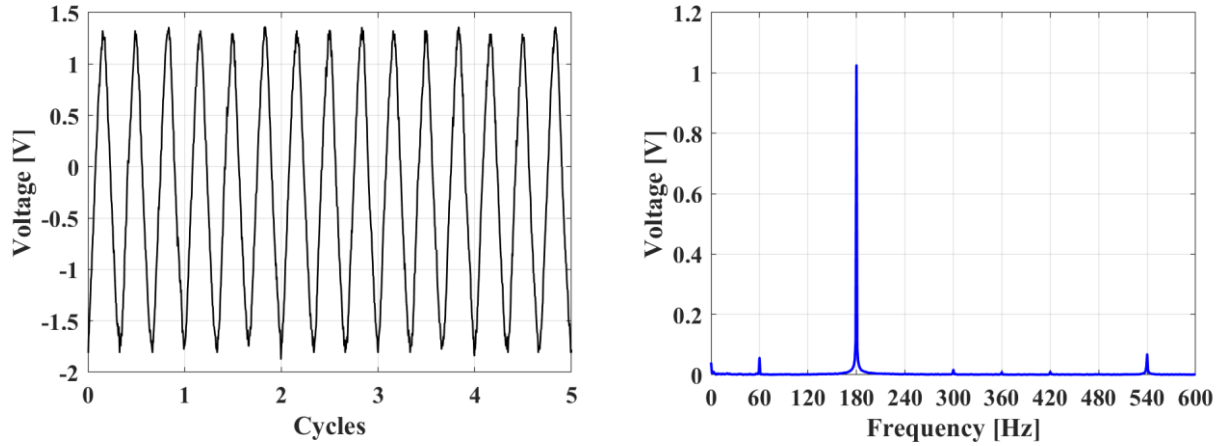

(a) Waveform (b) Harmonic spectrum

Figure 3.8 Results of the field experiments on substation GPR measurement

Therefore, using the natural 3rd harmonic current as a test signal is advantageous to estimate the substation grounding grid impedance. Estimation results are available continuously, at very short intervals, such as one result per several seconds. As a result, the conclusions drawn on the grounding grid conditions can be even more trustworthy and reliable than those derived from the fault-current-based method. Since grounding grid impedance is primarily resistive and the 3rd harmonic frequency is not significantly higher than 60Hz, the results calculated using 3rd harmonic data can be directly used to represent the power-frequency resistance of the grounding grid. Moreover, the calculated substation grounding grid impedances at the 3rd harmonics can be converted to the power frequency.

3.3 An Improved Online Monitoring Method

The proposed multiwire GPR measurement technique and the existence of the 3rd harmonic substation GPR verified in the previous section can be jointly used to provide an advanced solution to the online monitoring of substation grounding grid conditions. It is conceived as follows. (1) The natural 3rd harmonic current and the resultant 3rd harmonic GPR on the substation grounding grid exist continuously. They can be used to estimate the grounding grid impedance at power frequency at short time intervals, thus fast-tracking the conditions of the substation grounding grid. (2) The 3rd harmonic GPR can be estimated with acceptable accuracy using the multiwire technique with the advantages of significantly reducing inductive interference and soil potential interference.

Subsequently, an improved method for online monitoring of substation grounding grid conditions using natural 3rd harmonic currents is developed.

3.3.1 Setup of the Improved Method

The schematic diagram of the setup of the proposed improved method is shown in Figure 3.9. The implementation of the multiwire technique has been described in section 3.2.2. It can be within a transmission line corridor or integrated into a distribution feeder. It is noted that the exact locations of the measuring wires are not explicitly shown in the figure. The minimum length of the measuring wires is suggested to be no less than 40m for the purposes of accurate p-values determination. This is because the GPS resolution is about 1m, and because of the sharply decreasing nature of the soil potential rise near the substation, the typical curves of which can be seen in Figure 3.6 and Figure 3.12. A current monitor is placed at the transformer neutral, transmission shield wire terminals, and the clumped conductor of feeder neutrals in the substation, respectively. For the substations with feeder neutrals not clumped into one conductor, the current on each neutral can be individually measured using one current monitor. The current and voltage monitors are synchronized using precision time signals from the substation clock. The substation Ethernet is used to transmit all measurement data to a processing unit, which is installed in the substation. The processing unit synchronizes and processes the measurement data based on the algorithm presented next. It also reports the monitoring results.

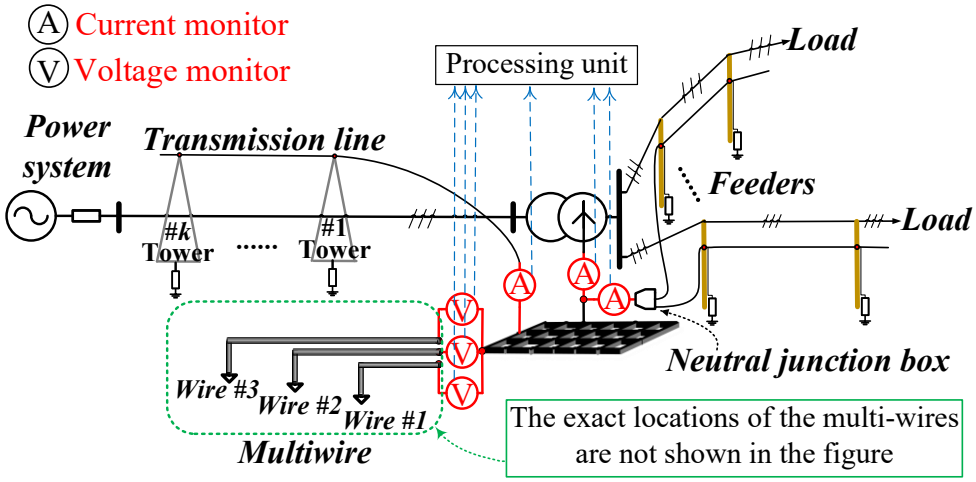

Figure 3.9 Schematic diagram of the setup of the proposed improved online monitoring method

3.3.2 Algorithm of the Improved Method

When a 3rd harmonic current $\bar{I}_{grid}^{3rd}$ flows through the substation grounding grid shown in Figure 3.9, the generated 3rd harmonic substation GPR $\bar{V}_{GPR}^{3rd}$ can be estimated using (3.6). Thus, the substation grounding grid impedance at the 3rd harmonics Z_{grid}^{3rd} can be determined as follows:

$$Z_{grid}^{3rd} = \frac{\bar{V}_{GPR}^{3rd}}{\bar{I}_{grid}^{3rd}} = \frac{\bar{V}_{GPR}^{3rd}}{\bar{I}_{Trn}^{3rd} - \bar{I}_{N}^{3rd} - \bar{I}_{SW}^{3rd}} \tag{3.7}$$

where $\bar{I}_{Trn}^{3rd}$ is the transformer neutral current at the 3rd harmonics, $\bar{I}_{N}^{3rd}$ is the feeder neutral current at the 3rd harmonics, and $\bar{I}_{SW}^{3rd}$ is the summation of all the transmission shield wire currents at the 3rd harmonics.

Subsequently, the substation grounding grid impedance at power frequency Z_{grid} is calculated as:

$$Z_{grid} = \mathrm{Real}\left\{Z_{grid}^{3rd}\right\} + j\,\mathrm{Imag}\left\{Z_{grid}^{3rd}\right\}\Big/3 \tag{3.8}$$

where $\mathrm{Real}\{\cdot\}$ and $\mathrm{Imag}\{\cdot\}$ represent the real part and the imaginary part of a complex number, respectively.

It is worthwhile noting that the grounding grid impedance calculated in (3.8) can directly reflect the conditions of the substation grounding grid since the effects of all the interconnected shield wires and neutrals are excluded. The use of the term "impedance" implies the proposed method can provide the total impedance rather than only the resistance component, although substation grounding grid impedances at the first several harmonics are primarily resistive [84, 85]. The impedance information may be more valuable for some sizeable power facilities at low soil resistivities, where the reactance is not negligible compared to the resistance.

An index of error ε is defined to quantify the accuracy of the grounding grid impedance estimation. It also facilitates the analysis and presentation of the proposed method.

$$\varepsilon = \left| \frac{Z_{grid} - Z_{grid\_true}}{Z_{grid\_true}} \right| \tag{3.9}$$

where Z_{grid_true} is the true value of the substation grounding grid impedance at power frequency.

The procedure of the proposed online monitoring method is shown in the flowchart of Figure 3.10. The explanation and discussion follow.

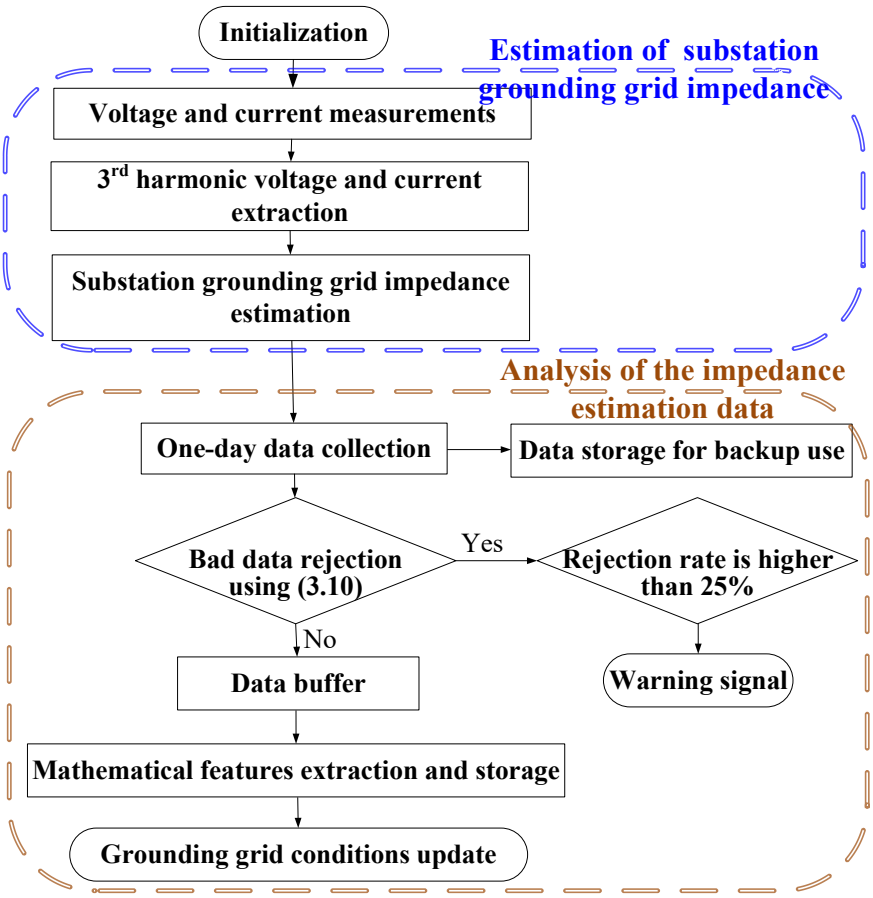

Figure 3.10 Procedure flowchart of the improved online monitoring method

One grounding grid impedance can be estimated based on the synchronized voltage and current waveform measurements in snapshots per a consecutive time span. A one-minute time span is suggested, which is sufficient for this long-term monitoring task. A shorter time span is also useful at the cost of more demands and requirements on infrastructure, such as data communication and storage. It is noted that gapless data recording and real-time streaming of data are not necessary.

In other words, the synchronized waveform data measurement and processing can be easily done within the substation. Estimated impedances are stored in the time sequence for the subsequent statistical analysis.

Each estimated impedance is preliminarily verified based on the primarily resistive feature of the substation grounding grid impedance. An estimation is rejected and discarded if the criterion in (3.10) is satisfied, i.e., the resistance is negative or too small compared to the reactance. If there is a high rate of data rejection in one day, which can be set at 25%, a warning signal will be sent, and a subsequent investigation into the monitoring system will be applied.

$$\text{Real}\left\{Z_{grid}\right\} < 0 \quad or \quad \left|\frac{\text{Real}\left\{Z_{grid}\right\}}{\text{Imag}\left\{Z_{grid}\right\}}\right| < n_z \tag{3.10}$$

where n_z is a user-defined coefficient, adjustable for different substation grounding grids. It can be generally determined as 1 for regular substations.

To further reduce the influence of measurement and background noise on each single estimation result when 3rd harmonic quantities may be in low values for some situations, the statistical mean value $\tilde{Z}_{grid}$ of all the qualified estimation data in one day is determined as follows:

$$\tilde{Z}_{grid} = \frac{1}{N}\sum_{k=1}^{N} Z_{grid}[k] \tag{3.11}$$

where $Z_{grid}[k]$ is the estimated grounding grid impedance for the kth minute in one day. N is the number of qualified data after the bad data rejection operation. It can be up to 1440 when one impedance estimation is generated every minute.

The statistical mean value is an index to be continuously tracked to reveal the substation grounding grid conditions. The additional advantage of this statistical process is to avoid unnecessary storage and computation burdens, especially when the estimation data accumulates overwhelmingly during long-term monitoring. Other mathematical features, such as the lower and upper bounds of the 95% confidence interval, can also be extracted to provide additional confidence in the results.

3.4 Case Studies and Sensitivity Studies

Preliminary case studies and sensitivity studies are carried out through extensive simulation studies. The goals are (1) to test the performance of the proposed method in the aspect of the measurement of substation grounding grid impedance; and (2) to check the possible impacting factors and their influence. The findings can help to implement the proposed method better. This section presents some of the representative results and corresponding discussions.

3.4.1 Description of the Test System

A simple test system is built in the "Multiphase Harmonic Power Flow (MHPF)" software combined with CDEGS software simulations. All the inductive and soil potential interferences are considered and included in the simulations. The test system is based on industry data. It consists of a Thevenin equivalent supply system, a transmission line, a power transformer, a substation grounding grid, a distribution feeder, and a three-phase load functioning as a 3rd harmonic source, as shown in Figure 3.11(a). The power frequency of this test system is 60Hz.

The three-phase and single-phase fault levels for the 144kV supply system are 20kA with an X/R ratio of 30 and 16kA with an X/R ratio of 40, respectively. The substation transformer is Y_g-Y_g connected with a buried delta tertiary winding. The capacity is 25MVA, and the voltage ratio is 144kV/25kV/13.8kV. The equivalent leakage reactance is 11%, -0.5%, and 7% for the primary, secondary, and tertiary winding, respectively [86]. The transformer neutral is connected to the substation grounding grid, which is presented in Figure 3.11(b). The transmission line is 20km with a span length of 400m and a 12-foot-¾-inch grounding rod at each tower foot. The feeder has a total length of 1.5km, a span length of 100m, and a 12-foot-¾-inch grounding rod at the pole. The physical structures of the power lines are shown in Figure 3.11(c). The soil resistivity is 100Ωm. Thus, grounding resistances of the transmission line and the feeder are determined as R_{TL} =15.0Ω and R_{DL} =27.9Ω, respectively. The routes of transmission line and feeder are shown in Figure 3.11(b). The three-phase load is in a capacity of 17MVA (i.e., load current I_{load} is 392A). Its 3rd harmonic current spectrum is $I_0^{3rd} = 6\%I_{load}$, $I_1^{3rd} = 1\%I_{load}$, and $I_2^{3rd} = 1\%I_{load}$ for the zero, positive and negative sequence, respectively. This harmonic spectrum is from field data statistics in Alberta [81]. The grounding resistance at the load location R_C is assumed as 10Ω.

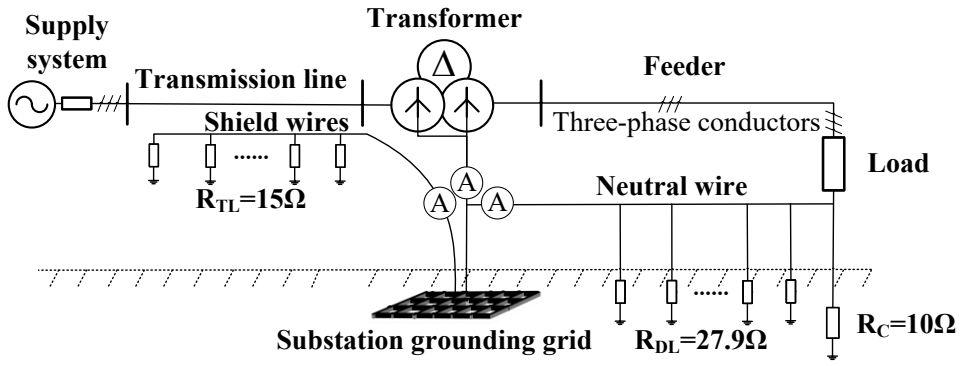

(a) Schematic diagram

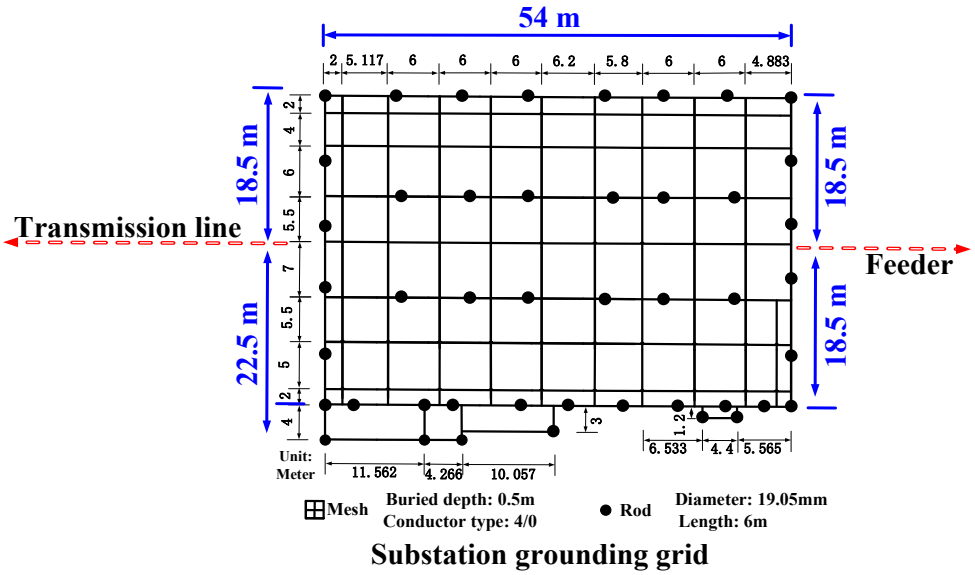

(b) Routes of transmission line and feeder with respect to substation grounding grid

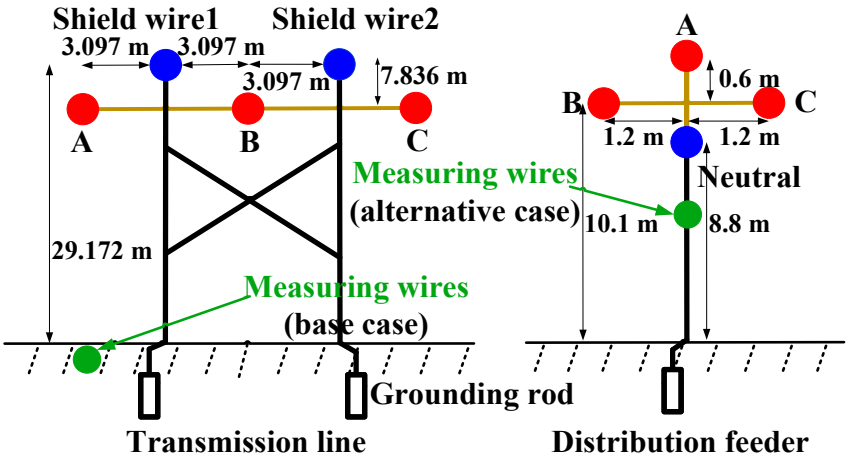

(c) Physical structures of the power lines and the illustration of the measuring wire location

Figure 3.11 A simple test system

The measuring wires in the lengths of 50m, 75m, and 100m are shallowly buried directly below the phase A conductor of the transmission line, as shown in Figure 3.11(c). A voltage monitor is installed at each wire terminal at the substation edge for 3rd harmonic GPR measurement. A current monitor is placed at the transformer neutral, transmission shield wire, and feeder neutral wire at their substation terminals, respectively, for 3rd harmonic current measurement.

The arrangement and equipment parameters described above are used as the base case for the case studies and sensitivity studies in the subsequent sections.

3.4.2 Case Studies

3.4.2.1 Base Case

With the input of the substation grounding grid, the true grounding grid impedance at 60Hz is determined as 0.8734+j0.0011Ω using CDEGS simulations. Also, by injecting a current into the grounding grid, the transfer voltage coefficients (i.e., p values) in the route of the measuring wires are obtained from CDEGS simulations. They are presented in Figure 3.12 and Table 3.1.

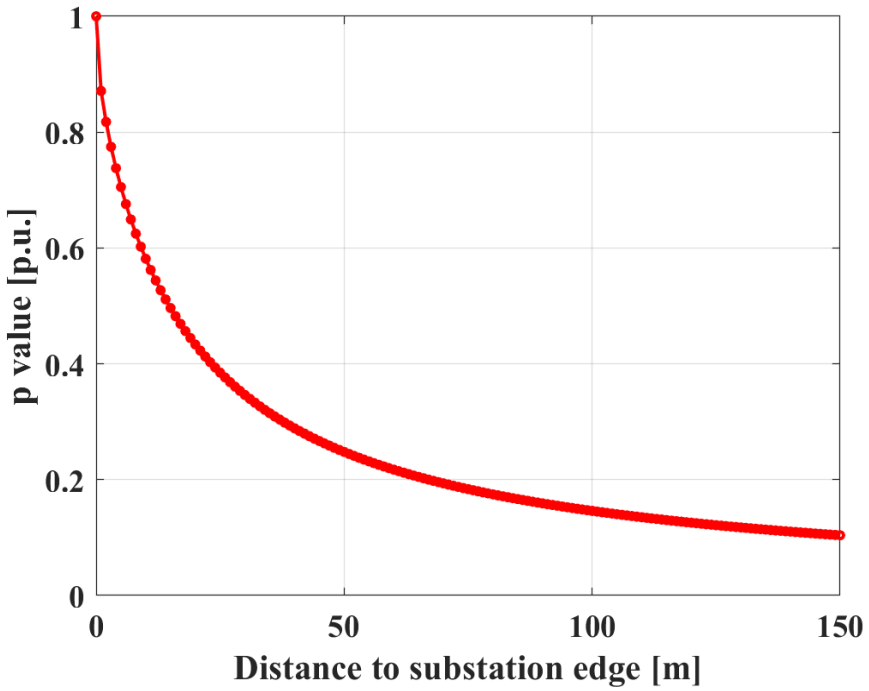

Figure 3.12 Transfer voltage coefficient in the route of the measuring wires

Table 3.1 Transfer voltage coefficient for some specific distances away from substation edge

Distance (m)	50	75	100	125	150
p (p.u.)	0.2479	0.1836	0.1461	0.1214	0.1039

The 3rd harmonic GPR measurements of the measuring wires in lengths of 50m, 75m, and 100m are -11.80+j7.73V, -12.81+j8.39V, and -13.38+j8.78V, respectively. The 3rd harmonic current measurements at the transformer neutral, feeder neutral, and shield wires are $\bar{I}_{Trn}^{3rd}$ = -29.34+j53.65A, $\bar{I}_{N}^{3rd}$ = -12.34+j44.96A, and $\bar{I}_{SW}^{3rd}$ = 0.83-j3.32A, respectively. Thus, the 3rd harmonic GPR $\bar{V}_{GPR}^{3rd}$ and current $\bar{I}_{grid}^{3rd}$ are determined as -15.72+j10.27V and -17.88+j12.01A. The substation grounding grid impedance at 60Hz is determined as 0.8716+j0.0036Ω. The error is 0.3473% in comparison to the true value of 0.8734+j0.0011Ω. The error may be majorly due to the end effect of induction [72, 87] (i.e., due to the measuring wires not being of infinite lengths), and minorly due to the effect of the nearby tower/pole footings.

3.4.2.2 Cases of Different Types of Substation Transformers

The substation transformer used in the base case is a three-winding transformer connected in Y_g-Y_g-Δ. This type of substation transformer is widely used in Alberta. Other winding connections such as Δ-Y_g and Y_g-Y_g may also be used for some substation transformers. Table 3.2 summarizes the performances of the proposed method for substation transformers in different winding connections. All two-winding transformers have a short-circuit reactance of 8%, a voltage ratio of 144kV/25kV, and a capacity of 25MVA in this study.

Table 3.2 Results for substation transformers in different winding connections

	$\bar{I}_{DLine}^{3rd}$ (A)	$\bar{I}_{N}^{3rd}$ (A)	$\bar{I}_{Trn}^{3rd}$ (A)	$\bar{I}_{TLine}^{3rd}$ (A)	$\bar{I}_{SW}^{3rd}$ (A)	$\bar{I}_{GRID}^{3rd}$ (A)	Error ε
Base Case	71∠-63°	46∠105°	61∠119°	3∠-61°	3.4∠-75°	21∠146°	0.35%
Y_g-Y_g	71∠-61°	45∠107°	60∠123°	12∠-62°	2.5∠-166°	18∠156°	0.82%
Y-Y_g	39∠27°	39∠117°	30∠148°	0∠-118°	4.9∠30°	24∠-121°	0.40%
Δ-Y_g	40∠32°	27∠-160°	35∠-147°	0∠32°	2.6∠29°	13∠-121°	0.29%

Table 3.2 shows that the errors are negligible for all types of substation transformers, even though the resultant 3rd harmonic current on the transmission line is significant in some cases. This is because the measuring wires can significantly reduce the induced EMFs. For the worst case of the Y_g-Y_g connected transformer, the substation grounding grid impedance at 60Hz is estimated as 0.8827+j0.0050Ω. The error is 0.82%. Therefore, one can conclude that the proposed method is applicable for substations consisting of power transformers of all types of winding connections.

3.4.2.3 Cases of Different Sizes of Substation Grounding Grids

Various substation grounding grids in different sizes are used to test the performance of the proposed method. In this study, each grounding grid is composed of 10m×10m meshes. Simulation results presented in Table 3.3 show that the estimated impedance is close to the true value for each grounding grid in different sizes. The maximum error in all the cases is less than 1%.

Table 3.3 Results for different sizes of substation grounding grids

Size of Grid	p_1	p_2	p_3	Estimated Impedance (Ω)	True Impedance (Ω)	Error ε
Base Case	0.2479	0.1836	0.1461	0.8716+j0.0036	0.8734+j0.0011	0.35%
100m×100m	0.3570	0.2813	0.2323	0.4694+j0.0042	0.4673+j0.0025	0.57%
200m×200m	0.5044	0.4253	0.3680	0.2280+j0.0035	0.2265+j0.0026	0.75%
300m×300m	0.5821	0.5087	0.4526	0.1507+j0.0034	0.1495+j0.0028	0.89%

3.4.2.4 Cases of Different Horizontal Displacements of the Multiwire in the Transmission Corridor

The three measuring wires are packed together to share one route along the power line. This route can be horizontally different. Figure 3.13 presents the simulation results for different horizontal displacements of the measuring wires with respect to the phase conductors and the shield wires of the transmission line. Figure 3.13 reveals that the errors change only slightly for all the possible horizontal displacements of measuring wires, even though the 3rd harmonic currents on three phases are very unbalanced in this case. Therefore, one can conclude that the horizontal

displacement of the multiwire in the transmission line corridor has negligible influence on the method.

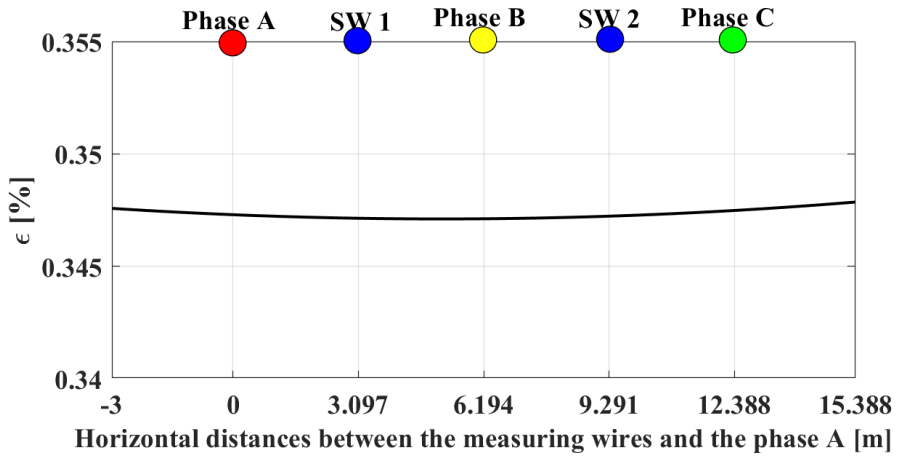

Figure 3.13 Errors for different horizontal displacements of measuring wires in the transmission corridor

3.4.2.5 Cases of Different Lengths of the Multiwire

Results for different lengths of measuring wires are presented in Table 3.4, which shows that the length of measuring wires has little impact on estimation accuracy.

Table 3.4 Results for different lengths of measuring wires

Cases	Wire #1 (m)	Wire #2 (m)	Wire #3 (m)	Estimated Impedance (Ω)	Error ε
Base Case	50	75	100	0.8716+j0.0036	0.3473%
1	50	75	125	0.8724+j 0.0039	0.3400%
2	50	75	150	0.8731+j 0.0042	0.3545%
3	50	100	125	0.8721+j 0.0038	0.3396%
4	50	100	150	0.8730+j 0.0041	0.3508%
5	75	100	125	0.8735+j 0.0044	0.3729%
6	75	100	150	0.8743+j 0.0047	0.4261%
7	75	125	150	0.8741+j 0.0046	0.4064%
8	100	125	150	0.8753+j 0.0051	0.5115%

3.4.2.6 Cases of the Implementation of the Multiwire in Feeders

When implementing the multiwire technique in the feeder in this test system, the neutral's first grounding rod is removed to facilitate the implementation. As shown in Figure 3.11(c), the three measuring wires are suspended on the feeder poles at the height of 7m and in lengths of 50m, 75m, and 100m, respectively. In this arrangement, the transfer voltage coefficients are determined as p_1=0.2480, p_2=0.1463, and p_3=0.1040. The 3rd harmonic voltage measurements are determined as $\bar{V}_{m1}^{3rd}$=-11.43+j8.58V, $\bar{V}_{m2}^{3rd}$=-12.40+j10.47V, and $\bar{V}_{m3}^{3rd}$=-12.39+j11.78V, respectively. Thus, the 3rd harmonic GPR is estimated as $\bar{V}_{GPR}^{3rd}$=-16.10+j10.25V. With the 3rd harmonic current determined as $\bar{I}_{grid}^{3rd}$=-18.13+j12.11A, the substation grounding grid impedance at 60Hz is estimated as Z_{grid} =0.8753+j0.0064Ω. The error is 0.65%.

Results for different heights of the measuring wires are shown in Figure 3.14. It can be seen from Figure 3.14 that the impedance estimation errors vary in a small range of 0.12% for all the possible heights of measuring wires in this feeder. Therefore, one can conclude that the vertical displacement of the multiwire on the feeder has little influence on the proposed method.

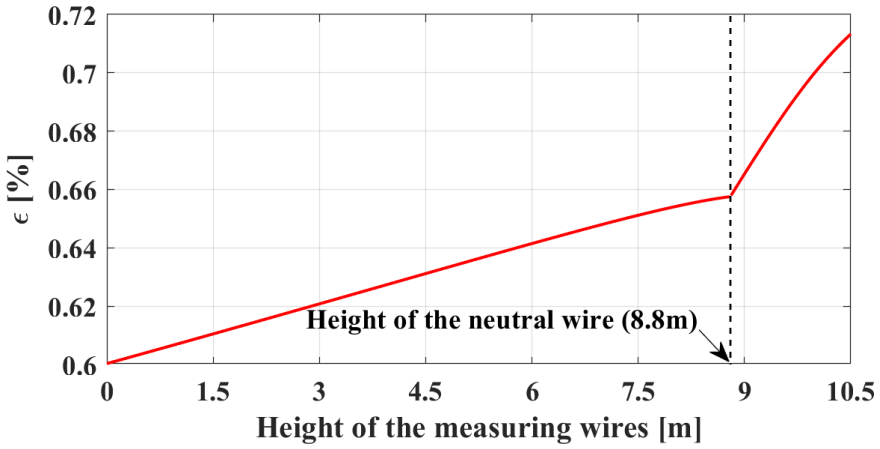

Figure 3.14 Errors for different heights of measuring wires installed in the feeder pole

3.4.3 Sensitivity Studies

In this section, the results of sensitivity studies are presented to study the influence of the uncontrollable impacting factors for the proposed method.

3.4.3.1 Influence of 3rd Harmonic-Generating Load Locations and Power Line Parameters

The feeder carries the load-generating 3rd harmonic currents into the substation grounding grid. The load can be at different locations, which is represented by the length of the feeder in this study. Also, the distribution of the 3rd harmonic current returning through the neutral can be different for the neutral parameters: total length, span length, and grounding resistance. Moreover, the induced EMFs from the feeder current may not be entirely linear for the length of the measuring wires (which are set in the transmission line corridor in this case) due to the possible separation angle and the end effects of induction. Thus, the influence of different feeder parameters is studied and presented in Figure 3.15 and Figure 3.16.

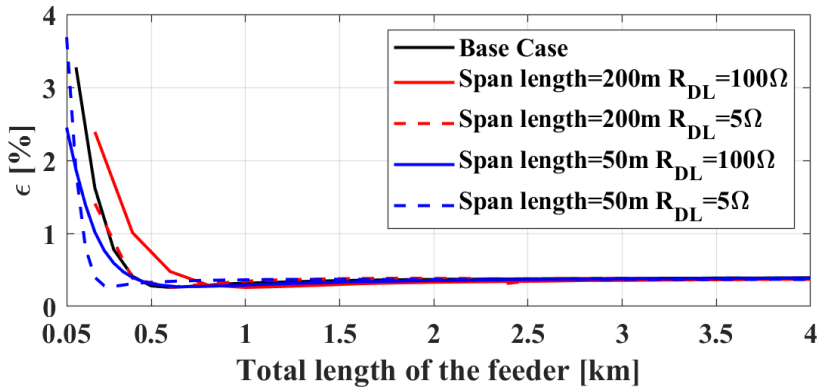

Figure 3.15 Errors for different total lengths, span lengths, and grounding resistances of the feeder

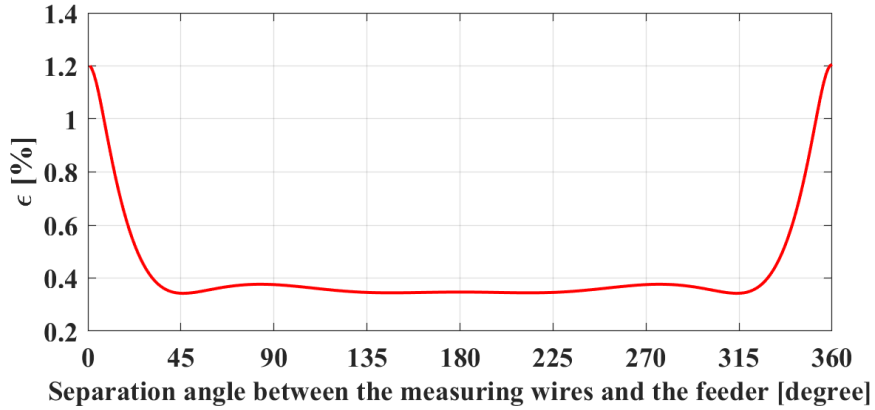

Figure 3.16 Errors for the different separation angles between the wires and the feeder

It can be concluded from Figure 3.15 that all the practical total lengths, span lengths, and grounding resistances of the feeder do not affect the proposed method significantly. The errors stay low for

different feeders. This is especially true considering that the load is not usually at one or two spans away from the substation in practice. Furthermore, Figure 3.16 shows that, due to the method's advantage of inductive interference reduction, the separation angle between the feeder and the measuring wires imposes little influence on the accuracy of impedance estimation, even though there is a large 3rd harmonic current in the feeder. In summary, the proposed method imposes no requirement on the location of the 3rd harmonic source in power systems.

Additionally, since the measuring wires run parallel to the transmission line, they can always significantly reduce the 3rd harmonic EMF induction from the currents on the transmission line regardless of its physical structures.

3.4.3.2 Influence of Grounding Resistance at the Load

The grounding resistance at the load R_C is contributed by the load's local grounding electrodes and the interconnected downstream grounding electrodes. It may vary substantially in different situations. Figure 3.17 reveals that the errors differ slightly when the resistance R_C continuously changes from 0.1Ω to 50Ω. Therefore, one can conclude that the grounding resistance at the load (i.e., the 3rd harmonic source) has almost no impact on the proposed method.

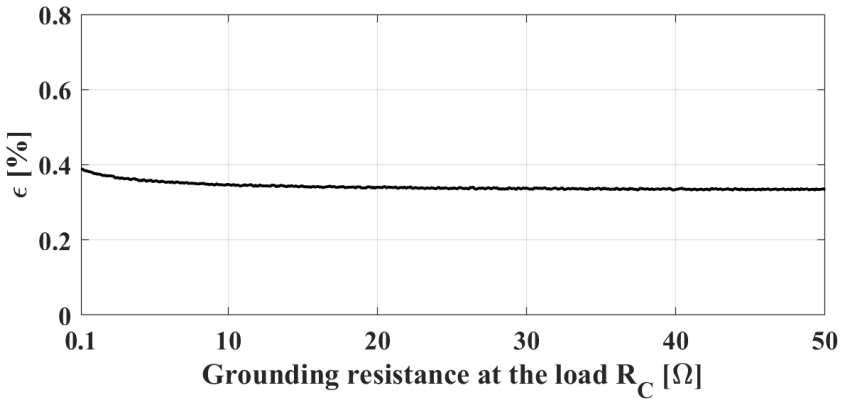

Figure 3.17 Error for different grounding resistances at the load

3.4.3.3 Influence of 3rd Harmonic Currents

The 3rd harmonic current on each phase can be in a different spectrum and time-variant for various loads. The influence of 3rd harmonic current variation is tested using 100,000 cases generated from

Monte Carlo Simulations. In each case, a 3rd harmonic load current on one phase is randomly selected from a lognormal distribution with a median value of $2\%I_{load}$ and 95% of the value below $10\%I_{load}$. The simulation results are presented in Figure 3.18.

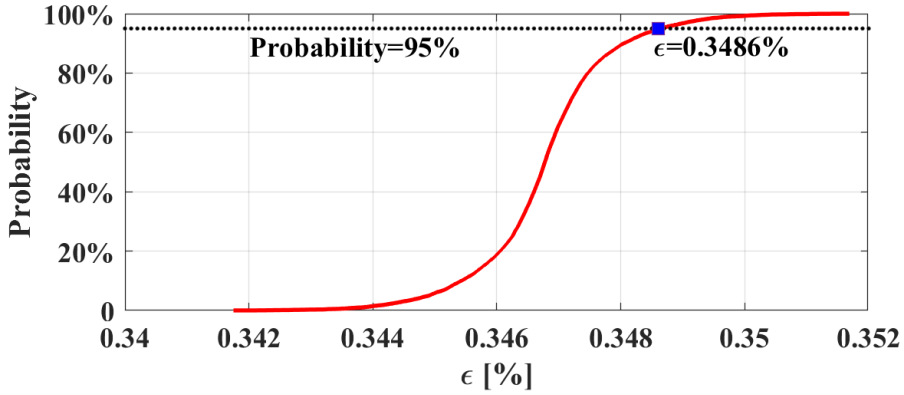

Figure 3.18 Results for different load-generating 3rd harmonic currents

Figure 3.18 demonstrates that all the impedance estimation errors are within a small range between 0.340% and 0.352%, although the 3rd harmonic current varies considerably. Therefore, one can conclude that the variation of the load-injecting 3rd harmonic current has a negligible influence on the proposed method.

3.4.4 Summary

Extensive case studies and sensitivity studies imply that the proposed method can use the naturally existing 3rd harmonic current to estimate the substation grounding grid impedance at 60Hz with reasonable accuracy. The proposed method is applicable for transmission and distribution substations, consisting of grounding grids of different sizes and substation transformers with all the possible types of winding connections, including Y_g-Y_g or Y_g-Y_g-Δ (delta tertiary winding). The horizontal displacement in the transmission line corridor and the vertical displacement in the feeder of the measuring wires have little influence on the proposed method. Moreover, the proposed method has no specific requirements for transmission lines, feeders, and downstream 3rd harmonic sources such as three-phase current spectra, locations, and grounding resistances.

3.5 Application Studies

In this section, preliminary application studies are presented to show the overall monitoring performance of the proposed method using a realistic study case. The results prove the effectiveness of the proposed method.

3.5.1 Description of the Study Case

The study case is shown in Figure 3.19. A power system supplies a 25MVA transformer connected in Y_g-Y_g-Δ (buried delta tertiary winding) through a transmission line. Labelled as Feeder 1~4, four 25kV feeders are positioned at angles of 90°, 135°, 180°, and 270° clockwise to the transmission line, respectively. A 5MVA three-phase load connected in Y_g is located at the end of each feeder with a 5Ω grounding resistance. The power factor is 0.95, lagging. The 3rd harmonic spectrum of the load on Feeders 1~4 is 0.7%, 3%, 2.4%, and 0.4% of its load current, respectively. The use of constant loads may be sufficient in this study since the 3rd harmonic current variation has almost no impact on the method's estimation accuracy, as concluded in the previous section. If not listed in Figure 3.19, the equipment parameters are the same as those used in the base case in section 3.4.

Three measuring wires in lengths of 150m, 200m, and 250m, respectively, are implemented in the transmission line corridor, with necessary voltage and current monitors installed. Thus, the transfer voltage coefficients can be determined as $p_1 = 0.1039$, $p_2 = 0.0807$, and $p_3 = 0.0660$ from CDEGS simulations with the input of substation grounding grid geometry. The soil resistivity is assumed as 50Ωm. Assume that the substation grounding grid deteriorates during the three years of monitoring. The deterioration is simulated in CDEGS by adding a layer of steel rust on all grounding grid conductors. The resistivity of the iron oxide is assumed as 11kΩm. The thickness of the iron rust increases from 0 to 2.8cm. Thus, the substation grounding grid impedance at 60Hz changes incrementally from 0.43Ω to 2.05Ω in this monitoring period.

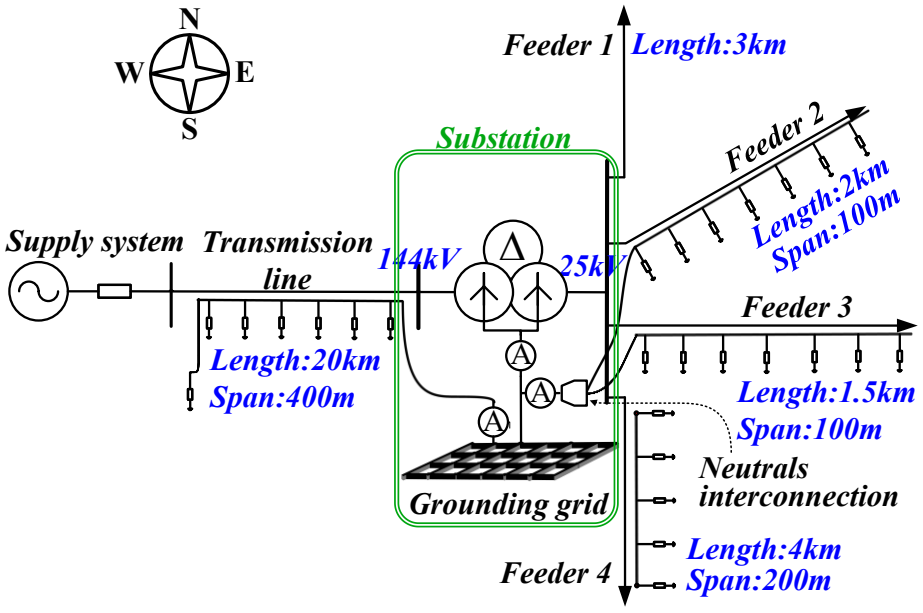

Figure 3.19 Description of the application study case

3.5.2 Online Monitoring Results

The results of a single test on the first day of monitoring, when the grounding grid is under normal conditions, are presented in the following. The 3rd harmonic currents and voltage measurements in phasors are $\bar{I}_{Trn}^{3rd}$=-7.38+j17.82A, $\bar{I}_{SW}^{3rd}$=-1.20+j0.13A, $\bar{I}_{N}^{3rd}$=-2.64+j12.07A, $\bar{V}_{m1}^{3rd}$=-2.21+2.24V, $\bar{V}_{m2}^{3rd}$=-2.18+j2.30V, and $\bar{V}_{m3}^{3rd}$=-2.12+j2.34V. As a result, the 3rd harmonic GPR is estimated as $\bar{V}_{GPR}^{3rd}$=-3.05+2.09V. Consequently, the substation grounding grid impedance at 60Hz is estimated as Z_{grid} =0.4363+j0.0791Ω. Compared to the true value of 0.4371+j0.0011Ω, the error is 2.59%.

To better mimic practical situations, random Gaussian noise is added in each waveform to generate a signal-to-noise ratio of 36dB. Figure 3.20 illustrates all the grounding grid impedance estimations on the first monitoring day. There are 1440 in total. Their mathematical features of interest are that the statistical mean value is 0.4458+j0.0069Ω and that the lower and upper bounds of the 95% confidence interval are 0.3060+j0.0155Ω, and 0.5871+j0.0066Ω, respectively. One can find that the estimated mean value is quite close to the true grounding grid impedance, with a difference of 0.01Ω.

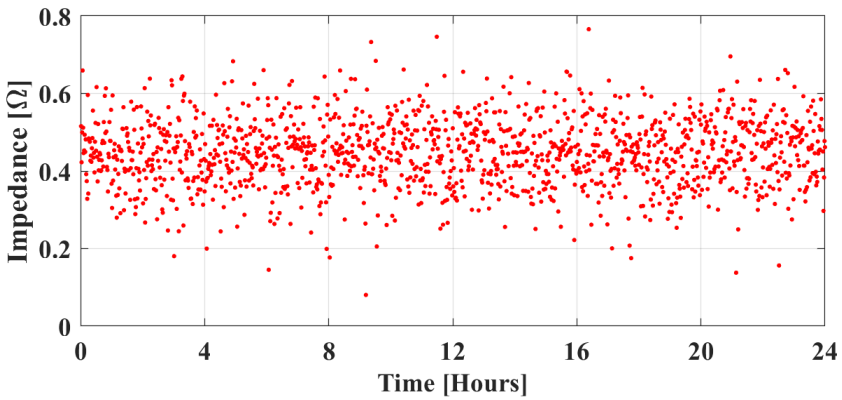

Figure 3.20 Grounding grid impedance estimations per minute with the influence of background noise in one-day monitoring

Figure 3.21 demonstrates that the statistical mean value of the impedance estimations per day can closely track the true grounding grid impedance at 60Hz throughout the monitoring period. Furthermore, the increasing trend of estimations reveals the grounding grid deterioration reliably and timely (i.e., the degradation can be conservatively found in the first year when the estimations increase to 1Ω in this case). The most significant difference between the estimation and the true impedance during the whole monitoring is 0.35Ω. This happens on the last monitoring day when the true grounding grid impedance is the largest, at 2.05Ω. The maximum error during the entire tracking time is 16.79%. Such an error is acceptable for online monitoring compared to the requirement of 25% for offline testing according to IEEE Standard 142-2007 [74]. Moreover, it is worth comparing that occasional measurements in this impedance range of less than 2.05Ω obtained from the offline methods, even if in full accuracy, cannot determine the gradual degradation of the grounding grid.

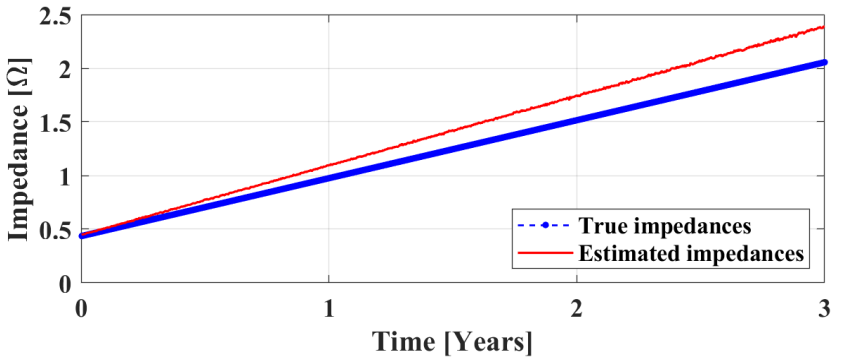

Figure 3.21 The results for the three years of monitoring on the grounding grid deterioration

3.6 Recommendation

Compared to the applicable limitations of the fault-current-based method as discussed in section 3.1, the improved method has almost no usage constraints. The method has been proved applicable for transmission and distribution substations containing grounding grids of different sizes and substation transformers with all the possible winding connections. Moreover, this method can estimate the grounding grid impedance at much shorter time intervals and thus provides more reliable conclusions on substation grounding grid conditions than the fault-current-based method. Hence, it is recommended to use the improved method for all the applications unless 3rd harmonic current and GPR are too low in some particular cases. The fault-current-based method is adopted for those cases if all the application requirements can be satisfied.

3.7 Conclusion

An improved method for substation grounding grid condition monitoring is proposed in this chapter. The proposed method uses a novel multiwire technique for substation GPR measurement. Using the naturally existing 3rd harmonic current as test signals and the resultant 3rd harmonic GPR, the method can estimate the substation grounding grid impedance at 60Hz at short time intervals and track the impedance estimations over time to reveal the substation grounding grid conditions. It is easy to implement the proposed method, with current measurements in the substation and the GPR measurement using the proposed multiwire technique permanently installed in a transmission line corridor or on a distribution feeder. Extensive case studies and sensitivity studies show that the proposed method performs well in estimating substation grounding grid impedances. The method is virtually unaffected by the GPR measuring wires' horizontal displacement in the transmission line corridor and vertical displacement on the feeder pole. Also, it has no specific requirements for transmission lines, feeders, and 3rd harmonic sources such as three-phase current spectra, locations, and grounding resistances. Due to the advantages of a significant reduction of inductive and soil potential interferences, the proposed method is applicable for transmission and distribution substations that contain grounding grids of different sizes and power transformers with all the possible winding connections. A realistic case is used for application studies to show that the proposed method can reliably and timely reveal the substation grounding grid conditions.

Chapter 4: Open Conductor Detection

The open conductor detection topic identified in Chapter 1 is a unique but important condition monitoring problem. The problem and its technical difficulties are analyzed, and two promising power-disturbance-based condition monitoring methods are proposed in this chapter.

4.1 Open Conductor Situation in Power Plants

Power plants are complex electrical systems. The stable output of power plants requires appropriate operations of each primary and auxiliary equipment, such as the generator step-up transformer (GSU) and cooling pumps. Figure 4.1 shows a typical electrical system of power plants. In the power plant electrical system, a standby auxiliary transformer (SAT) is installed to provide backup power from the power grid to each plant auxiliary segment and critical safety-related equipment when the plant is unable to provide its own power, such as upon startup or during accident scenarios. For example, when the main generator is tripped due to an emergency, the breaker "T" is switched off so that the auxiliary equipment such as cooling pumps will lose power. In this situation, the breakers "X", "Y" and "Z" are required to switch on immediately to provide the necessary backup power. Such a backup function must be reliable especially for nuclear power plants to avoid any possible failures related to reactors.

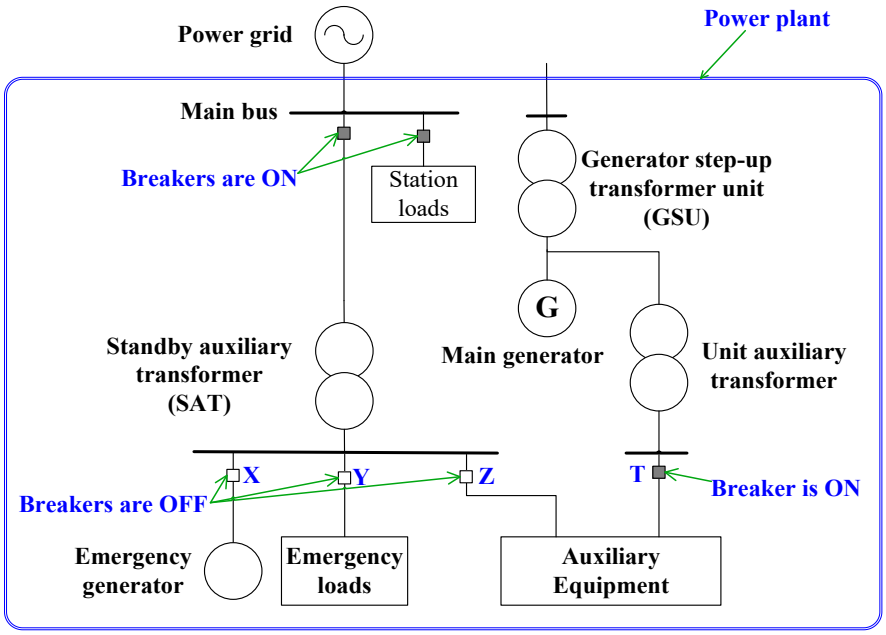

Figure 4.1 One-line diagram of power plant electrical system

However, the power supply to the plant's backup system may experience an open conductor situation, as described in Figure 4.2. Three-phase conductors feed the standby auxiliary transformer (i.e., SAT) that supplies the backup system in the power plants, i.e., the transformer is unloaded. The open conductor condition is a break in a single phase conductor. It can also occur due to equipment malfunction, such as breaker pole discordance. The open conductor point may exist anywhere between the main bus and the transformer terminal. If such an open conductor situation exists, the plant's auxiliary and emergency equipment may fail to provide the essential backup functions when required. In fact, such a situation is not uncommon. For example, the Byron nuclear power station in the United States and the Dungeness B nuclear power station in the United Kingdom ran into such situations in 2012 and 2014, respectively [56]. It is likely that the problem may also be encountered in other power plants or similar industrial facilities.

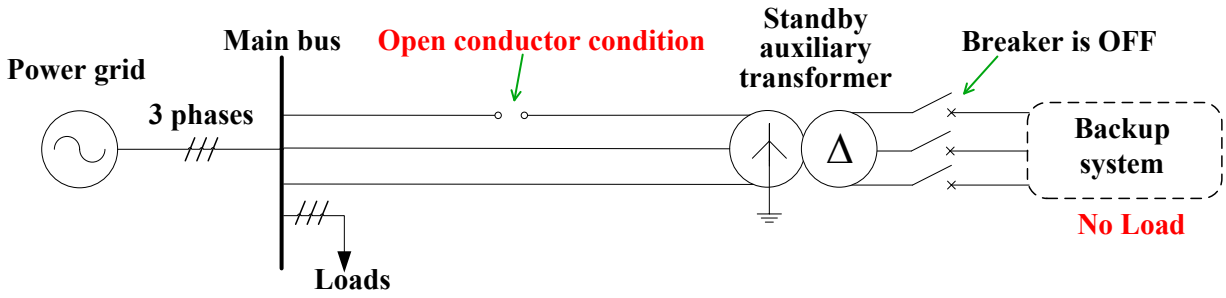

Figure 4.2 Open conductor problem description

Detecting this open conductor condition is difficult due to two special features [67]. First, the phase current on each conductor is almost zero since there is no load. As a result, one cannot use the conductor current to detect the open conductor condition. Second, the transformer has Y_g connected primary windings and Δ connected secondary windings or a three-legged core. As will be explained in detail in the following, such a transformer can recreate a "normal" voltage on the open phase through electrical or electromagnetic coupling from the two normal phases [62]. As a result, phase voltages at the transformer terminals cannot be used to detect the open conductor condition either. In summary, the open conductor condition produces no abnormal signatures in the phase current and voltage measurements under common power system conditions.

- Voltage recreation due to electrical coupling

For a transformer with Y_g connected primary windings and Δ connected secondary windings, the recreation of the voltage on the primary side opened phase is illustrated in Figure 4.3. Assume that the transformer is with a transformation ratio n_T and an arbitrary phase shift φ between the primary side and the secondary side (φ is usually zero). On the primary side, it is powered by a balanced three-phase source with the voltages expressed as $\bar{V}_{AN}$, $\bar{V}_{BN}$, and $\bar{V}_{CN}$, respectively. On the secondary side, the voltages across the windings, which correspond to the primary A, B, and C windings, are denoted as $\bar{V}_1$, $\bar{V}_2$, and $\bar{V}_3$, respectively. In this case in which phase A is under open conductor condition and phases B and C are energized, the secondary voltages $\bar{V}_2$ and $\bar{V}_3$ are induced. Due to the voltages circling Δ windings must be summed up to 0, the voltage $\bar{V}_1$ is created by $\bar{V}_2$ and $\bar{V}_3$. It induces the voltage $\bar{V}_{AR}$, on the opened phase A, equaling to $\bar{V}_{AN}$.

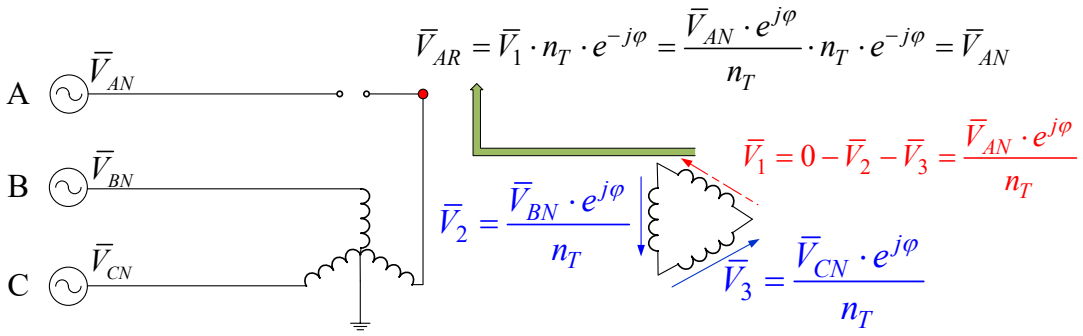

Figure 4.3 Voltage recreation due to electrical coupling

- Voltage recreation due to electromagnetic coupling

For a transformer with Y_g connected primary windings and a three-legged core, the recreation of the voltage on the primary side opened phase is illustrated in Figure 4.4. The primary winding has N turns. Assuming phase A is under an open conductor condition, the balanced excitations $\bar{V}_{AN}$, $\bar{V}_{BN}$, and $\bar{V}_{CN}$ produce the fluxes $\bar{\phi}_B$ and $\bar{\phi}_C$ in the core legs B and C, respectively. The voltage phase angle β is arbitrary. Since the summation of all the fluxes in the three-legged core must be equal to 0, the flux $\bar{\phi}_A$ is generated by $\bar{\phi}_B$ and $\bar{\phi}_C$. It induces voltage $\bar{V}_{AR}$ on the opened phase A, which equals to $\bar{V}_{AN}$.

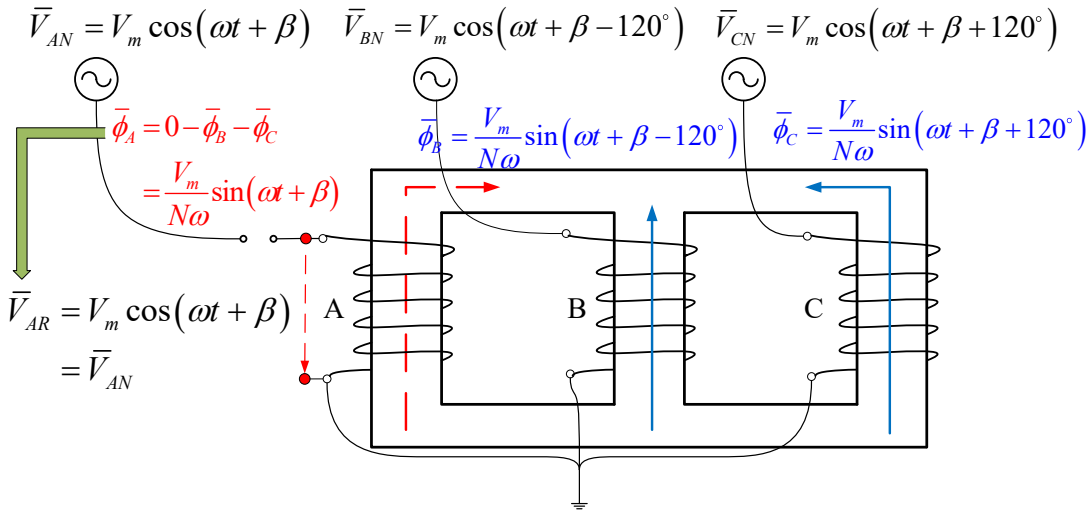

Figure 4.4 Voltage recreation due to magnetic coupling

The problem represents a unique open conductor detection challenge encountered by power plants, especially critical plants such as nuclear power plants and other safety-critical facilities that involve backup power supplies. The open conductor situation does not cause operational problems if the backup system is not energized. Thus, the goal is to detect the situation as soon as possible, hopefully before the backup system is energized. This is a pure open conductor detection problem while locating the open conductor point is not critical since the situation is within the power plant. However, few solutions are available to detect this open conductor situation, leaving this unsolved problem potentially jeopardizing power plants and power systems. In this chapter, two power-disturbance-based methods have been developed to effectively detect this open conductor condition. Once detected by the proposed methods, the open conductor is located with an onsite check and repaired subsequently.

4.2 Method 1: Natural Voltage Disturbance Based Scheme

This section presents a voltage disturbance based scheme developed for monitoring the open conductor condition. The key ideas of this method are (1) to use naturally occurring unbalanced voltage disturbances as the test signals and (2) to use the unique responses of the transformer neutral current to check the existence of the open conductor condition.

The proposed scheme was conceived from the following observation. When a voltage disturbance occurs at a point upstream from the unloaded transformer, the transformer will respond differently

depending on whether it has two or three phases connected to the system. This is especially true if the voltage disturbance is unbalanced. Thus, the basic idea of the proposed method is to use natural voltage disturbances as the test signals and the associated transformer neutral current response to check if an open conductor condition exists.

4.2.1 Equivalent Circuit Analysis

An open conductor condition can be modelled in the phase domain as a resistor of infinite resistance inserted into the opened phase (assume that phase A is open), as shown in Figure 4.5(a). The open conductor condition equivalent impedance $\mathbf{R}_s$ in the sequence domain can be, therefore, obtained as follows:

$$\mathbf{R}_s = \begin{bmatrix} 1 & 1 & 1 \\ \alpha^2 & \alpha & 1 \\ \alpha & \alpha^2 & 1 \end{bmatrix}^{-1} \begin{bmatrix} R & 0 & 0 \\ 0 & 0 & 0 \\ 0 & 0 & 0 \end{bmatrix} \begin{bmatrix} 1 & 1 & 1 \\ \alpha^2 & \alpha & 1 \\ \alpha & \alpha^2 & 1 \end{bmatrix} = \frac{1}{3} \begin{bmatrix} R & R & R \\ R & R & R \\ R & R & R \end{bmatrix} \tag{4.1}$$

where $\alpha = -\frac{1}{2} + \mathrm{j}\frac{\sqrt{3}}{2}$, $\alpha^2 = -\frac{1}{2} - \mathrm{j}\frac{\sqrt{3}}{2}$, and R is infinity. The equivalent circuit of the open conductor condition in the sequence domain is shown in Figure 4.5(b).

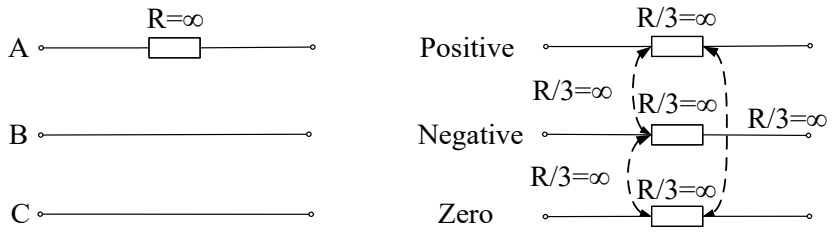

(a) Phase domain (b) Sequence domain

Figure 4.5 Equivalent circuits of phase A open conductor condition

Therefore, for the system of Figure 4.2, the sequence admittance of the circuit downstream from the main bus (denoted as $\mathbf{Y}_{occ}$ and illustrated in Figure 4.6) can be transformed from the sum of the open conductor condition equivalent impedance $\mathbf{R}_s$ in (4.1) and the transformer impedance $\mathbf{Z}_{Ts}$, as follows:

$$\mathbf{Y}_{occ} = \left(\mathbf{R}_s + \mathbf{Z}_{Ts}\right)^{-1} = \begin{bmatrix} Z_{T1}+\frac{1}{3}R & \frac{1}{3}R & \frac{1}{3}R \\ \frac{1}{3}R & Z_{T1}+\frac{1}{3}R & \frac{1}{3}R \\ \frac{1}{3}R & \frac{1}{3}R & Z_{T0}+\frac{1}{3}R \end{bmatrix}^{-1} = \frac{1}{Z_{T1}+2Z_{T0}} \begin{bmatrix} 1+\frac{Z_{T0}}{Z_{T1}} & -\frac{Z_{T0}}{Z_{T1}} & -1 \\ -\frac{Z_{T0}}{Z_{T1}} & 1+\frac{Z_{T0}}{Z_{T1}} & -1 \\ -1 & -1 & 2 \end{bmatrix} \quad (4.2)$$

where $\mathbf{Z}_{Ts} = [\mathrm{Z}_{T1} \quad \mathrm{Z}_{T1} \quad \mathrm{Z}_{T0}]^T$ is the transformer sequence impedance, and Z_{T1} and Z_{T0} are the positive and zero sequence impedances, respectively.

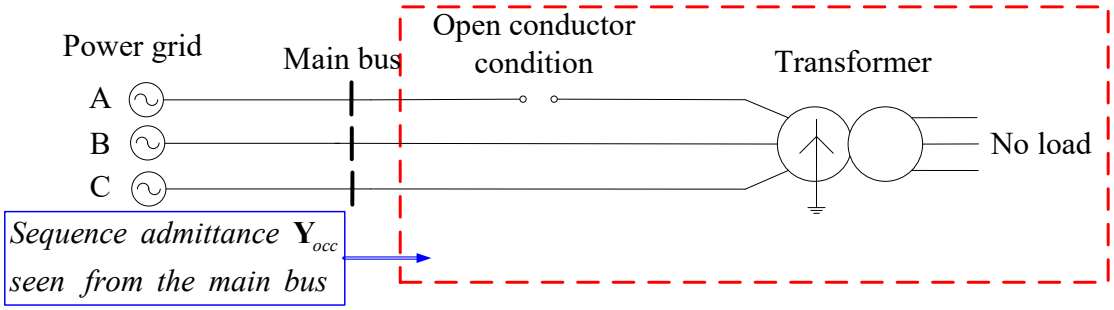

Figure 4.6 Illustration of downstream circuit sequence admittance

For the system of Figure 4.2, the equivalent circuits in the sequence domain can be established as Figure 4.7. The power system upstream from the main bus is modelled as a Thevenin equivalent in the circuits.

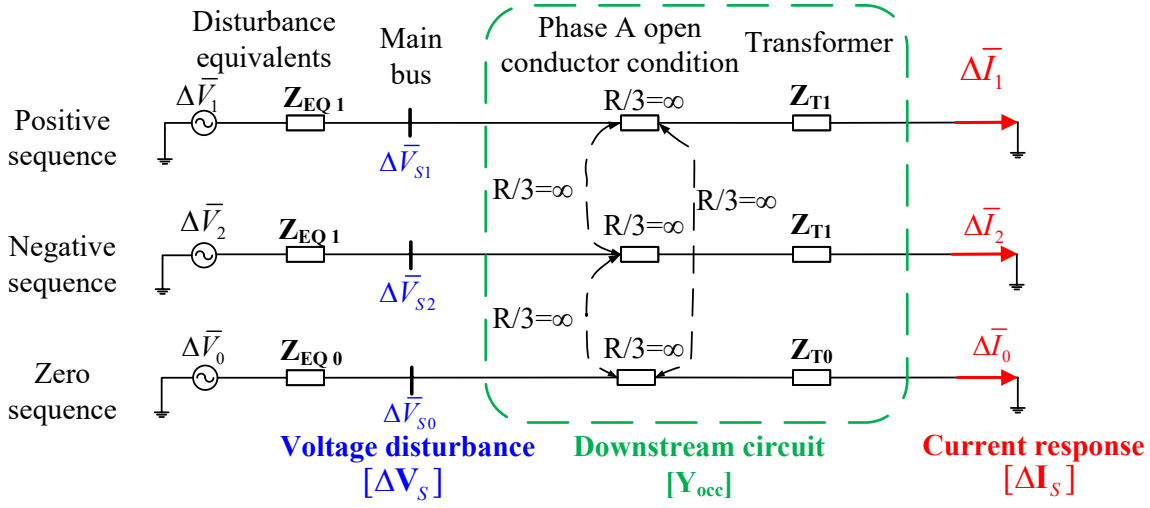

Figure 4.7 Equivalent circuits in sequence domain

In Figure 4.7, the sequence voltage disturbance, $\Delta\mathbf{V}_S = [\Delta\bar{V}_{S1} \quad \Delta\bar{V}_{S2} \quad \Delta\bar{V}_{S0}]^T$, experienced at the main bus, can be obtained as follows:

$$\begin{aligned}
\Delta\bar{V}_{S1} &= \frac{1}{3}(\Delta\bar{V}_{Sa} + \alpha\Delta\bar{V}_{Sb} + \alpha^2\Delta\bar{V}_{Sc}) \\
\Delta\bar{V}_{S2} &= \frac{1}{3}(\Delta\bar{V}_{Sa} + \alpha^2\Delta\bar{V}_{Sb} + \alpha\Delta\bar{V}_{Sc}) \\
\Delta\bar{V}_{S0} &= \frac{1}{3}(\Delta\bar{V}_{Sa} + \Delta\bar{V}_{Sb} + \Delta\bar{V}_{Sc})
\end{aligned} \tag{4.3}$$

where $\Delta\bar{V}_{Sa}$, $\Delta\bar{V}_{Sb}$, and $\Delta\bar{V}_{Sc}$ are measurements of three-phase voltage disturbances at the main bus, respectively.

Thus, the sequence current response $\Delta\mathbf{I}_S = [\Delta\bar{I}_1 \quad \Delta\bar{I}_2 \quad \Delta\bar{I}_0]^T$ in Figure 4.7 can be determined by substituting $\mathbf{Y}_{occ}$ obtained from (4.2) and $\Delta\mathbf{V}_S$ obtained from (4.3) into the nodal voltage equation $\Delta\mathbf{I}_S = \boldsymbol{Y}_{occ}\Delta\mathbf{V}_S$. The zero sequence current response $\Delta\bar{I}_0$ in $\Delta\mathbf{I}_S$ is given by

$$\Delta\bar{I}_0 = \frac{1}{Z_{T1} + 2Z_{T0}}\left(\Delta\bar{V}_{Sb} + \Delta\bar{V}_{Sc}\right) \tag{4.4}$$

4.2.2 Principle of the Method

The transformer neutral current response is triple the zero sequence current response and can be obtained from (4.4) as follows:

$$\Delta\bar{I}_{neu-occ} = 3\Delta\bar{I}_0 = \frac{3}{Z_{T1} + 2Z_{T0}}\left(\Delta\bar{V}_{Sb} + \Delta\bar{V}_{Sc}\right) \tag{4.5}$$

One can conclude from (4.5) that, under a phase A open conductor condition, the transformer neutral current response is determined by the voltage disturbances on the intact phases (phase B and phase C) and the unloaded transformer's zero and positive sequence impedances. Furthermore, due to the large positive sequence impedance, the transformer neutral current response has almost no zero sequence component for all types of voltage disturbances under the open conductor condition.

By contrast, the transformer neutral current response to the voltage disturbances under the normal operating condition is as follows:

$$\Delta\bar{I}_{neu-normal} = \frac{1}{Z_{T0}}\left(\triangle\bar{V}_{Sa} + \triangle\bar{V}_{Sb} + \triangle\bar{V}_{Sc}\right) \tag{4.6}$$

Equations (4.5) and (4.6) reveal the characteristics of the transformer neutral current response to the voltage disturbances. They are summarized in Table 4.1.

Table 4.1 Transformer neutral current response to voltage disturbances

$\left\|\Delta\bar{I}_{neu}\right\|$	Conditions	
	Normal operating condition	Phase A open conductor condition
Balanced voltage disturbance	$\left\|\frac{\Delta\bar{V}_{Sa} + \Delta\bar{V}_{Sb} + \Delta\bar{V}_{Sc}}{Z_{T0}}\right\|$ $(= 0)$	$3\left\|\frac{\Delta\bar{V}_{Sb} + \Delta\bar{V}_{Sc}}{Z_{T1} + 2Z_{T0}}\right\|$ (≈ 0)
Unbalanced voltage disturbance	$\left\|\frac{\Delta\bar{V}_{Sa} + \Delta\bar{V}_{Sb} + \Delta\bar{V}_{Sc}}{Z_{T0}}\right\|$ $(\neq 0)$	$3\left\|\frac{\Delta\bar{V}_{Sb} + \Delta\bar{V}_{Sc}}{Z_{T1} + 2Z_{T0}}\right\|$ (≈ 0)

As shown in Table 4.1, a balanced voltage disturbance does not induce a transformer neutral current change under the normal operating condition. However, it will stimulate a transformer neutral current change under the open conductor condition, but this change is insignificant due to the large positive sequence impedance of the unloaded transformer [88-90]. Thus, higher accuracy measurement instruments are in additional need so that the balanced voltage disturbances as the test signals can be used. By contrast, the transformer neutral current response to an unbalanced voltage disturbance is much more noticeable under the normal operating condition but limited to almost unnoticeable under the open conductor condition. Therefore, unbalanced voltage disturbances are preferred for use as the test signals in the proposed method.

An open conductor condition exists if an unbalanced voltage disturbance does not cause a noticeable neutral current change. A quantitative index to describe this condition can be established

as the ratio (K) between the change percentage of the zero sequence voltage at the system side (K_v) and the change percentage of the transformer neutral current (K_i). It is expressed as follows:

$$K = \frac{K_v}{K_i} = \frac{\left|\Delta \bar{V}_{S0} / \bar{V}_{S0}\right|}{\left|\Delta \bar{I}_{neu} / \bar{I}_{neu}\right|} \tag{4.7}$$

where $\Delta \bar{V}_{S0}$ is the change of the zero sequence voltage caused by a voltage disturbance at the main bus. $\Delta \bar{I}_{neu}$ is the transformer neutral current response to this voltage disturbance. $\bar{I}_{neu}$ and $\bar{V}_{S0}$ are the neutral current and zero sequence voltage before the voltage disturbance, respectively.

The detection index is calculated when a desirable unbalanced voltage disturbance is detected. According to the requirements of the IEEE standard, PTs' measurement accuracy deviation should be less than 1.2% of the rated voltage [91]. Thus, the unbalanced voltage disturbance is selected as the test signal if ΔV_{S0} is greater than 6% of the rated voltage, thus reducing the impact caused by PTs' measurement errors.

The following shows the mathematical analysis with practical considerations of the detection criterion. Under the normal operating condition, the equivalent circuits of the system with unloaded transformers can be decoupled in the sequence domain. The detection index K is solved in (4.8). It shows that the detection index K is always 1 under the normal operating condition.

$$K = \frac{\left|\Delta \bar{V}_{S0}\right|}{\left|\Delta \bar{I}_{neu}\right|} \cdot \frac{\left|\bar{I}_{neu}\right|}{\left|\bar{V}_{S0}\right|} = Z_{T0} \cdot Y_{T0} = 1 \tag{4.8}$$

Under the phase A open conductor condition, K_v and K_i can be calculated as follows:

$$K_v = \left|\frac{\Delta \bar{V}_{S0}}{\bar{V}_{S0}}\right| = \frac{\left|\Delta V_{S0} / V_{ph}\right|}{\left|V_{S0} / V_{ph}\right|} \quad \text{and} \quad K_i = \left|\frac{\Delta \bar{I}_{neu}}{\bar{I}_{neu}}\right| \tag{4.9}$$

where V_{ph} is the rated phase voltage.

It is shown in (4.9) that K_v is determined by the background voltage imbalance and the unbalanced voltage disturbance. In practice, the background voltage imbalance is at most 2-3% of the rated voltage [92]. When the detection index calculation is triggered, the zero sequence component of the voltage disturbance is greater than 6% of the rated voltage. Thus, K_v is always larger than 2. Meanwhile, based on the conclusions summarized in Table 4.1, during a desirable disturbance, the neutral current response $|\Delta\bar{I}_{neu}|$ is only a little under the open conductor condition. It is calculated by the subtraction of neutral currents during and before the disturbance. The neutral current itself has a measurable magnitude because the transformer is energized by a two-phase power supply. Therefore, K_i is small, approaching 0. As K_v has been proved to be larger than 2, the detection index ($K = K_v/K_i$) is a big value, much larger than 2 under the open conductor condition.

Considering that the detection index K is equal to 1 under the normal operating condition and is much larger than 2 under the open conductor condition, the threshold for the open conductor identification is recommended as 2. If the detection index is less than the threshold, the operating condition is determined normal; if the detection index is greater than the threshold, the open conductor condition is identified.

4.2.3 Implementation and Practical Considerations

Implementation issues, including the hardware deployment and the monitoring algorithm, and the prevalence of voltage disturbances are discussed to develop the proposed open conductor detection method into a practical application scheme.

4.2.3.1 Hardware Deployment

Figure 4.8 presents the hardware deployment of the proposed method. It requires two power disturbance monitors to measure the voltage at the main bus and the current on the transformer neutral, respectively. The monitors are commonly equipped with signal processing modules to perform data analysis, GPS modules to receive the precision time signal, and communication modules to transmit recorded data. Since both power disturbance monitors are in one power plant, the sampled data at each location is tagged using substation clock signals and is transmitted to the

processing unit using the substation Ethernet [19]. The processing unit synchronizes the data from both monitors based on the precision time tag and runs the detection algorithm.

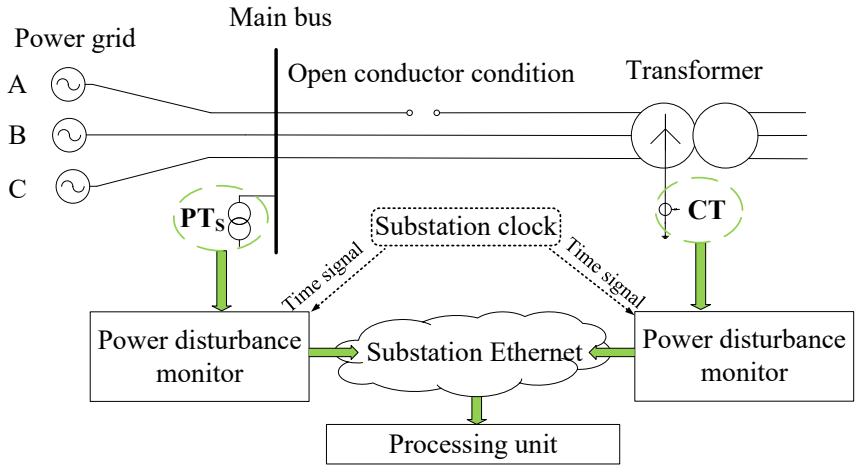

Figure 4.8 Illustration of hardware deployment

4.2.3.2 Monitoring Algorithm

The monitoring algorithm is shown in the flowchart of Figure 4.9 and is explained as follows. The main bus phase voltages and transformer neutral current are continuously monitored by power disturbance monitors. Power frequency components of the voltage and the current are extracted using the Discrete Fourier Transform (DFT) algorithm implemented in the signal processing module. A phase domain to sequence domain transformation is adopted to obtain the zero sequence voltage at power frequency. After a desirable unbalanced voltage disturbance ($\Delta V_{S0} \geq 6\% V_{ph}$) is detected, the changes in the power-frequency neutral current and zero sequence voltage are calculated by subtracting the pre-disturbance value from the during-disturbance values, respectively. Then, the voltage change ratio K_v and the synchronized neutral current change ratio K_i are determined. Consequently, the detection index K is calculated, and the detection criterion is applied to identify the operating condition. An alarm signal is sent if an open conductor condition is identified.

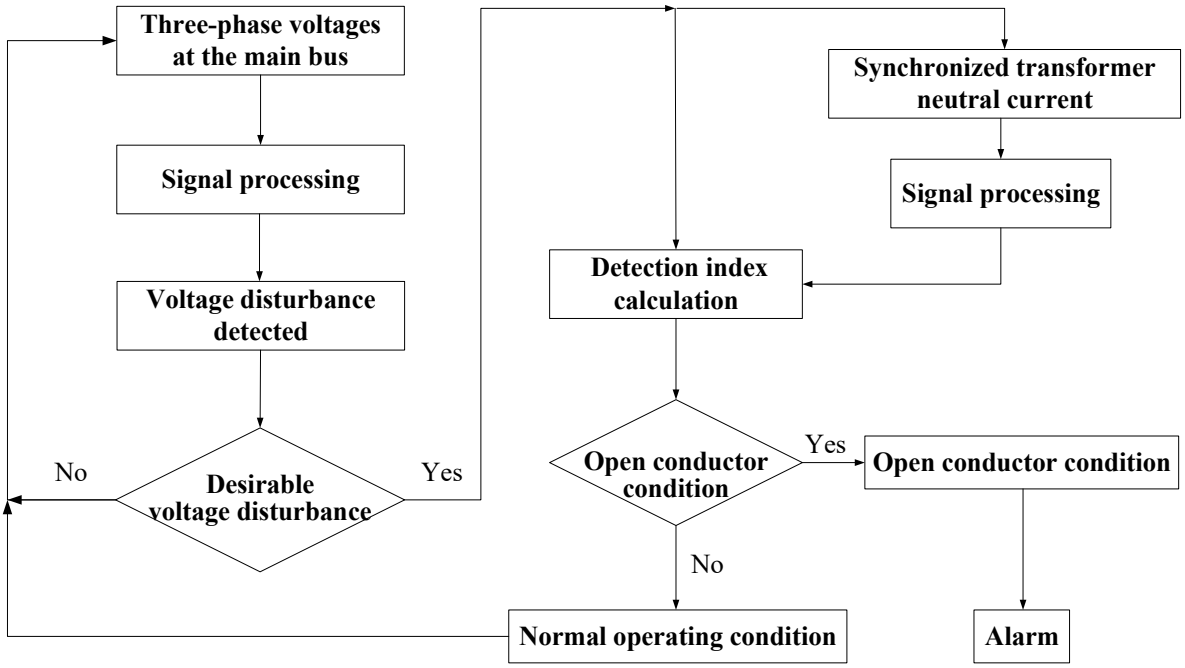

Figure 4.9 Monitoring algorithm flowchart

4.2.3.3 Prevalence of Voltage Disturbance

The proposed method requires the existence of upstream voltage disturbances. Therefore, a survey has been conducted to check how often a voltage disturbance may occur. Reference [13] showed that a bus experienced 45 fault-caused voltage sags in 17 months. Reference [93] presented 16 severe voltage sags in 3.5 months at a power plant distribution bus. Reference [94] showed 4.94 voltage sags happened per month per monitoring bus. The survey [95] showed that 7.05 voltage sags were found per month per monitoring bus in 9 European countries. These field-measurement-based statistics show that voltage disturbances are common in power systems.

The problem to be solved is a condition monitoring problem rather than a protection problem. The open conductor does not cause any operational issues if the backup system is not energized. The goal is to detect the open conductor condition as soon as possible, hopefully before the backup system is energized. In other words, the immediate detection of this problem is not necessary. Therefore, the frequency of occurrence of natural power disturbances is sufficient to detect this open conductor condition.

4.2.4 Simulation Studies

An IEEE test system [96] was built in MATLAB/Simulink to study the effectiveness and robustness of the proposed scheme. The test system consists of 13 buses, and it is representative of a medium-sized industrial plant. The single-line diagram is shown in Figure 4.10.

The power frequency of the test system is 60Hz. The power plant is fed from an equivalent utility supply of 69kV, and the local plant distribution system operates at 13.8kV. The transformer Tr1 between Bus 9 and Bus 10 has no loads connected to its secondary side. It has Y_g-Δ connected windings and a three-legged core, with a capacity of 1.5MVA and a voltage ratio of 13.8/0.48kV. The transformer's short-circuit resistance and reactance are 0.8743% and 5.6831%, respectively. The zero sequence magnetizing impedance Z_{M0} is j63.482Ω. The positive sequence magnetizing resistance R_m is 63480Ω, and the positive sequence magnetizing inductance L_m is 168.39H. Therefore, its positive sequence magnetizing impedance Z_{M1} is 31741+j31740Ω. The motor at Bus 7 has a capacity of 1.25MVA.

The voltage disturbances are introduced by phase-to-ground faults at the power supply side (illustrated by the red sign in Figure 4.10) and motor starting, respectively. All disturbances last for five cycles at the end of the total ten cycles. Phase B of the power line between Bus 3 and Bus 9 is set to be open (if necessary). The sampling rate of both monitors is 256 points/cycle.

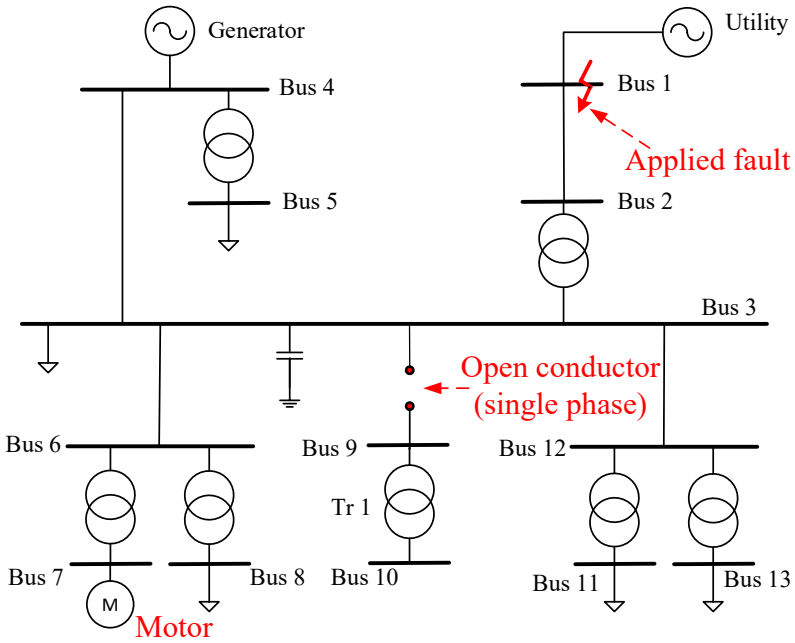

Figure 4.10 IEEE 13-bus test system

4.2.4.1 Verifications of Unbalanced Voltage Disturbance Based Scheme

A single-phase-to-ground (Cg) fault is first applied to verify the effectiveness of the proposed scheme. The monitor at Bus 3 detects a desirable unbalanced voltage disturbance ($\Delta V_0 = 20\% V_{ph}$). The three-phase voltage waveforms at Bus 3 are shown in Figure 4.11.

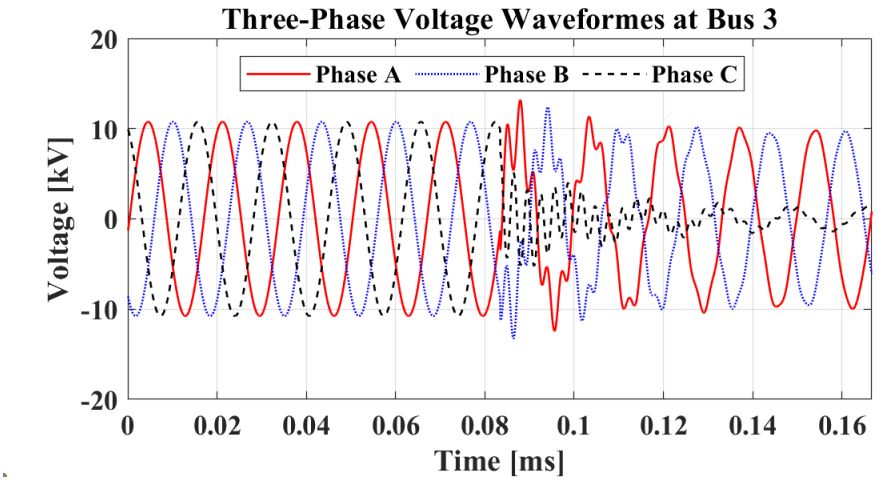

Figure 4.11 Three-phase voltage waveforms at Bus 3 for a case with an unbalanced voltage disturbance caused by a Cg fault

Under the phase B open conductor condition, the transformer neutral current waveform and the detection index are presented in Figure 4.12. It shows that the neutral current response to this voltage disturbance is about 0.07A. The calculated detection index is stable and much larger than the threshold during the disturbance. Thus, the open conductor condition is detected.

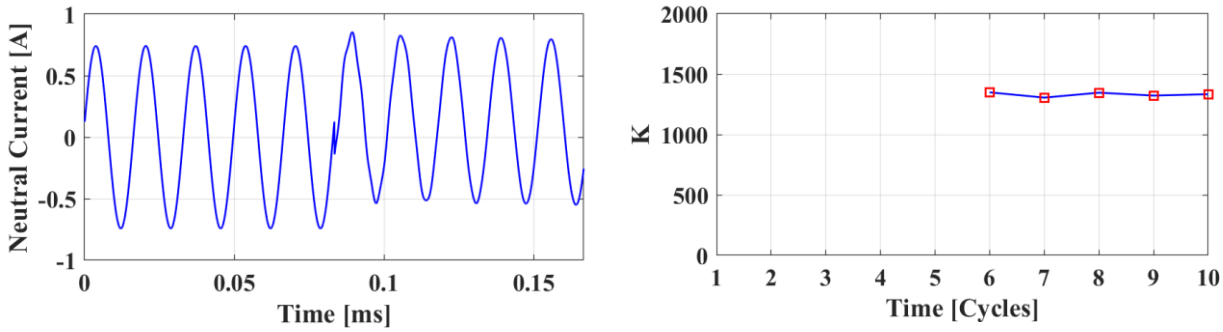

(a) Neutral current waveform (b) Detection index

Figure 4.12 Neutral current response results under the phase B open conductor condition

Under the normal operating condition, Figure 4.13 illustrates a significant neutral current response to this voltage disturbance. The detection index is always calculated around 1, which is less than the threshold during the disturbance. Thus, the normal operating condition is identified.

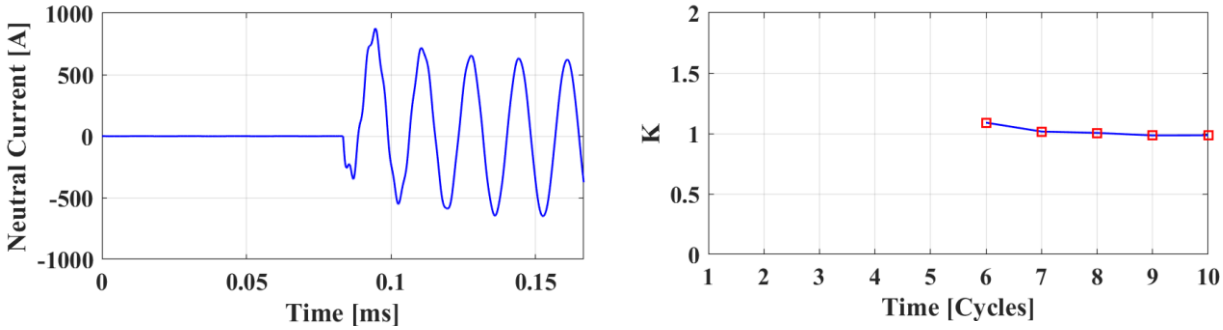

(a) Neutral current waveform (b) Detection index

Figure 4.13 Neutral current response results under the normal operating condition

As a two-phases-to-ground (CAg) fault is applied, a desirable voltage disturbance ($\Delta V_0 = 10\% V_{ph}$) at Bus 3 is monitored. The three-phase voltage waveforms are presented in Figure 4.14.

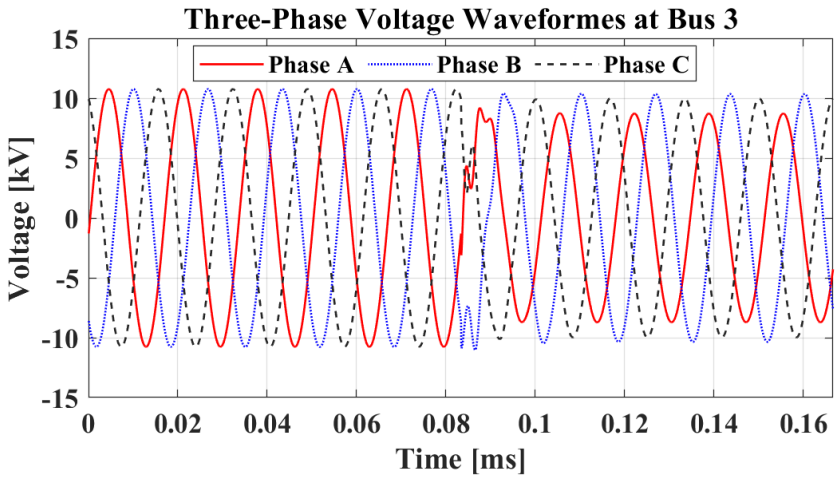

Figure 4.14 Three-phase voltage waveforms at Bus 3 for a case with an unbalanced voltage disturbance caused by a CAg fault

Under the phase B open conductor condition, the transformer neutral current waveform and the detection index are shown in Figure 4.15. It shows that there is almost no neutral current response. The detection index is stable and always much larger than the threshold during the disturbance. Thus, the open conductor condition is detected.

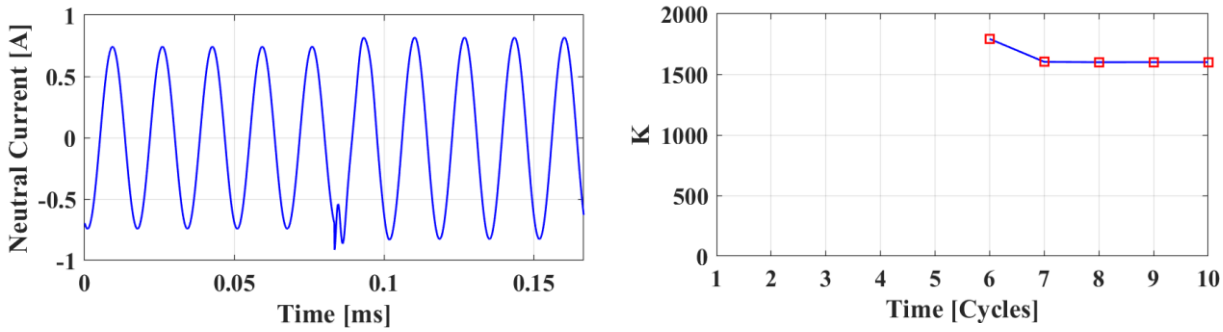

(a) Neutral current waveform (b) Detection index

Figure 4.15 Neutral current response and detection index during the CAg fault under the phase B open conductor condition

Under the normal operating condition, a significant neutral current response to the same disturbance and the detection index are shown in Figure 4.16. The detection index is always around 1, less than the threshold, indicating that the operating condition is normal.

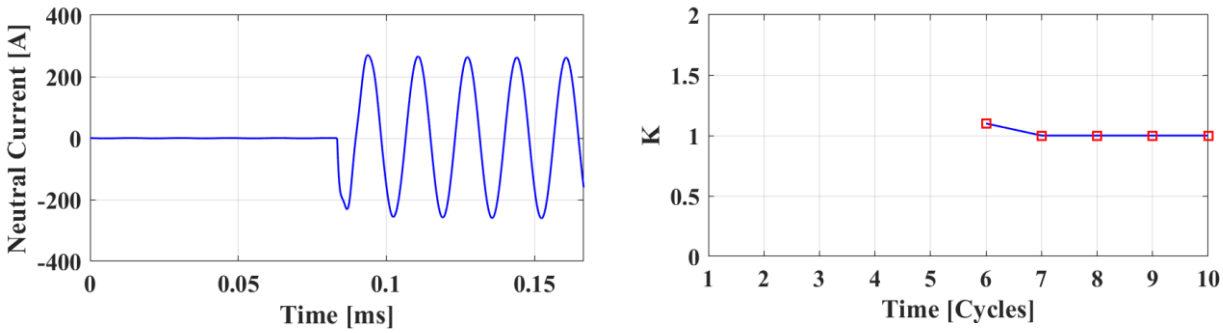

(a) Neutral current waveform (b) Detection index

Figure 4.16 Neutral current response and detection index during the CAg fault under the normal operating condition

It is shown from the two cases above that the proposed scheme can effectively distinguish the open conductor condition from the normal operating condition.

4.2.4.2 Verifications of Balanced Voltage Disturbance Based Scheme

The motor starting event is applied to generate balanced voltage disturbances. The three-phase voltage waveforms at Bus 3 are presented in Figure 4.17.

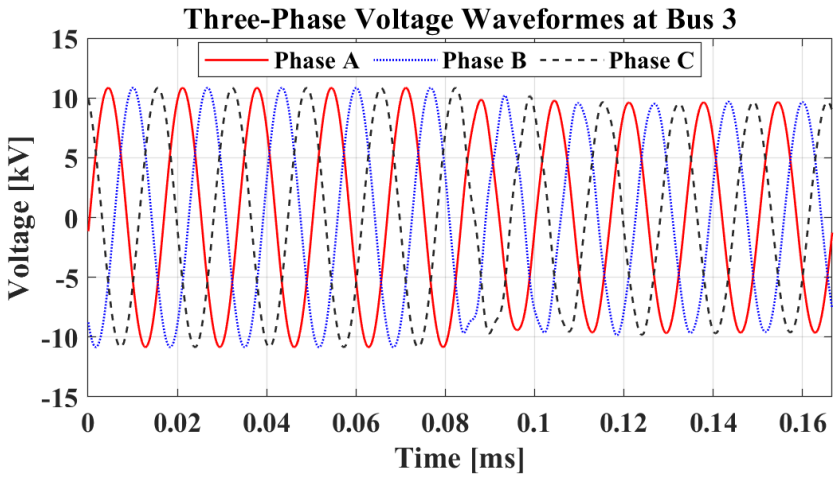

Figure 4.17 Three-phase voltage waveforms at Bus 3 containing a balanced voltage disturbance caused by the motor starting

Under both operating conditions, the transformer neutral current responses to a balanced voltage disturbance are in small magnitudes, as shown in Figure 4.18. This proves that the balanced voltage disturbance is not a good test signal as a high accuracy CT is needed.

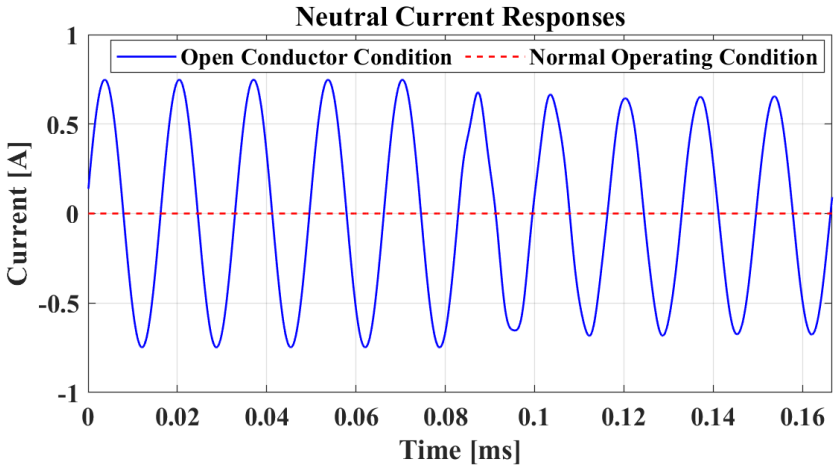

Figure 4.18 Neutral current responses to a balanced voltage disturbance under both operating conditions

4.2.4.3 Impact of Background Voltage Imbalance

The International Electrotechnical Commission (IEC) recommends that the degree of background voltage imbalance should be limited to 2%. Meanwhile, the American National Standard (ANSI) C84.1 recommends a maximum voltage imbalance limit of 3% for electric power systems [92]. In

the simulations, the voltage of phase A is changed to simulate a background voltage imbalance from -3% to 3%. The 10th cycle detection index under both operating conditions is presented in Figure 4.19 and Figure 4.20. These two figures confirm that the proposed scheme can work effectively within the maximum range of background voltage imbalance.

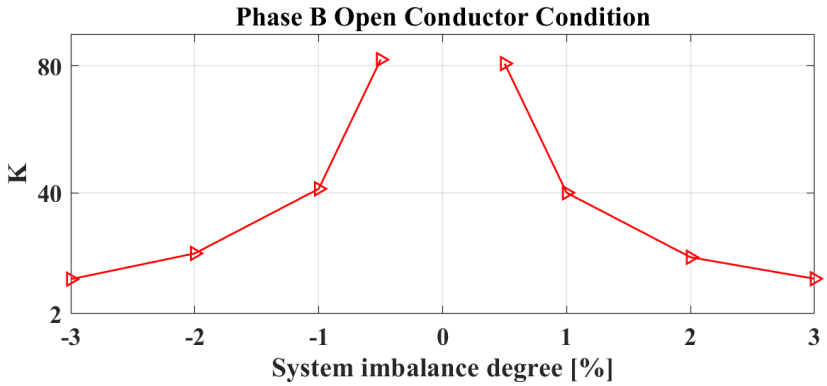

Figure 4.19 Detection index under phase B open conductor condition with different degrees of system imbalance

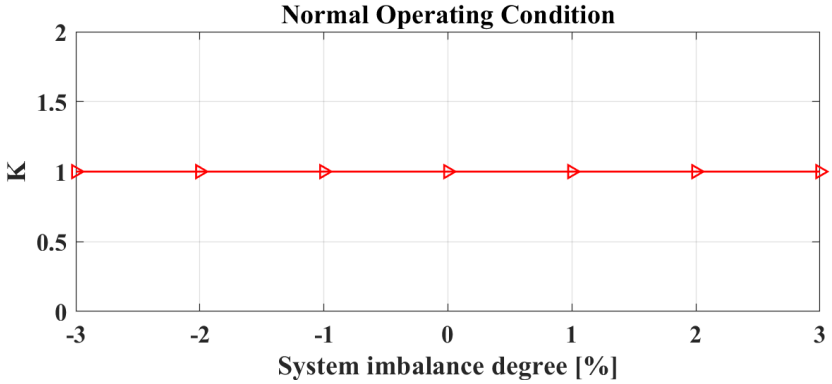

Figure 4.20 Detection index under the normal operating condition with different degrees of system imbalance

4.2.5 Experimental Verification

The proposed scheme has been investigated through laboratory experiments. The experimental system is shown in Figure 4.21. The experimental transformer is 120/208V, and Y_g-Δ connected with a three-legged core configuration. Its capacity is 30kVA. No loads are connected to its secondary side. One phase of the line between the system side bus and the transformer side bus is set to be opened (if necessary). A three-phase 10Ω resistor is added between the power supply and

the system side bus to trigger large enough voltage disturbances. The unbalanced voltage disturbance is introduced by energizing a single-phase heater connecting at the system side bus. Two power disturbance monitors are installed at the main bus and the transformer neutral.

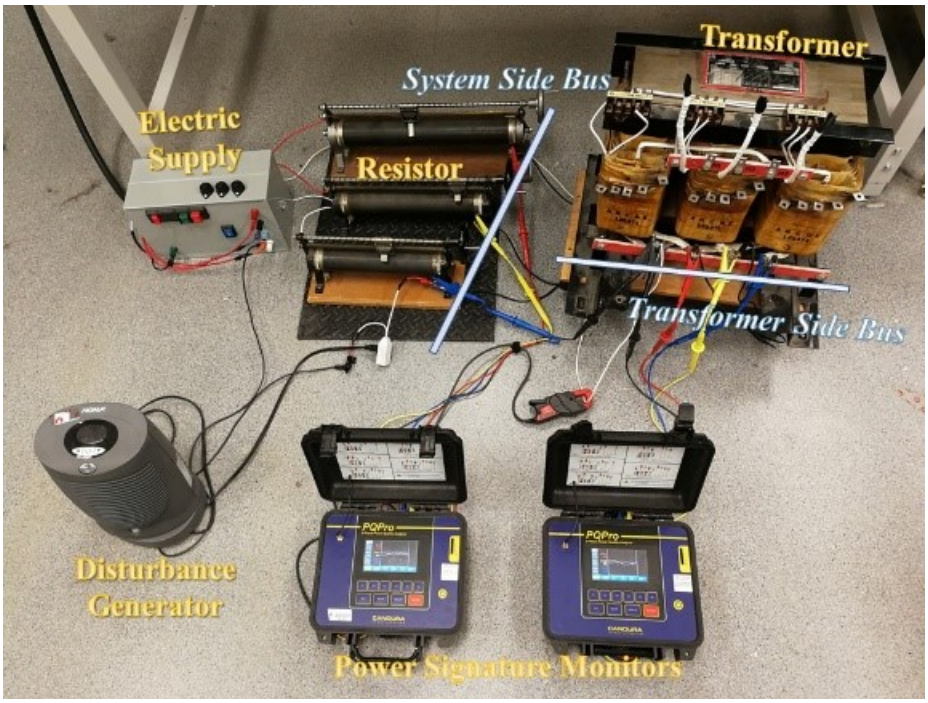

Figure 4.21 Experimental system

This section presents two representative cases. Ten cycles of measurement data are presented in each case — the first five cycles are before the disturbance, and the remaining five cycles are during the disturbance. To simplify the illustration, some voltages and currents are presented in magnitude.

Case 1: Phase B open conductor condition with an unbalanced voltage disturbance applied on phase C.

Figure 4.22 illustrates that the neutral current response is around 0.7A. The detection index is stable at 3.8, consistently above the threshold during the disturbance. Therefore, the open conductor condition is detected.

Case 2: Normal operating condition with an unbalanced voltage disturbance applied on phase C.

Figure 4.23 shows that the neutral current response is about 2.2A, and the detection index is stable at around 0.5 during the disturbance. Therefore, the normal operating condition is detected.

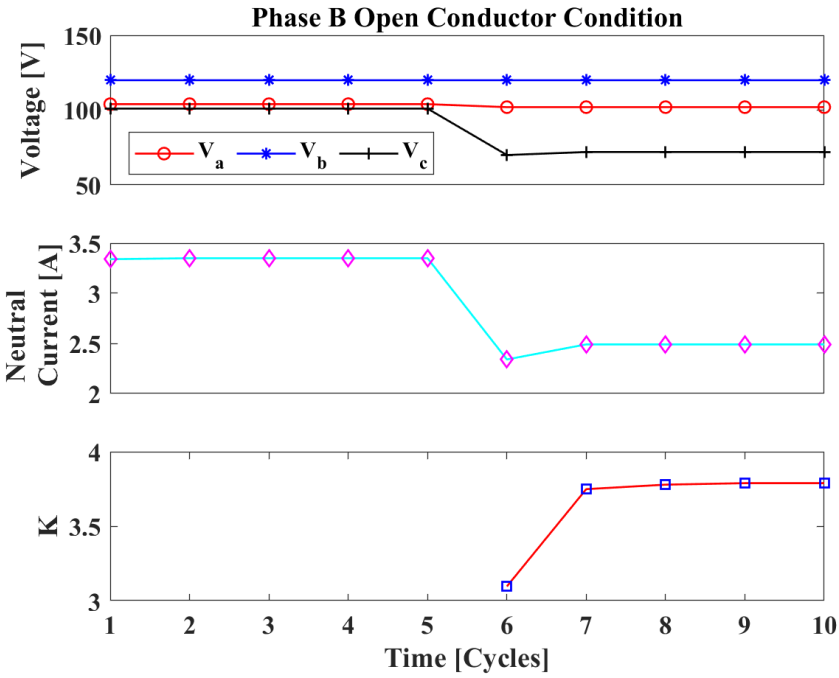

Figure 4.22 The experimental results of case 1 (open conductor condition)

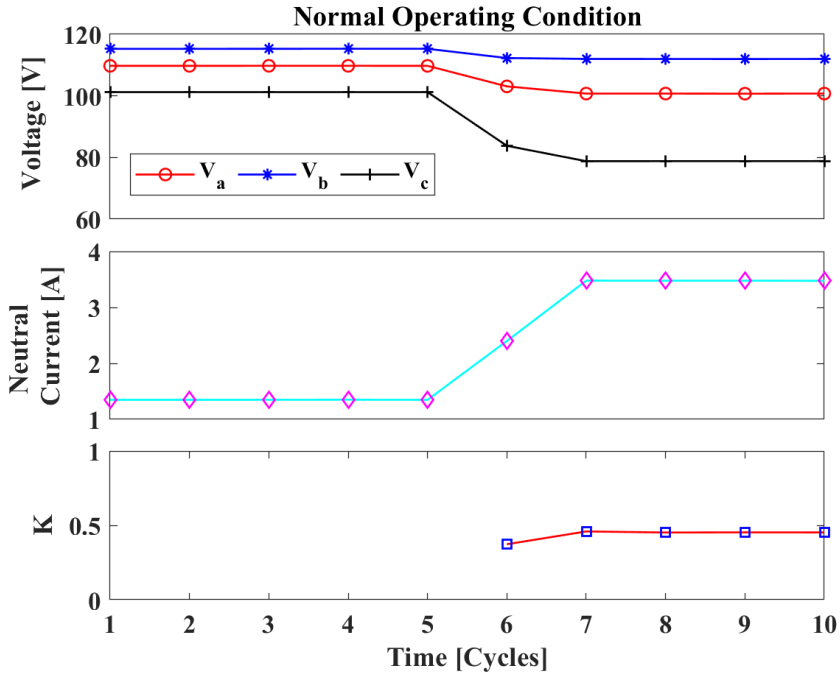

Figure 4.23 The experimental results of case 2 (normal operating condition)

It is worthwhile noting that the detection index for both operating conditions does not precisely match the theoretical value. This is because the transformer used in the experiment is three-phase unbalanced due to aging.

4.2.6 Summary

A novel method for detecting the open conductor condition is proposed. The method uses natural unbalanced voltage disturbances as the test signals. By analyzing the responses of the transformer neutral current to the voltage disturbance, a detection index is developed as an indicator to detect the open conductor condition. The implementation and practical considerations of the proposed method are discussed. Simulation and experimental results prove that the technique effectively monitors the open conductor condition.

4.3 Method 2: Natural 3rd Harmonic Power Based Scheme

Since the voltage-disturbance-based method proposed above needs certain natural disturbances to perform the detection, it cannot detect the open conductor condition immediately. In view of this limitation, a novel and advanced method is developed using 3rd harmonic power. This method detects the open conductor condition immediately and works as simply as a zero sequence power relay.

4.3.1 Zero Sequence Component Based Detection Idea

The phenomenon of the voltage recreation at the open phase illustrated in Figure 4.3 and Figure 4.4 is closely related to the fact that the three-phase supply voltages are in positive sequence. If the supply voltages were in zero sequence, the phenomenon would not exist. For example, when a zero sequence voltage is applied to the main bus, the transformer will exhibit distinct voltage responses for the cases with and without an open conductor condition. Therefore, the key idea of the proposed method is to use zero sequence components for open conductor detection.

For normal power systems, the zero sequence voltage at power frequency is very low (less than 2%), and the corresponding zero sequence current is also low. It is, therefore, challenging to detect the change of power-frequency zero sequence components. Like the power frequency, the

sequence components of harmonics can also be transformed from phase domain quantities at the corresponding harmonic orders using symmetrical components transformation. It is well known that the 3rd harmonics in power systems have a significant zero sequence component. In fact, zero sequence is the dominant component in 3rd and other triple harmonics [97]. As an example, Figure 4.24 shows a field measured 3rd harmonic voltage at a 13.8kV bus in Alberta. The zero sequence component is about three times that of the positive sequence voltage. References [80-83] conducted in-depth investigations on the characteristics of harmonic distortions in various power systems. The findings showed that rich 3rd harmonics exist at various locations and voltage levels. Therefore, it is feasible and practical to use the zero sequence component of 3rd harmonics to detect the open conductor condition.

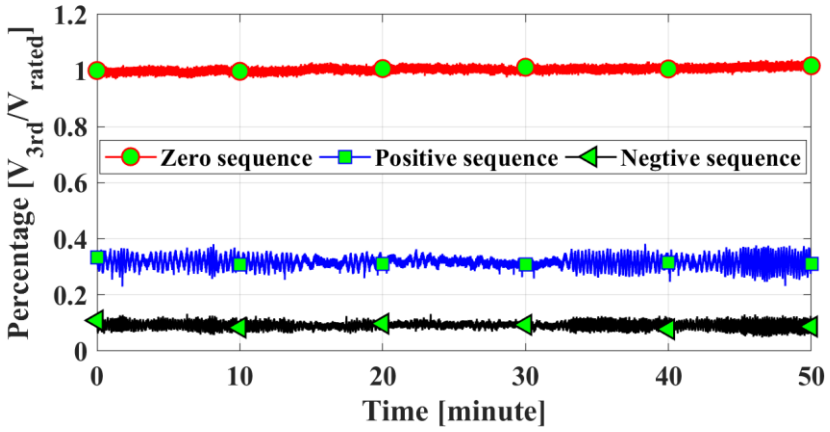

Figure 4.24 3rd harmonics in the field measurement

4.3.2 Impact of Open Conductor on Zero Sequence Component

Based on the superposition principle, the response of the system shown in Figure 4.2 to a zero sequence voltage can be studied by assuming there is only a zero sequence voltage at the main bus. This means:

$$V_0(h) = V_{TA}(h) + V_{TB}(h) + V_{TC}(h) \neq 0 \tag{4.10}$$

where $V_{TA}(h)$, $V_{TB}(h)$, and $V_{TC}(h)$ are three-phase voltages at the hth harmonic at the transformer terminal. h refers to the 3rd harmonic if there is no other specification in this chapter.

Under the normal operating condition, the zero sequence current flowing into the transformer can be determined using the zero sequence circuit as follows:

$$I_0(h) = V_0(h) / Z_0(h) \neq 0 \tag{4.11}$$

where $Z_0(h)$ is the zero sequence impedance downstream from the transformer terminal.

Under the open conductor condition (e.g., phase A is open), the voltages on the main bus only energize the transformer's primary phases B and C. Thus, as shown in Figure 4.25, the voltages (denoted as $V_2(h)$, and $V_3(h)$) across the two corresponding secondary windings are induced, respectively.

$$V_2(h) = V_{TB}(h) / n_T \quad \text{and} \quad V_3(h) = V_{TC}(h) / n_T \tag{4.12}$$

where n_T is the transformation ratio between the transformer primary and secondary windings.

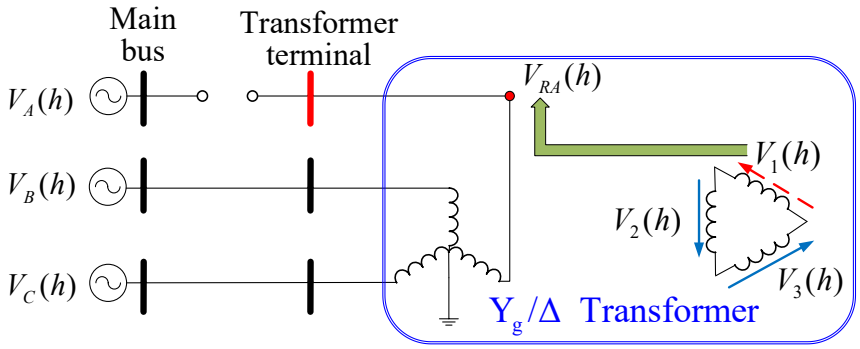

Figure 4.25 Voltage regeneration on the opened phase in the $\mathbf{Y_g}$-Δ transformer

In the secondary Δ windings, the voltage across the third winding, denoted as $V_1(h)$, is created by $V_2(h)$ and $V_3(h)$, as follows:

$$V_1(h) = 0 - V_2(h) - V_3(h) = -\left(V_{TB}(h) + V_{TC}(h)\right) / n_T \tag{4.13}$$

The voltage in (4.13) will induce a voltage on the opened phase A, as follows:

$$V_{RA}(h) = n_T \cdot V_1(h) = -\left(V_{TB}(h) + V_{TC}(h)\right) \tag{4.14}$$

where $V_{RA}(h)$ is the re-built voltage at the phase A transformer terminal.

Thus, the three-phase voltages at the transformer terminal add to zero, as follows:

$$V_{RA}(h) + V_{TB}(h) + V_{TC}(h) = 0 \tag{4.15}$$

This reveals that there will be no zero sequence voltage at the transformer terminal if one conductor is open.

Since the zero sequence voltage is zero at the transformer terminal, the zero sequence current entering the transformer is also zero, i.e.,

$$I_0(h) = I_{TA}(h) + I_{TB}(h) + I_{TC}(h) = 0 \tag{4.16}$$

The above conclusion also holds for the three-legged transformer that has $\mathrm{Y_g}$ primaries and Y or $\mathrm{Y_g}$ secondaries.

4.3.3 Potential Detection Criteria

In summary, an open conductor condition can exhibit unique voltage and current characteristics if it is analyzed from the zero sequence perspective. At the primary side of the unloaded transformer, both the voltage and current in zero sequence will drop to zero once a conductor is open. Thus, there are three possible criteria to detect the open conductor condition.

1) Voltage-Based Detection Criterion

Based on the characteristics of the zero sequence voltage response, a voltage-based detection criterion is developed as follows:

$$\left|V_0(h)\right| \le \varepsilon_v(h) \tag{4.17}$$

where $V_0(h)$ is the voltage detection index, obtained from the zero sequence voltage measurement at the transformer terminal. $\varepsilon_v(h)$ is a user-defined threshold.

2) Current-Based Detection Criterion

Similarly, based on the characteristics of the zero sequence current response, a current-based detection criterion is developed as follows:

$$|I_0(h)| \leq \varepsilon_I(h) \tag{4.18}$$

where $I_0(h)$ is the current detection index, obtained from the zero sequence current measurement at the transformer terminal. $\varepsilon_I(h)$ is a user-defined threshold.

3) Power-Based Detection Criterion

Since both the zero sequence voltage and current drop to zero once an open conductor occurs, a detection index in the form of power is proposed as follows:

$$S_0(h) = |V_0(h)| \cdot |I_0(h)| \tag{4.19}$$

where $S_0(h)$ is the power detection index. Thus, a power-based detection criterion for the open conductor detection is developed, as follows:

$$|S_0(h)| \leq \varepsilon_S(h) \tag{4.20}$$

where $\varepsilon_S(h)$ is a user-defined threshold.

4) Index Processing, Threshold Setting, and Decision Making

Since the 3rd harmonic contains a rich zero sequence component, it is used to form the above indices. The DFT algorithm is applied on the measured zero sequence current and voltage waveforms to extract the 3rd harmonic quantities in the zero sequence. The RMS values of the zero sequence voltage, current, and power at the 3rd harmonics are obtained.

To reduce adverse impacts of noise and abnormal harmonic changes, such as a sudden outburst or interruption, raw indices are further processed with a moving average algorithm as follows:

$$X^P(h) = \frac{1}{N_m} \sum_{p=k-N_m+1}^{k} X_k^P(h) \tag{4.21}$$

where $X_k^p(h)$ refers to the raw index at the kth cycle, which can be either $I_0(h)$, $V_0(h)$, or $S_0(h)$. $X^p(h)$ is the processed index at the pth cycle, calculated with the moving average algorithm with a window length of N_m.

It is also important to set a proper threshold for each criterion. Based on the previous findings that each index drops and permanently stays at zero after an open conductor occurs, the threshold for each detection criterion can be determined in the following.

First, a daily profile of 3rd harmonic zero sequence voltage at the transformer terminal is monitored. Figure 4.26 illustrates a real-world 3rd harmonic zero sequence voltage daily profile on a 13.8kV bus in Alberta. It is similar to a daily load curve, having a clear magnitude fluctuation. Second, the minimum voltage (denoted as $V_{th}(h)$) in the profile is used as the threshold $\varepsilon_v(h)$ for the voltage based detection criterion. If the minimum value here is less than 0.15%, this value is excluded, and the second-lowest value is used, and so on. If the 3rd harmonic zero sequence voltage measurements in the first 24-hour monitoring are all less than 0.15%, the threshold will not be set, and the proposed method will not be applied. Third, thresholds for current based and power based detection criteria (i.e., $\varepsilon_I(h)$ and $\varepsilon_S(h)$) are determined in $V_{th}(h)/Z_0(h)$ and $V_{th}^2(h)/Z_0(h)$, respectively. $Z_0(h)$ is the 3rd harmonic zero sequence impedance downstream from the transformer terminal. This impedance is the ratio of 3rd harmonic zero sequence voltage and current, expressed as $V_0(h)/I_0(h)$, where $V_0(h)$ and $I_0(h)$ are the transformer terminal's zero sequence voltage and current at the 3rd harmonics, respectively. Specifically, $Z_0(h)$ consists of the transformer's zero sequence impedance and the downstream load's zero sequence impedance. $Z_0(h)$ does not exhibit significant changes, since the transformer supplies a backup system (i.e., the load is normally zero).

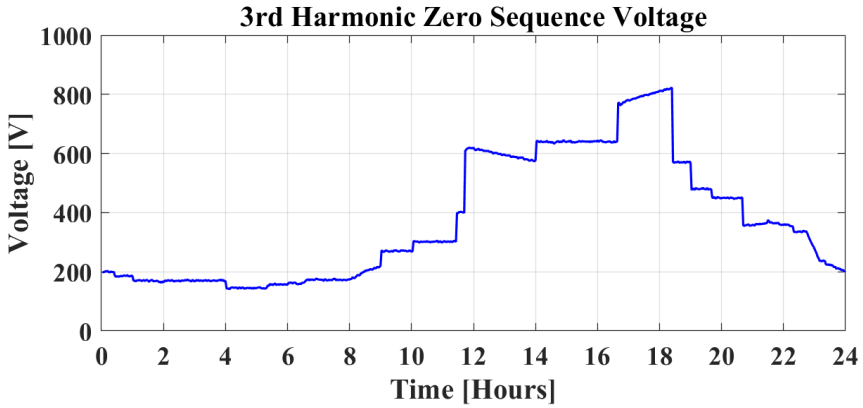

Figure 4.26 Illustration of a real-world 3rd harmonic zero sequence voltage daily profile

It is worthwhile noting that the thresholds are adaptive. The settings are updated daily based on the monitoring results from the previous day. When the occurrence of some special events, such as an open conductor or communication channel failure, disturbs the regular daily monitoring, the settings are updated using the monitoring results on the most recent normal day before the events. Note that the energization of the load in the backup power system may change $Z_0(h)$ and then affect the normal 3rd harmonic measurements. This situation is also treated as an abnormal event and excluded in the daily threshold adaption. On the other hand, if the load in the backup system has a noticeable impact on $Z_0(h)$, i.e., the backup load is put into service, the open conductor condition can be easily detected by using, for example, a negative sequence current relay. This is because an open conductor condition will result in a noticeable imbalance in the current feeding the load. In this situation, the proposed detection method is not necessary so that it can be temporarily out of service to avoid false detection. As such, the thresholds need no real-time corrections when the backup load is in service. In summary, the thresholds update daily and need no real-time modifications.

The decision-making strategy is presented in the following. The change of each index in a cycle-level snapshot around an open conductor event could satisfy the corresponding criterion (4.17), (4.18), or (4.20) to indicate the open conductor condition. Unfortunately, such a change can also be caused by a sudden dip of the system 3rd harmonic under normal operating conditions. This implies that an instant decision-making strategy may yield a false detection. Considering that open conductor detection is not required in real time, it is possible to make decisions with a time delay. The time delay is set as 1s to guarantee a confident detection. Thus, the decision-making strategy

is that if an index within 1s is always less than the threshold, the open conductor condition is seen to exist. The principle behind this strategy comes from the previous finding that detection indices drop to zero and would not change with the 3rd harmonic voltage fluctuations when an open conductor occurs. In addition, if the 3rd harmonic zero sequence voltage is lower than the voltage detection threshold $\varepsilon_v(h)$ in a short time (less than 1s), a warning signal will be sent to indicate the existence of temporarily low 3rd harmonic excitations. It is suggested that the open conductor decision made closely after the warning should be verified.

Note that the 3rd harmonic zero sequence current and voltage can be low in some systems. For such systems, the proposed method cannot work reliably. This is the main limitation of the proposed method. Due to this consideration, 3rd harmonic levels in various systems are investigated. As mentioned previously, field measurements and literature survey results in [80-83] reveal that rich 3rd harmonics exist in many systems. This is due to the widespread use of single-phase switched-mode power supplies and loads. Therefore, there is a good chance that the proposed method can work properly for many systems. Furthermore, two measures for checking the possible low 3rd harmonic level are adopted to guarantee a reliable detection. The first is to check the 3rd harmonic level in the first 24-hour monitoring to determine whether to apply the method; the other is to show the existence of low 3rd harmonic excitations during the following operations.

4.3.4 Verifications and Sensitivity Studies

Verifications and sensitivity studies of the proposed criteria are carried out through extensive simulation and experimental studies. The goals are (1) to test the performance of the proposed criteria and (2) to find the best criterion for further real-world application. This section presents some of the representative results and the corresponding discussions.

4.3.4.1 Simulation Verification

A 115kV backup power system was built in the “Multiphase Harmonic Power Flow (MHPF)” software to test the performance of the proposed indices/criteria. The test system consists of a Thevenin equivalent power source, a cable, and a transformer. The phase C conductor between the

cable terminal and the transformer is open (if necessary). The schematic of the test system is shown in Figure 4.27.

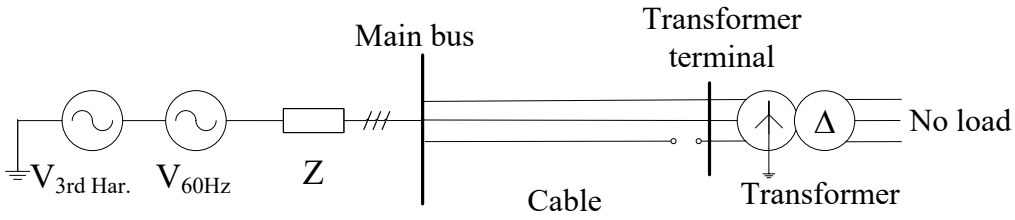

Figure 4.27 Simulation test system

The power frequency of the test system is 60Hz. At the power frequency, the system self- and mutual impedances are $Z_s(h=1)$ =0.0830+j3.3187Ω and $Z_m(h=1)$ =-0.0055+j0.6640Ω, respectively. A zero sequence voltage source is added in series with the system impedance to generate a 0.33% voltage harmonic for the 3rd harmonics on the main bus. This harmonic magnitude is from field data statistics in Alberta. A three-phase single-core cable feeds a Y_g-Δ unloaded transformer, which has a capacity of 35MVA and a voltage ratio of 115/13.8kV. The transformer's short-circuit resistance and reactance are 0.4698% and 7.9862%, respectively. The zero and positive sequence magnetizing impedances are j63.48Ω and 31741+j31740Ω, respectively.

For this test system, $Z_0(h)$ is calculated as 0.59+j29.82Ω. It is reasonable to assume that the minimum value in the daily profile of the 3rd harmonic zero sequence voltage is 0.2%. Thus, thresholds for the three criteria are set as 398.3V, 13.36A, and 5321VA, respectively. Detection indices under both operating conditions are presented in Table 4.2.

Table 4.2 Detection indices under both operating conditions

Indices	Normal operating condition	Open conductor condition
$V_0(h)$ (V)	528.5	0.9108
$I_0(h)$ (A)	17.72	0.0316
$S_0(h)$ (VA)	9364	0.0283

It can be seen from Table 4.2 that all indices are lower than the threshold under the open conductor condition, and they are larger than the threshold under the normal operating condition. This implies that all the proposed detection criteria can effectively detect the open conductor condition.

4.3.4.2 Experiment Verification

The proposed criteria have also been tested in laboratory experiments. The experimental test system is shown in Figure 4.28. The transformer is a 120/208V, Y_g-Δ connected three-phase bank transformer. It is directly fed by three-phase power from a lab wall outlet and has no load at the secondary side. One power quality monitor is placed at the transformer terminal to monitor the zero sequence current and voltage. The sampling rate of the monitor is 256 samples/cycle.

In the daily profile of the 3rd harmonic zero sequence voltage, the minimum value is 0.55V. This value is used as the voltage threshold $\varepsilon_v(h)$. In addition, the transformer terminal downstream impedance $Z_0(h)$ at the 3rd harmonics is obtained as 5Ω. Thus, the current and power thresholds $\varepsilon_I(h)$ and $\varepsilon_S(h)$ are set as 0.11A and 0.06VA, respectively.

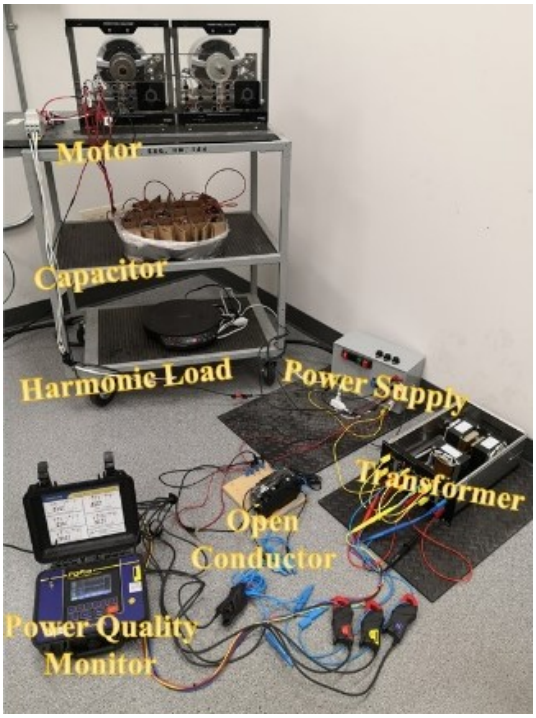

Figure 4.28 Experimental test system

Figure 4.29 shows a 200-cycle snapshot of the zero sequence voltages at all primary harmonic frequencies on the main bus. The 3rd harmonic is the largest component, around 0.75V (0.625%). At this moment, the 3rd harmonic zero sequence current is 0.16A, so the power index is obtained as 0.12VA. All three indices are above their thresholds. Once a conductor is open, all indices experience a drop and stay below the thresholds, as shown in Figure 4.30. One can conclude from Figure 4.30 that all the proposed criteria can detect the open conductor condition.

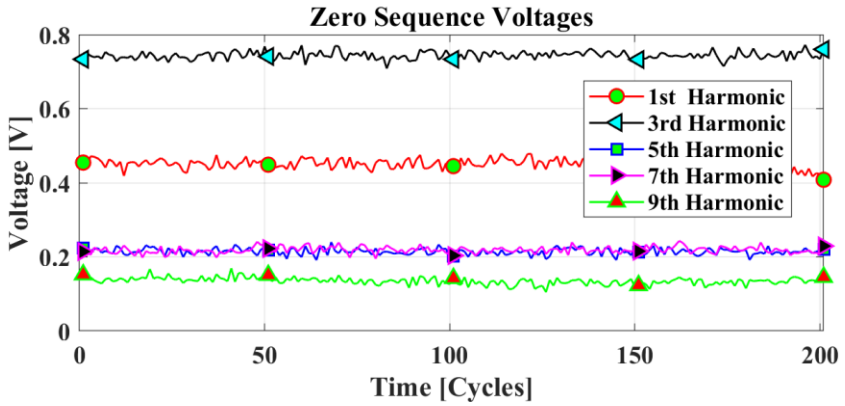

Figure 4.29 A 200-cycle snapshot of zero sequence voltages at all primary harmonic frequencies on the main bus

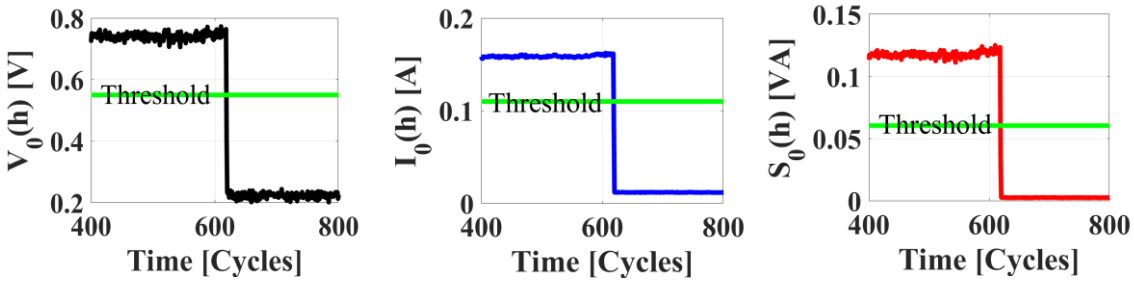

(a) Voltage index (b) Current index (c) Power index

Figure 4.30 Detection indices under both operating conditions

4.3.4.3 Sensitivity Studies

The simulation and experiment verifications above have proved that the proposed indices can independently detect the open conductor condition. Since these indices share the same philosophy, sensitivity studies are conducted to compare their performances. The goal is to find the best index.

One can see from the simulation results in Table 4.2 that the power index has the most significant drop (330883 times) compared to the voltage index (580 times) and the current index (561 times) when an open conductor occurs. This implies that the power index is the most sensitive in perceiving the open conductor condition.

In a further investigation, different 3rd harmonic zero sequence voltages are applied as a series of test voltages on the experimental test system to evaluate the sensitivity of detection indices. The performances of each index are shown as follows:

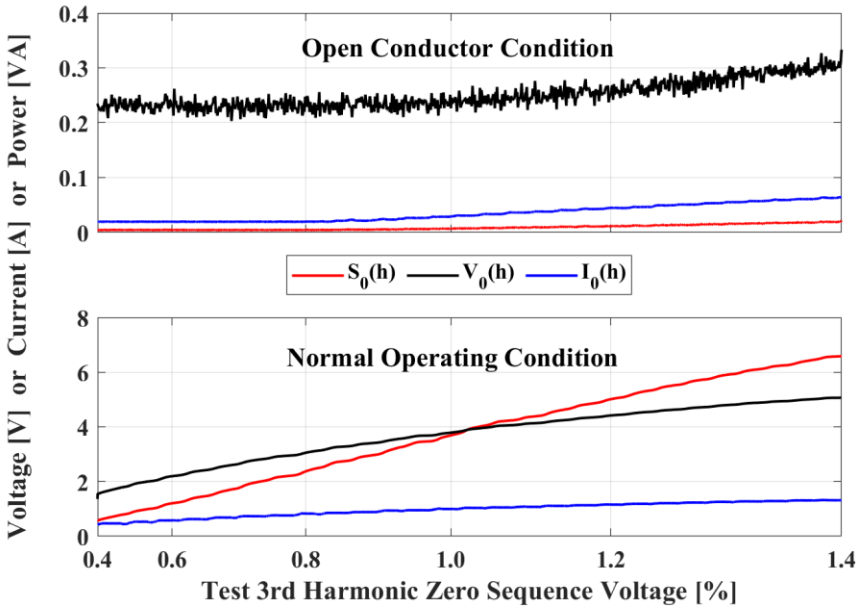

Figure 4.31 Performances of detection indices for different 3rd harmonic voltages

It can be seen in Figure 4.31 that, as the test voltage changes, the power index is constantly the lowest under the open conductor condition. By contrast, the power index and the voltage index are comparable under the normal operating condition. The power index outperforms the voltage index when the test voltage is high.

Based on the above sensitivity studies, one can conclude that the power index has a better performance than the other two indices. Therefore, the power-based criterion is to be preferred for use in detecting the open conductor condition.

4.3.4.4 The Usefulness of Power-Frequency Zero Sequence Component

One may wonder if the zero sequence component at power frequency can also be used for detection. The behaviours of the power-frequency zero sequence power in an experiment (the same one presented in the experiment verification) are shown in Figure 4.32.

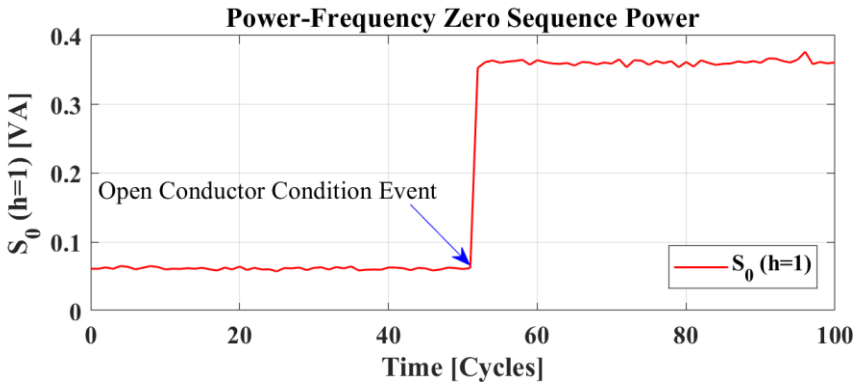

Figure 4.32 Performance of $\boldsymbol{S_0(h=1)}$ under both operating conditions

As can be seen, $S_0(h=1)$ is not zero after the open conductor occurs. This is because, under the open conductor condition, the voltages on the two normal phases generate a transformer exciting current, flowing into the ground through the transformer neutral [98]. This current is in zero sequence. Due to the system voltage at power frequency being large, the associated zero sequence current and voltage (i.e., $I_0(h=1)$ and $V_0(h=1)$) at the transformer terminal are both not zero. Therefore, the proposed scheme cannot employ the power-frequency zero sequence component.

4.3.4.5 Immunity to Other Disturbances

There are power disturbances other than the 3rd harmonics existing in power systems. These disturbances may also generate 3rd harmonic zero sequence voltage and current responses at the transformer terminal. Thus, their influence needs to be considered. Disturbances are manually created in the experiments to investigate the impacts of power disturbances on the proposed criteria.

1) Motor Starting

Motors are connected to the main bus in power plants, and motor starting may generate power disturbances on the main bus. Accordingly, the influence of motor starting on the proposed method

is investigated. Two identical motor starting events are applied under the normal operating condition and the open conductor condition, respectively. The power index with the influence of motor starting is shown in Figure 4.33. The purpose of Figure 4.34 is to confirm the motor starting events by showing the motor's 3rd harmonic current. These 3rd harmonics are very low during the motor's steady-state operation and are caused by non-ideal sinusoidal voltages applied to the aging motor.

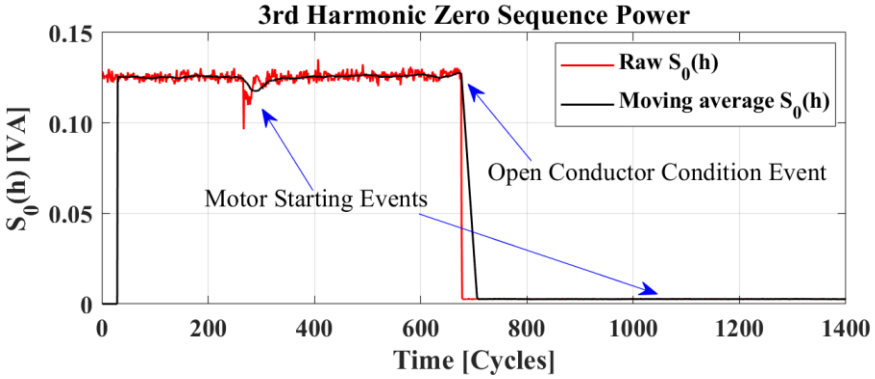

Figure 4.33 Power index with the influence of motor starting

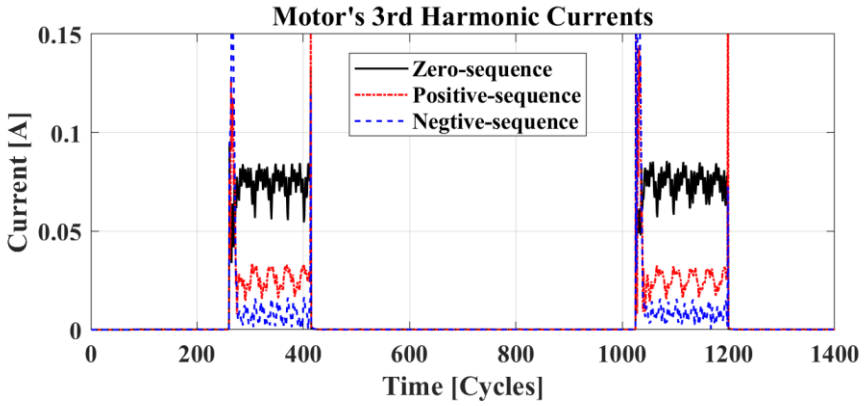

Figure 4.34 Motor's 3rd harmonic currents

One can see from Figure 4.33 and Figure 4.34 that motor starting generates some power disturbances on the main bus that affect the raw 3rd harmonic power (i.e., raw $S_0(h)$), however, the power index used for the detection (i.e., moving average $S_0(h)$) is much less affected. Thus, motor starting has little influence on the proposed method.

2) Capacitor Switching

A 16.67μF three-phase capacitor bank is connected to the main bus. Two identical capacitor switching events are applied under the normal operating condition and the open conductor condition, respectively. The power index with the influence of capacitor switching is shown in Figure 4.35. The events are confirmed by the capacitor injecting currents in Figure 4.36.

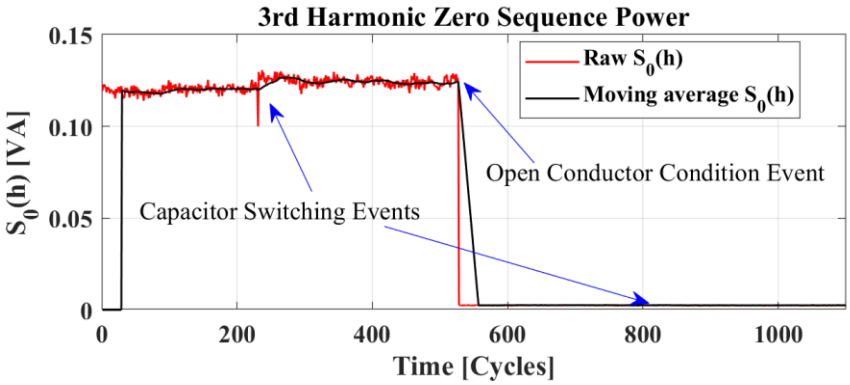

Figure 4.35 Power index with the influence of capacitor switching

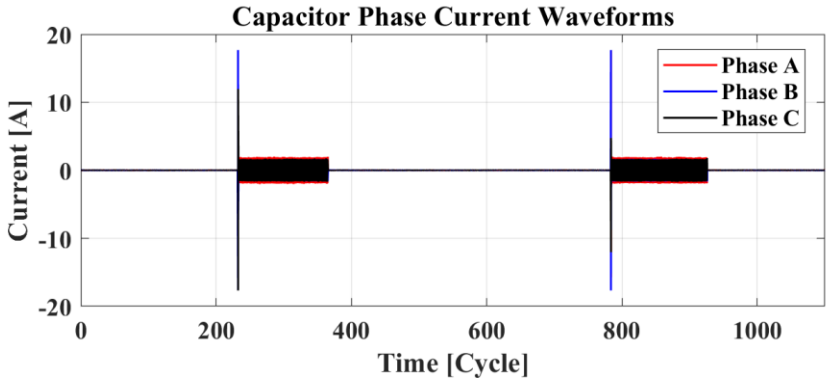

Figure 4.36 Capacitor's three-phase current waveforms

3) Harmonic Load Change

Two identical harmonic load change events are applied under the normal operating condition and the open conductor condition, respectively. The power index is shown in Figure 4.37. The events are confirmed by the load's 3rd harmonic zero sequence current injections in Figure 4.38.

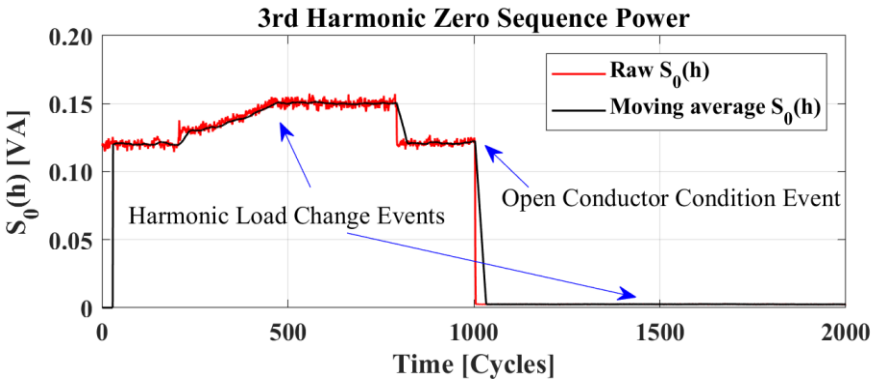

Figure 4.37 Power index with the influence of harmonic load change

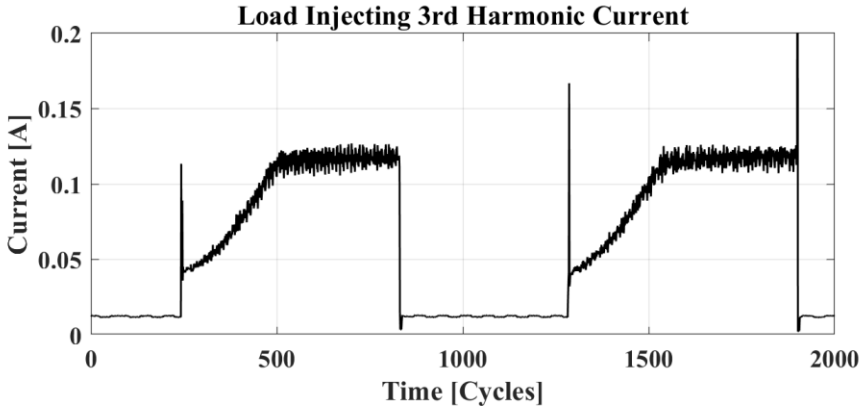

Figure 4.38 Load injecting 3rd harmonic zero sequence current

4) Unbalanced System Voltage Disturbances

The unbalanced system voltage disturbances are also investigated. As a severe and representative unbalanced voltage disturbance, a single-phase voltage interruption is conducted by opening one phase conductor. Note that the testing of this disturbance's influence is meaningful only under the open conductor condition. Figure 4.39 shows that the unbalanced phase voltage abnormality implies the occurrence of a single-phase voltage interruption under the open conductor condition. As shown in Figure 4.40, this disturbance has no noticeable impact on the power index.

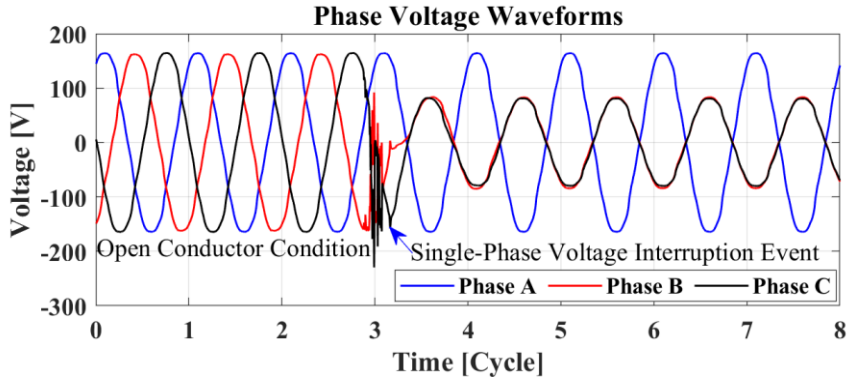

Figure 4.39 Phase voltage waveforms with a single-phase voltage interruption disturbance under the open conductor condition

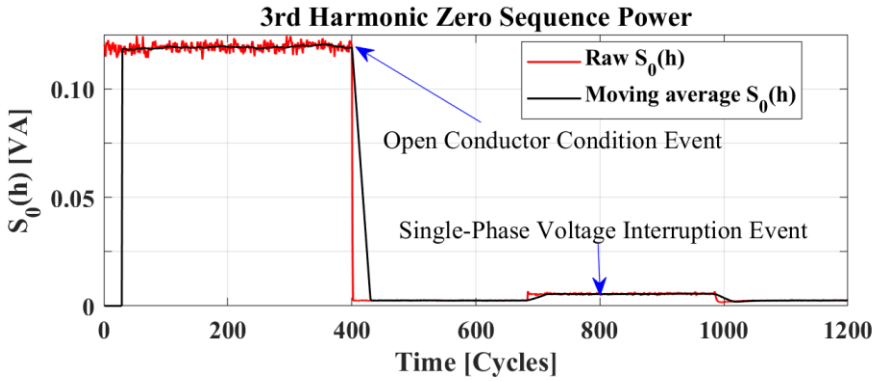

Figure 4.40 Power index with the influence of a single-phase voltage interruption

5) Summary

It can be concluded from the above cases that power disturbances other than the 3rd harmonics do not influence the performance of the proposed criteria for the following reasons. Based on the principle of superposition, one disturbance can be considered as an additional 3rd harmonic excitation to the original 3rd harmonic test voltage. The responses to this additional excitation under both operating conditions have no impact on the detection results.

Specifically, under the open conductor condition, the disturbance-produced 3rd harmonic excitation will not increase detection indices from zero. Thus, the disturbance has no impact under the open conductor condition. On the other hand, under the normal operating condition, one disturbance may yield an increase or decrease in the total 3rd harmonic test voltage. Such a change can be treated as a short-term harmonic fluctuation. Its impact on the detection indices can be removed or

at least much alleviated by the moving average algorithm. Moreover, the decision is made with a time delay, so the disturbance would not have a decisive impact under the normal operating condition. In summary, the proposed criteria are immune to other power disturbances.

4.3.5 Comparative Studies of All the Existing Methods

In this section, the proposed method is compared with three known approaches: the voltage-disturbance-based method presented in the previous section [98], the EPRI's active method [68], and the EPRI's passive method [68].

The voltage-disturbance-based method requires natural voltage disturbances to facilitate detection. So, it cannot detect the open conductor condition immediately. The EPRI's active method requires a 60Hz power source to inject testing currents into the transformer neutral. This method is very difficult to implement, and additional reliability issues exist. Therefore, it is not comparable with the methods based on passive measurements.

The EPRI's passive method uses the measurements of the power-frequency and harmonic components in the transformer neutral current for detection. So, it is a more suitable candidate for comparison. Using the same test condition reported in the experiment verification section, the individual quantities in the transformer neutral before and after the open conductor event are recorded and shown in Figure 4.41.

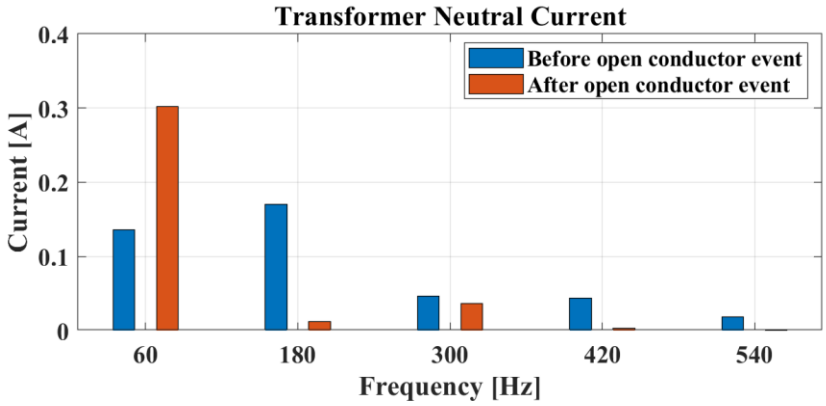

Figure 4.41 Power-frequency and harmonic components in the transformer neutral current before and after the open conductor event

One can see from Figure 4.41 that the 60Hz component and 180Hz component (i.e., 3rd harmonic) in the transformer neutral current are comparable before the open conductor event; after the open conductor occurs, the 60Hz and 180Hz components have an increase of 0.1661A and a decrease of 0.1583A, respectively, and the 300Hz component (i.e., 5th harmonic) has little change. The EPRI's passive method proposes that these current changes could be the signatures of the open conductor, but it does not provide information on which spectrum components to use and what the thresholds are. No theoretical support is provided to explain the change and guide the threshold determination. The threshold in EPRI's passive method is hard to set since the changes are affected significantly by the external system conditions. For example, with a sole focus on the 3rd harmonics, one can observe the 3rd harmonic component changes from 0.1706A to 0.0123A due to the open conductor. However, it is hard to determine a threshold in advance to differentiate those two values (i.e., two operating conditions). In fact, the EPRI's passive method is not proposed to work independently; instead, it works together with the EPRI's active method.

In summary, the proposed method has better performance, and the detection criterion is established based on a scientific understanding of the phenomenon to be detected.

4.3.6 Implementation

Implementation issues, including the hardware deployment and the detection algorithm, are presented in this section to develop the power-based criterion into a practical scheme. The results of a representative experimental case prove the feasibility and effectiveness of the proposed scheme.

4.3.6.1 Hardware Implementation

The proposed method can be implemented as a new type of relay shown in Figure 4.42. The digital relay takes the analog zero sequence voltage and current inputs, implements the Discrete Fourier transform (DFT) algorithm to extract the 3rd harmonic zero sequence voltage and current from the analog inputs, and uses the extracted 3rd harmonics to perform the open conductor detection. The relay's input and logic processing functions are similar to the well-known zero sequence power

relays [99]. In this scheme, all the measurement data are collected and processed at one location. As a result, a communication network for data transmission is not needed.

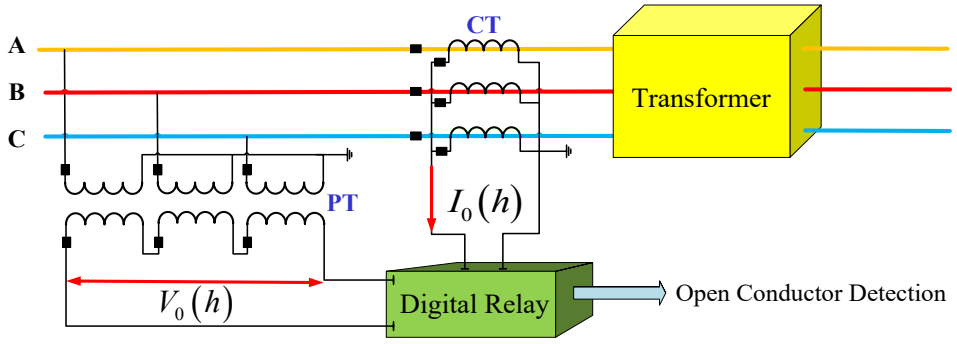

Figure 4.42 Hardware deployment schematic diagram

One unique feature of the proposed relaying scheme is that the threshold is adaptive in comparison with conventional relays. To achieve this goal, the new relay needs to store the one-day monitoring information and update the setting. The data storage unit can be built into the relay. The setting strategy has been explained in detail in section 4.3.3.

4.3.6.2 Detection Algorithm

The detection algorithm is shown in the flowchart of Figure 4.43 and is explained in the following. In the initialization, a daily profile of the 3rd harmonic zero sequence voltage is obtained at the transformer terminal. The downstream 3rd harmonic zero sequence impedance is determined as the ratio of 3rd harmonic zero sequence voltage and current. Thus, the threshold $\varepsilon_S(h)$ is set, and the proposed scheme starts to work. The relay synchronously digitizes the analog zero sequence current and voltage signals obtained via CTs and PTs at the transformer terminal. Then, the relay implements the DFT algorithm on the sampled data to extract the 3rd harmonic zero sequence voltage and current in phasors and calculates a raw power index per cycle. Next, the power indices for decision-making are generated by adopting the moving average algorithm on the raw indices. The window length of the moving average algorithm is set as 30 cycles. If the criterion (4.20) is being satisfied (i.e., power indices are always greater than the setting) throughout 1s, the open conductor condition is detected. Otherwise, the operating condition is considered to be normal. It

is also worth noting that the relay's output of detecting an open conductor condition may or may not yield immediate tripping.

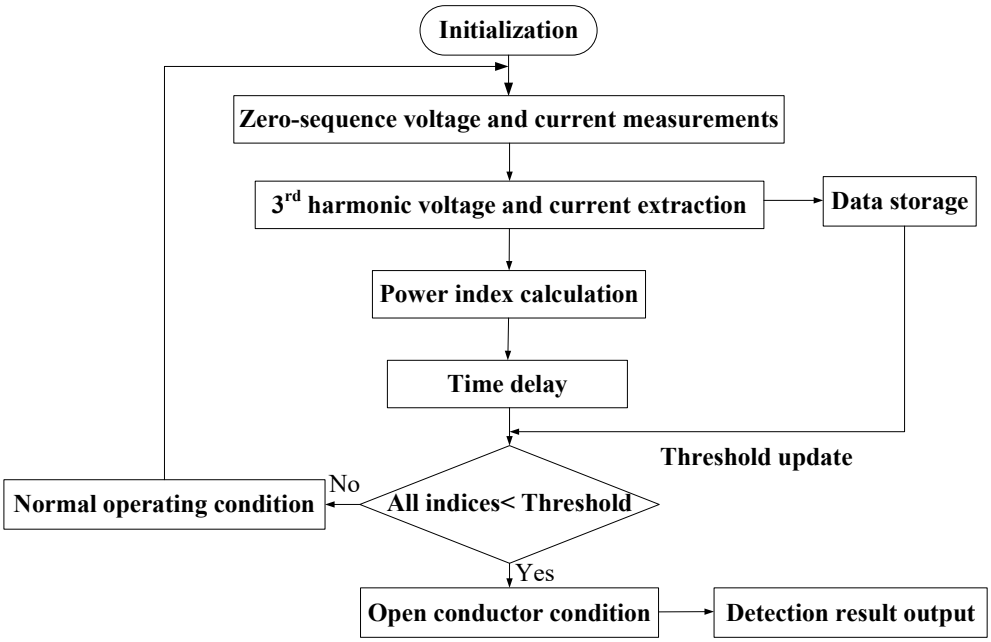

Figure 4.43 Algorithm flowchart

4.3.6.3 Case Study Results

This section presents an experimental case with the complete detection procedure to demonstrate how the proposed scheme works.

In the initialization, a daily profile of the 3rd harmonic zero sequence voltage at the transformer terminal (see Figure 4.44) is obtained. The minimum value in this profile is 0.49V. Also, 3rd harmonic zero sequence impedance downstream from the transformer terminal is calculated as 5**Ω**, as shown in Figure 4.45. Thus, the threshold $\varepsilon_S(h)$ is determined as 0.048VA.

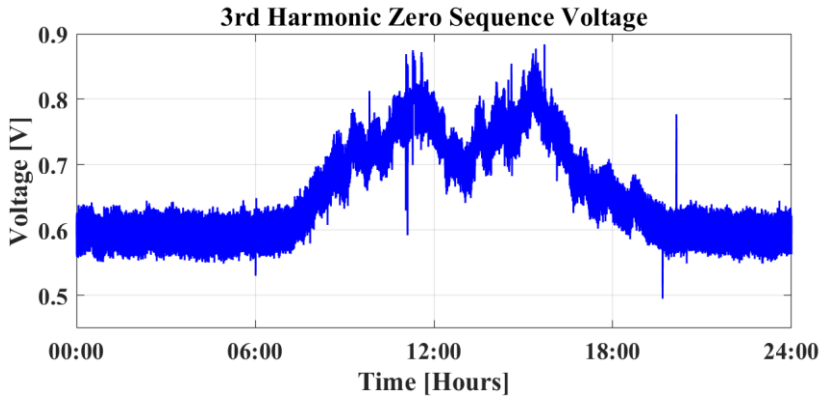

Figure 4.44 Daily profile of 3rd harmonic zero sequence voltage at the transformer terminal

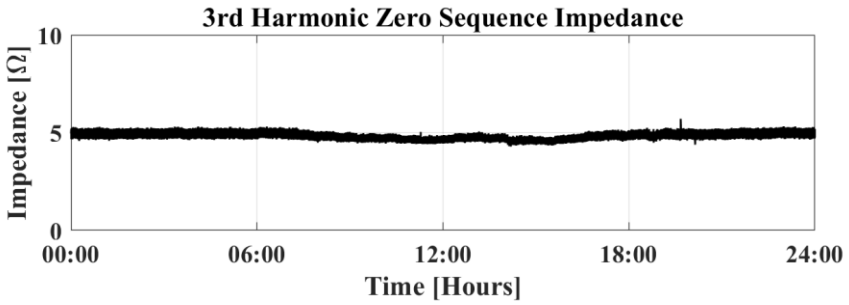

Figure 4.45 3rd harmonic zero sequence impedance downstream from the transformer terminal

Once the threshold is set, the proposed scheme starts to detect the open conductor condition. The continuously monitored power index for the entire second day is shown in Figure 4.46. It can be seen that all the indices are above the threshold, which indicates that the operating condition is normal.

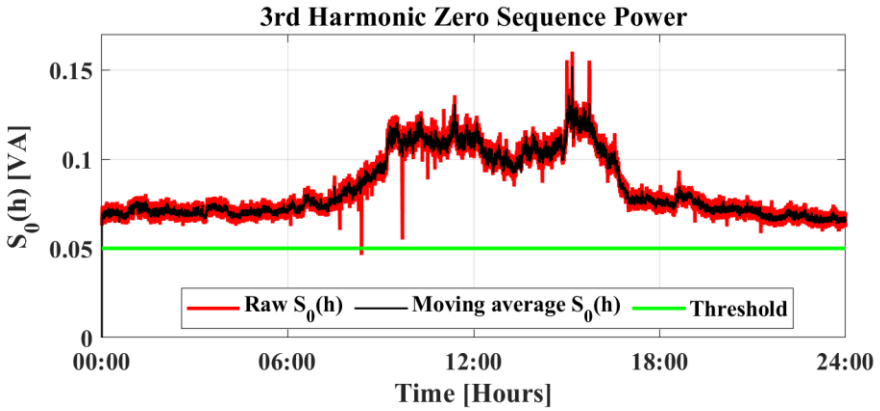

Figure 4.46 One-day performance of the power index under the normal operating condition

At the end of the day, based on the information of the daily voltage profile and impedance $Z_0(h)$, the threshold $\varepsilon_S(h)$ is updated as 0.046VA. On the next day, when an open conductor occurs, the daily and three-second behaviours of the power index are shown in Figure 4.47 and Figure 4.48, respectively.

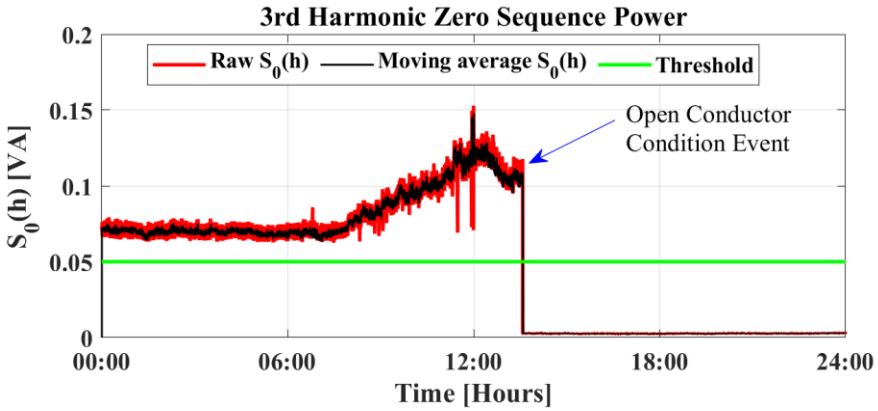

Figure 4.47 One-day performance of power index with an open conductor condition occurrence

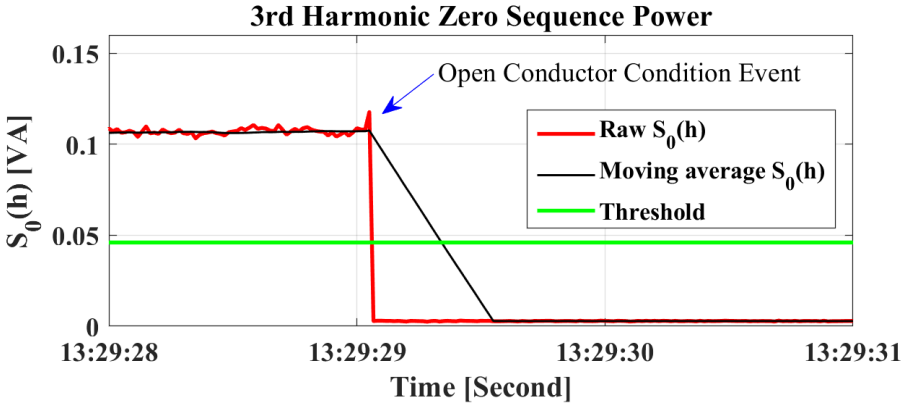

Figure 4.48 Three-second performance of power index at the occurrence of an open conductor condition

One can see from Figure 4.48 that the power index drops at the instant of the open conductor condition event, starts to satisfy the detection criterion of (4.20) in 0.3s, and stays below the threshold for the next 1s. Therefore, the open conductor condition is quickly detected.

4.3.7 Summary

An advanced method is proposed for open conductor detection in the above sections. The key idea of the method is to use the 3rd harmonic zero sequence power. The method's good performance is

proved using extensive simulation and experimental studies. The proposed method can be easily implemented using a relay similar to the conventional zero sequence power relay but with a function of adaptive setting. Extensive study results show that the proposed method is a promising technique to solve the open conductor detection problem.

4.4 Conclusion

An undetected open conductor condition is a threat to the safe operation of power plants and industrial facilities. This condition is especially challenging to detect in a system with certain unloaded Y_g connected primary transformers. Few approaches have been proposed to date to solve this problem effectively. This is due to the lack of detectable abnormal voltage and current changes when a conductor opens. This research recognizes that this situation is related to the positive sequence nature of the supply voltage. If the supply voltage were in zero sequence, an open conductor would produce different voltage and current responses. Based on this understanding, two natural power-disturbance-based condition monitoring methods are proposed in this chapter. The first method jointly analyzes the unbalanced voltage disturbance and the resultant response of the transformer neutral current to achieve the open conductor detection. The second method uses the 3rd harmonic zero sequence power for the open conductor detection. Good performances of both methods have been proved using extensive simulation and experimental studies. The implementation and practical considerations of both methods have been discussed. Comparative studies of all the existing techniques further verify that the proposed 3rd harmonic power based method is the most promising, having the advantages of fast detection and easy implementation. Since the proposed two methods deploy different types of natural power disturbances, they can work individually or in a parallel way to increase the effectiveness and reliability of the open conductor detection.

Chapter 5: Conclusions and Future Work

This chapter summarizes the findings and contributions of the thesis and provides suggestions for future work.

5.1 Thesis Conclusions and Contributions

The Ph.D. research aims to transform active condition monitoring from offline to online using natural power disturbances as the test signals. Such a power-disturbance-based condition monitoring approach proposed in this thesis can provide a much more accurate picture of conditions for different power equipment with no need for a scheduled de-energization. As a result, it can strongly support and even direct the emerging condition-based operation actions and asset management in an efficient and low-cost manner. It can also significantly increase the resiliency and reliability of power systems by avoiding unexpected equipment failures. In this thesis, the proposed concept has been successfully applied for two topics: substation grounding grid condition monitoring and open conductor detection. The main conclusions and contributions of this thesis are summarized as follows.

- Chapter 2 presents an online method for monitoring the substation grounding impedance and the grounding grid conditions. The proposed method uses naturally occurring fault currents as the test current. The corresponding GPR is measured using an isolated multi-grounded neutral. The current and potential loops are installed permanently. Over time, the statistical trend of the grounding impedances estimated using the proposed method can provide a more detailed picture of grounding grid conditions than an occasional single test result obtained using offline methods. The main challenges faced by the proposed method are multiple interferences that can cause measurement inaccuracy. The main factors affecting such interference-caused errors are identified through analytical studies. Various ways to mitigate the impacts of those interferences are identified. Based on the extensive verification and sensitivity study results using industrial data, a guide for the selection of the feeder neutral for the GPR measurement and the faults as the “test current” sources has been developed. Following the guide and the implementation requirements suggested, good measurement accuracy can be achieved. Furthermore, estimated ranges of measurement errors due to different interference issues are

provided to give users additional confidence in the results. An application study demonstrates that the trend of impedance variation is a more useful indicator of the substation grounding grid conditions.

- Chapter 3 proposes an improved method for substation grounding grid condition monitoring. The proposed method uses a novel multiwire technique for the GPR measurement. Using the naturally existing 3rd harmonic current as test signals and the resultant GPR, the method can estimate the substation grounding grid impedance at 60Hz at short time intervals and track the impedance estimations over time to reveal the substation grounding grid conditions. It is easy to implement the proposed method, with current measurements in the substation and the GPR measurement using three measuring wires permanently installed in a transmission line corridor or on a distribution feeder. Extensive case studies and sensitivity studies show that the proposed method performs well in estimating substation grounding grid impedances. The method is negligibly affected by the GPR measuring wires' horizontal displacement in the transmission line corridor and their vertical displacement on the feeder pole. Also, it has no specific requirements for transmission lines, feeders, and 3rd harmonic sources such as three-phase current spectra, locations, and grounding resistances. Due to the advantages of the significant reduction of inductive and soil potential interferences, the proposed method is applicable for transmission and distribution substations that may contain grounding grids of different sizes and power transformers of all possible winding connections. Application studies demonstrate that the proposed method can timely and reliably reveal the deterioration of substation grounding grid conditions.

- Two power-disturbance-based condition monitoring schemes in different working mechanisms are proposed in Chapter 4 to address the open conductor condition detection challenge encountered in power plants. The first scheme jointly analyzes the natural unbalanced voltage disturbance and the resultant response of the transformer neutral current to achieve the open conductor detection. The second scheme deploys the 3rd harmonic zero sequence power for the open conductor detection. Both methods' good performance and effectiveness have been demonstrated using simulation and experimental studies. Implementation and practical considerations are addressed. Comparative studies of all the existing techniques further show that the proposed 3rd harmonic power based method is the most promising with the advantages

of fast detection and easy implementation. Since these two schemes deploy different types of natural power disturbances, they can work individually or in a parallel way to increase the effectiveness and reliability of the detection.

5.2 Suggestions for Future Work

In this thesis, several power-disturbance-based condition monitoring techniques have been successfully developed to solve the challenges of substation grounding grid condition monitoring and open conductor detection. Some extensions of research related to these two topics are as follows:

1. Grounding condition monitoring for large-scale solar farms.

2. Grounding condition monitoring for portable grounding devices used for worksite safety in power line maintenance.

3. Grounding condition monitoring for High Voltage Direct Current (HVDC) systems.

Besides the focused research topics in the thesis, the proposed power-disturbance-based condition monitoring approach can be extended to other power equipment for different condition monitoring focuses, such as power transformer winding deformation and power cable sheath misconnection.

References

[1] A. Silverstein, "The NASPI technical report: Diagnosing equipment health and mis-operations with PMU data," [Online]. Available: http://www.naspi.org.

[2] Siemens Energy, Integrated Substation Condition Monitoring. Online [Available]: https://assets.siemens-energy.com/siemens/assets/api/uuid:6418467a-39c9-4415-bf40-ad45a48f37a3/se-ff-en-iscm-1.pdf.

[3] W. Zhang, X. Xiao, K. Zhou, W. Xu *et al.*, "Multicycle incipient fault detection and location for medium voltage underground cable," *IEEE Transactions on Power Delivery,* vol. 32, no. 3, pp. 1450-1459, Jun. 2017.

[4] S. Kulkarni, S. Santoso, and T. A. Short, "Incipient fault location algorithm for underground cables," *IEEE Transactions on Smart Grid,* vol. 5, no. 3, pp. 1165-1174, May 2014.

[5] W. Xu, Z. Huang, X. Xie, and C. Li, "Synchronized waveforms – A frontier of data-based power system and apparatus monitoring, protection, and control," *IEEE Transactions on Power Delivery,* vol. 37, no. 1, pp. 3-17, Feb. 2022.

[6] *IEEE Guide for Field Testing and Evaluation of the Insulation of Shielded Power Cable Systems Rated 5 kV and Above*, 2012.

[7] *IEEE Guide for Field Testing of Shielded Power Cable Systems Using Very Low Frequency (VLF)(less than 1 Hz)*, IEEE Standard 400.2, 2013.

[8] *IEEE Guide for the Application and Interpretation of Frequency Response Analysis for Oil-Immersed Transformers*, IEEE Standard C57.149, 2012.

[9] P. Mukherjee and S. K. Panda, "Diagnosing disk-space variation in transformer windings using high-frequency inductance measurement," *IEEE Transactions on Power Delivery,* Early Access, 2022.

[10] W. Zhou, Y. Liu, G. Li, G. Yan *et al.*, "Power frequency interference and suppression in measurement of power transmission tower grounding resistance," *IEEE Transactions on Power Delivery,* vol. 30, no. 2, pp. 1016-1023, Apr. 2015.

[11] H. Soliman, H. Wang, and F. Blaabjerg, "A review of the condition monitoring of capacitors in power electronic converters," *IEEE Transactions on Industry Applications,* vol. 52, no. 6, pp. 4976-4989, 2016.

[12] L. Zhang, H. Chen, Q. Wang, N. Nayak *et al.*, "A novel on-line substation instrument transformer health monitoring system using synchrophasor data," *IEEE Transactions on Power Delivery,* vol. 34, no. 4, pp. 1451-1459, Aug. 2019.

[13] H. G. Sarmiento and E. Estrada, "A voltage sag study in an industry with adjustable speed drives," *IEEE Industry Applications Magazine,* vol. 2, no. 1, pp. 16-19, Jan./Feb. 1996.

[14] L. Zhan, Y. Liu, W. Yao, J. Zhao *et al.*, "Utilization of chip-scale atomic clock for synchrophasor measurements," *IEEE Transactions on Power Delivery,* vol. 31, no. 5, pp. 2299-2300, Oct. 2016.

[15] F. V. Lopes, T. R. Honorato, G. A. Cunha, and N. S. S. Ribeiro, "Transmission line records synchronization based on traveling waves analysis," *IEEE Transactions on Power Delivery,* vol. 36, no. 3, pp. 1892-1902, Jun. 2021.

[16] *IEEE Standard for a Precision Clock Synchronization Protocol for Networked Measurement and Control Systems*, IEEE Standard 1588, 2008.

[17] *IEEE Standard Profile for Use of IEEE 1588™ Precision Time Protocol in Power System Applications*, IEEE Standard C37.238, 2017.

[18] *IEEE Guide for Designing a Time Synchronization System for Power Substations*, IEEE Standard 2030.101-2018.
[19] *IEEE Recommended Practice for Implementing an IEC 61850-Based Substation Communications, Protection, Monitoring, and Control System*, IEEE Standard 2030.100, 2017.
[20] *IEEE Standard for Synchrophasor Measurements for Power Systems*, IEEE Standard C37.118.1, 2011.
[21] Siemens Energy, Siemens Assetguard MVC. Online [Available]: https://assets.new.siemens.com/siemens/assets/api/uuid:58b7b249-5562-4ec3-9974-6f737373bf13/energy-ip-assetguard-mineralsweek-jtello.pdf.
[22] *IEEE Guide for Safety in AC Substation Grounding*, IEEE Standard 80, 2013.
[23] *IEEE Guide for Measuring Earth Resistivity, Ground Impedance, and Earth Surface Potentials of a Grounding System*, IEEE Standard 81, 2012.
[24] A. P. S. Meliopoulos, G. Cokkinides, and H. Abdallah, "A PC based ground impedance measurement instrument," *IEEE Transactions on Power Delivery* vol. 8, no. 3, pp. 1095-1106, July 1993.
[25] M. Kazerooni, H. Zhu, and T. J. Overbye, "Improved modeling of geomagnetically induced currents utilizing derivation techniques for substation grounding resistance," *IEEE Transactions on Power Delivery,* vol. 32, no. 5, pp. 2320-2328, Oct. 2017.
[26] A. P. S. Meliopoulos, S. G. Patel, and G. J. Cokkinides, "A new method and instrument for touch and step voltage measurements," *IEEE Transactions on Power Delivery,* vol. 9, no. 4, pp. 1850-1860, Oct. 1994.
[27] X. Long, M. Dong, W. Xu, and Y. W. Li, "Online monitoring of substation grounding grid conditions using touch and step voltage sensors," *IEEE Transactions on Smart Grid,* vol. 3, no. 2, pp. 761-769, Jun. 2012.
[28] B. Zhang, Z. Zhao, X. Cui, and L. Li, "Diagnosis of breaks in substation's grounding grid by using the electromagnetic method," *IEEE Transactions on Magnetics,* vol. 38, no. 2, pp. 473-476, Mar. 2002.
[29] C. Yu, Z. Fu, Q. Wang, H. M. Tai *et al.*, "A novel method for fault diagnosis of grounding grids," *IEEE Transactions on Industry Applications,* vol. 51, no. 6, pp. 5182-5188, Nov./Dec. 2015.
[30] C. E. F. Caetano, J. O. S. Paulino, C. F. Barbosa, J. C. de Oliveira e Silva *et al.*, "A new method for grounding resistance measurement based on the drained net charge," *IEEE Transactions on Power Delivery,* vol. 34, no. 3, pp. 1011-1018, Jun. 2019.
[31] F. P. Zupa and J. F. Laidig, "A practical ground potential rise prediction technique for power stations," *IEEE Transactions on Power Apparatus and Systems,* vol. PAS-99, no. 1, pp. 207-216, Jan./Feb. 1980.
[32] I. D. Lu and R. M. Shier, "Application of a digital signal analyzer to the measurement of power system ground impedances," *IEEE Transactions on Power Apparatus and Systems,* vol. PAS-100, no. 4, pp. 1918-1922, Apr. 1981.
[33] H. G. Sarmiento, J. Fortin, and D. Mukhedkar, "Substation ground impedance: Comparative field measurements with high and low current injection methods," *IEEE Transactions on Power Apparatus and Systems,* vol. PAS-103, no. 7, Jul. 1984.
[34] S. G. Patel, "A complete field analysis of substation ground grid by applying continuous low voltage fault," *IEEE Transactions on Power Apparatus and Systems,* vol. PAS-104, no. 8, pp. 2238–2243, Aug. 1985.

[35] J. Fortin, H. G. Sarmiento, and D. Mukhedkar, "Field measurement of ground fault current distribution and substation ground impedance at LG-2, Québec," *IEEE Transactions on Power Delivery,* vol. 1, no. 3, pp. 48-60, Jul. 1986.
[36] S. T. Sobral, C. A. Peixoto, D. Fernandes, and D. Mukhedkar, "Grounding measurements at the Itaipu generating complex using the "extended eleck method"," *IEEE Transactions on Power Delivery,* vol. 3, no. 4, pp. 1553-1563, Oct. 1988.
[37] S. T. Sobral, J. J. Horta Santos, and D. Mukhedkar, "A proposal for ground measurement techniques in substations fed exclusively by power cables," *IEEE Transactions on Power Delivery,* vol. 3, no. 4, pp. 1403-1409, Oct. 1988.
[38] P. R. Pillai and E. P. Dick, "A review on testing and evaluating substation grounding systems," *IEEE Transactions on Power Delivery,* vol. 7, no. 1, pp. 53-61, Jan. 1992.
[39] E. B. Curdts, "Some of the fundamental aspects of grounding resistance measurements," *AIEE Transactions,* vol. 77, pp. 760-767, Nov. 1958.
[40] F. Dawalibi and D. Mukhedkar, "Resistance measurement of large grounding systems," *IEEE Transactions on Power Apparatus and Systems,* vol. PAS-98, no. 6, pp. 2348-2354, Nov./Dec. 1979.
[41] C. Wang, T. Takasima, T. Sakuta, and Y. Tsubota, "Grounding resistance measurement using fall-of-potential method with potential probe located in opposite direction to the current probe," *IEEE Transactions on Power Delivery,* vol. 3, no. 14, pp. 1128-1135, Oct. 1998.
[42] J. Ma and F. P. Dawalibi, "Extended analysis of ground impedance measurement using the fall-of-potential method," *IEEE Transactions on Power Delivery,* vol. 17, no. 4, pp. 881-885, Oct. 2002.
[43] C. Korasli, "Ground resistance measurement with alternative fall-of-potential method," *IEEE Transactions on Power Delivery,* vol. 20, no. 2, pp. 1657-1661, Apr. 2005.
[44] R. Zeng, J. He, and Z. Guan, "Novel measurement system for grounding impedance of substation," *IEEE Transactions on Power Delivery,* vol. 21, no. 2, pp. 719-725, Apr. 2006.
[45] J. K. Choi, Y. H. Ahn, J. W. Woo, G. J. Jung *et al.*, "Evaluation of grounding performance of energized substation by ground current measurement," *Electric Power Systems Research,* vol. 77, pp. 1490-1494, 2007.
[46] T. Yuan, Y. Bai, W. Sima, C. Xian *et al.*, "Grounding resistance measurement method based on the fall of potential curve test near current electrode," *IEEE Transactions on Power Delivery,* vol. 32, no. 4, pp. 2005-2012, Aug. 2017.
[47] Z. Hu, S. Ni, B. Zhang, and K. Zhang, "New method of measuring ground impedance and mutual impedance between measuring lead wires," *IEEE Transactions on Power Delivery,* vol. 33, no. 5, pp. 2070-2077, Mar. 2018.
[48] W. C. Boaventura, I. J. S. Lopes, P. S. A. Rocha, R. M. Coutinho *et al.*, "Testing and evaluating grounding systems of high voltage energized substations: Alternative approaches," *IEEE Transactions on Power Delivery,* vol. 14, no. 3, pp. 923-927, Jul. 1999.
[49] G. Gela, "Condition assessment of substation ground grids phase 1—proof of concept," EPRI, Palo Alto, CA, USA, Rep. 1013910.Mar. 2008.
[50] R. Zeng, J. He, J. Lee, S. Chang *et al.*, "Influence of overhead transmission line on grounding impedance measurement of substation," *IEEE Transactions on Power Delivery,* vol. 20, no. 2, pp. 1219-1225, Apr. 2005.

[51] P. Hrobat and I. Papic, "An oscilloscope method for eliminating the interference and disturbance voltages for the earthing measurements of large earthing systems in substations," *Electric Power Systems Research,* vol. 81, pp. 510-517, 2011.
[52] M. Kuusaari and A. J. Pesonen, "Earth impedance measurements of substations," *CIGRE paper 36-02,* 1978.
[53] Task Force F0A of the IEEE/PES Substations West Coast Subcommittee, "Current north american assessment and refurbishment practices of substation grounding systems," *IEEE Transactions on Power Delivery,* vol. 20, no. 3, pp. 1886-1889, Jul. 2005.
[54] R. J. Gustafson, R. Pursley, and V. D. Albertson, "Seasonal grounding resistance variations on distribution systems," *IEEE Transactions on Power Delivery,* vol. 5, no. 2, pp. 1013-1018, Apr. 1990.
[55] J. He, R. Zeng, Y. Gao, Y. Tu *et al.*, "Seasonal influences on safety of substation grounding system," *IEEE Transactions on Power Delivery,* vol. 18, no. 3, pp. 788-795, Jul. 2003.
[56] Nuclear Regulatory Commission, "NRC information notice 2012-03: Design vulnerability in electric power system," Washington, DC, USA, 2012.
[57] S. Mohajeryami, M. Doostan, and Z. Salami, "An analysis of open-phase fault in power generation station," presented at the North American Power Symposium (NAPS), Denver, Sept., 2016.
[58] International Atomic Energy Agency, "Impact of open phase conditions on electrical power systems of nuclear power plants," Safety Reports Series No.91, 2016.
[59] Electric Power Research Institute, "Distributed energy resources field experence: Open phase," EPRI, Palo Alto, CA, USA, Rep. 3002015949, Apr. 2019.
[60] C. Li and R. Reinmuller, "Open phase detection in der operation by using power quality data analytics," *IEEE Transactions on Power Delivery,* vol. 35, no. 6, pp. 2575-2582, Dec. 2020.
[61] *IEEE Standard for Interconnection and Interoperability of Distributed Energy Resources with Associated Electric Power Systems Interfaces*, IEEE Standard 1547, 2018.
[62] A. Norouzi, "Open phase conditions in transformers analysis and protection algorithm," presented at the 66th Annual Conference for Protective Relay Engineers, College Station, TX, USA, Apr., 2013.
[63] V. H. Makwana and B. R. Bhalja, "A new digital distance relaying scheme for series-compensated double-circuit line during open conductor and ground fault," *IEEE Transactions on Power Delivery,* vol. 27, no. 2, pp. 910-917, Apr. 2012.
[64] B. Wang, X. Dong, Z. Bo, and A. Klimek, "Negative-sequence pilot protection with applications in open-phase transmission lines," *IEEE Transactions on Power Delivery,* vol. 25, no. 3, pp. 1306-1313, Jul. 2010.
[65] A. C. Westrom, A. P. S. Meliopoulos, G. J. Cokkinides, and A. H. Ayoub, "Open conductor detector system," *IEEE Transactions on Power Delivery,* vol. 7, no. 3, pp. 1643-1651, Jul. 1992.
[66] J. Blake, A. Rose, A. Baker, E. Hadley *et al.*, "Open phase detection for power transformers using VT triggered optical CTs and IEC 61850-9.2LE compliant relays," presented at the 70th Annual Conference for Protective Relay Engineers (CPRE), College Station, TX, USA, Apr., 2017.
[67] W. Johnson, "Nuclear maintenance application center: Development and analysis of an open-phase detection scheme for various configurations of auxiliary transformers," EPRI, Palo Alto, CA, USA, Rep. 3002000764, May 2013.

[68] W. Johnson, "Interim report: EPRI open-phase detection method," EPRI, Palo Alto, CA, USA, Rep. 3002004432, Oct. 2014.
[69] J. J. Burke and D. J. Lawrence, "Characteristics of fault currents on distribution systems," *IEEE Transactions on Power Apparatus and Systems,* vol. PAS-103, no. 1, pp. 1-6, Jan. 1984.
[70] A. Sundaram, "Distribution fault location: Field data and analysis," EPRI, Palo Alto, CA, 1012438, 2006.
[71] H. W. Dommel, *EMTP theory book. 2nd Edition*. Vancouver, Canada: Microtran Power System Analysis Corporation, 1992.
[72] E. J. Rogers and J. F. White, "Mutual coupling between finite lengths parallel or angled horizontal earth return conductors," *IEEE Transactions on Power Delivery,* vol. 4, no. 1, pp. 103-111, Jan. 1989.
[73] *National Electrical Safety Code (NESC)*, Accredited Standards Committee C2, 2012.
[74] *IEEE Recommended Practice for Grounding of Industrial and Commercial Power Systems*, IEEE Standard 142, 2007.
[75] T. A. Short, *Electric Power Distribution Handbook*, 2nd *Edition*. Boca Raton: CRC Press, 2014.
[76] J. L. Pinto de Sa and M. Louro, "On human life risk-assessment and sensitive ground fault protection in mv distribution networks," *IEEE Transactions on Power Delivery,* vol. 25, no. 4, pp. 2319-2327, Oct. 2010.
[77] Ecole Polytechnique Federale de Lausanne (EPFL), "Monitoring Data Accessed on October 1, 2015", [Online]. Available: http://smartgrid.epfl.ch/?q=monitoring.
[78] M. Brown, M. Biswal, S. Brahma, S. J. Ranade *et al.*, "Characterizing and quantifying noise in PMU data," *IEEE PES General Meeting*, Boston, MA, USA, pp. 1-5, 2016.
[79] Texas Instruments, "Multi-phase power quality measurement with isolate shunt sensors", [Online]. Available: https://www.ti.com/lit/ug/tidubo7a/tidubo7a.pdf?ts=1645129022133&ref_url=https%253A%252F%252Fwww.startpage.com%252F.
[80] A. E. Emanuel, J. A. Orr, D. Cyganski, and E. M. Gulachenski, "A survey of harmonic voltages and currents at distribution substations," *IEEE Transactions on Power Delivery,* vol. 6, no. 4, pp. 1883-1890, Oct. 1991.
[81] Y. Wang, J. Yong, Y. Sun, W. Xu *et al.*, "Characteristics of harmonic distortions in residential distribution systems," *IEEE Transactions on Power Delivery,* vol. 32, no. 3, pp. 1495-1504, Jun. 2017.
[82] A. E. Emanuel, J. A. Orr, D. Cyganski, and E. M. Gulachenski, "A survey of harmonic voltages and currents at the customer's bus," *IEEE Transactions on Power Delivery,* vol. 8, no. 1, pp. 411-421, Jan. 1993.
[83] T. C. Shuter, H. T. Vollkommer, and T. L. Kirkpatrick, "Survey of harmonic levels on the american electric power distribution system," *IEEE Transactions on Power Delivery,* vol. 4, no. 4, pp. 2204-2213, Oct. 1989.
[84] A. D. Papalexopoulos and A. P. Meliopoulos, "Frequency dependent characteristics of grounding systems," *IEEE Transactions on Power Delivery,* vol. PWRD-2, no. 4, pp. 1073-1081, Oct. 1987.
[85] L. D. Grcev and M. Heimbach, "Frequency dependent and transient characteristics of substation grounding systems," *IEEE Transactions on Power Delivery,* vol. 12, no. 1, pp. 172-178, Jan. 1997.

[86] T. Ding and W. Xu, "A filtering scheme to reduce the penetration of harmonics into transmission systems," *IEEE Transactions on Power Delivery,* vol. 31, no. 1, pp. 59-66, Jan. 2016.
[87] H. G. Sarmiento, D. Mukhedkar, and V. Ramachandran, "An extension to the study of earth-return mutual coupling effects in ground impedance field measurements," *IEEE Transactions on Power Delivery* vol. 3, no. 1, pp. 96-101, Jan. 1988.
[88] M. Yang, R. Kazemi, S. Jazebi, D. Deswal *et al.*, "Retrofitting the BCTRAN transformer model with nonlinear magnetizing branches for the accurate study of low-frequency deep saturating transients," *IEEE Transactions on Power Delivery,* vol. 33, no. 5, pp. 2344-2353, Oct. 2018.
[89] T. Hong, D. Deswal, and F. De Leon, "An online data-driven technique for the detection of transformer winding deformations," *IEEE Transactions on Power Delivery,* vol. 33, no. 2, pp. 600-609, Apr. 2018.
[90] F. De Leon, A. Farazmand, and P. Joseph, "Comparing the T and π equivalent circuits for the calculation of transformer inrush currents," *IEEE Transactions on Power Delivery,* vol. 27, no. 4, pp. 2390-2398, Aug. 2012.
[91] *IEEE Standard Requirements for Instrument Transformers*, IEEE Standard C57.13, 2008.
[92] A. V. Jouanne and B. Banerjee, "Assessment of voltage unbalance," *IEEE Transactions on Power Delivery,* vol. 16, no. 4, pp. 782-790, Oct. 2001.
[93] V. E. Wagner, A. A. Andreshak, and J. P. Staniak, "Power quality and factory automation," *IEEE Transactions on Industry Applications,* vol. 26, no. 4, pp. 620-626, Jul./Aug. 1990.
[94] D. Sabin, "An assessment of distribution system power quality, volume 2: Statistical summary report," in "EPRI TR-106294," May 1996.
[95] F. W. T. Davenport, "Voltage dips and short interruptions in medium voltage public electricity supply systems," UNIPEDE/DISDIP Report, 1990.
[96] H. E. Mazin, W. Xu, and B. Huang, "Determining the harmonic impacts of multiple harmonic-producing loads," *IEEE Transactions on Power Delivery,* vol. 26, no. 2, pp. 1187-1195, Apr. 2011.
[97] W. M. Grady and S. Santoso, "Understanding power system harnonics," *IEEE Power Engineering Review,* vol. 21, no. 11, pp. 8-11, Nov. 2001.
[98] X. Wang, T. Ding, and W. Xu, "An open conductor condition monitoring scheme using natural voltage and current disturbances," *IEEE Transactions on Power Delivery,* vol. 34, no. 3, pp. 1193-1202, Jun. 2019.
[99] A. R. van C. Warrington, *Protective relays: Their theory and practice volume one. 2nd Edition.* London, UK: Chapman & Hall, 1968.

Appendices

Appendix A: Transfer Voltages from Grounding Electrodes

Mutual coupling always exists between two grounding electrodes in the soil. Its contribution to the soil potential (i.e., the transfer voltage) has distinct characteristics for substation grounding grids and neutral/shield wire rods, mainly depending on their structures. They are analyzed and compared below.

When a current $\bar{I}$ is injected into a grounding rod, the rod's GPR, $\bar{V}_{GPR}^{rod}$, can be calculated as follows:

$$\bar{V}_{GPR}^{rod} = \frac{\rho \bar{I}}{4\pi L_{rod}} \ln \frac{\sqrt{r_{rod}^2 + L_{rod}^2} + L_{rod}}{\sqrt{r_{rod}^2 + L_{rod}^2} - L_{rod}} \tag{A1}$$

where r_{rod} and L_{rod} are the radius and the length of the rod, respectively, and ρ is soil resistivity.

The transfer voltage at a point x meters away from the rod, $\bar{V}_{transfer}^{rod}(x)$, can be calculated as follows:

$$\bar{V}_{transfer}^{rod}(x) = \frac{\rho \bar{I}}{4\pi L_{rod}} \ln\left(\frac{\sqrt{x^2 + L_{rod}^2} + L_{rod}}{\sqrt{x^2 + L_{rod}^2} - L_{rod}}\right) \tag{A2}$$

Thus, the percentage of the transfer voltage over the GPR for a grounding rod at different locations, $\sigma_{rod}(x)$, can be determined in (A3). It is shown in (A3) that this percentage is independent of the soil resistivity and the energized current. The results for typical grounding rods, with a radius of 0.5~1 inch and a length of 8~12 ft, are shown in Figure A1.

$$\sigma_{rod}(x) = \frac{\bar{V}_{transfer}^{rod}(x)}{\bar{V}_{GPR}^{rod}} = \ln\left(\frac{\sqrt{x^2 + L_{rod}^2} + L_{rod}}{\sqrt{x^2 + L_{rod}^2} - L_{rod}} - \frac{\sqrt{r_{rod}^2 + L_{rod}^2} + L_{rod}}{\sqrt{r_{rod}^2 + L_{rod}^2} - L_{rod}}\right) \times 100\% \tag{A3}$$

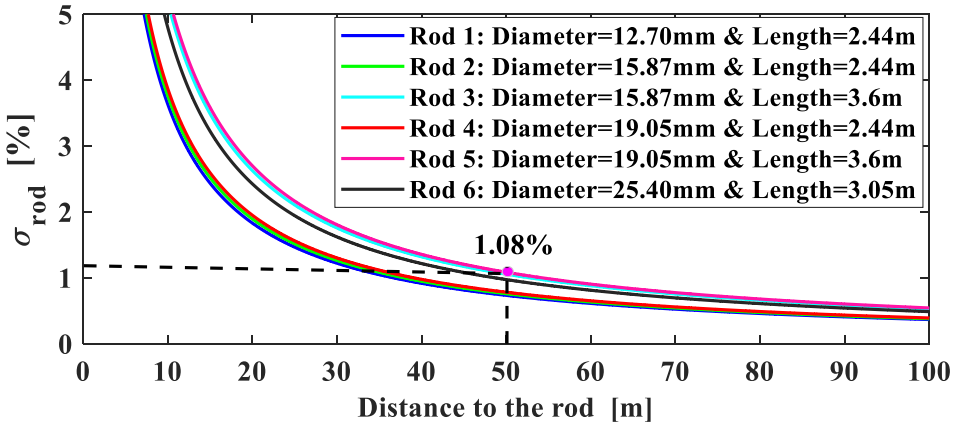

Figure A1 Percentage of the transfer voltage over the GPR for typical grounding rods.

It can be seen from Figure A1 that a regular grounding rod's transfer voltage decays quickly to a negligibly low percentage of the rod's GPR within a short distance. For example, at a 50m distance from the rod, the transfer voltage is only 1.08% of the rod's GPR at most. The larger the distance is, the smaller the transfer voltage will be.

On the other hand, the GPR of a substation grounding grid due to a current $\bar{I}$ injection, $\bar{V}_{GPR}^{grid}$, can be calculated as follows [23]:

$$\bar{V}_{GPR}^{grid} = Z_{grid}\bar{I} \approx \frac{1}{4} \times \sqrt{\frac{\pi}{A}} \times \rho\bar{I} = \frac{\rho\bar{I}}{2D_{grid}} \tag{A4}$$

where A is the size of the grounding grid, and D_{grid} is the diameter of the grounding grid (if assuming that the grid is round).

The transfer voltage at a point x meters away from the grounding grid, $\bar{V}_{transfer}^{grid}(x)$, can be calculated as follows [23]:

$$\bar{V}_{transfer}^{grid}(x) = \frac{\rho\bar{I}}{2\pi x} \tag{A5}$$

Similarly, the percentage of the transfer voltage over the GPR for a substation grounding grid at different locations, $\sigma_{grid}(x)$, can be determined in (A6). This percentage is also independent of the soil resistivity and the energized current.

$$\sigma_{grid}(x) = \frac{\bar{V}_{transfer}^{grid}(x)}{\bar{V}_{GPR}^{grid}} = \frac{D_{grid}}{\pi x} \times 100\% \tag{A6}$$

The results for substation grounding grids in different sizes are shown in Figure A2. The transfer voltage from a grounding grid is not insignificant unless the separated distance is larger than $5\sim10D_{grid}$ (e.g., 500~1000m if the tested grounding grid diameter D_{grid} is 100m).

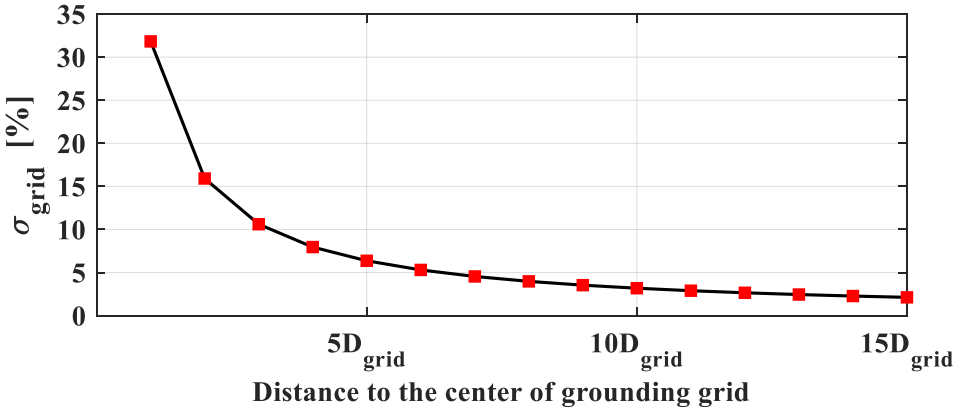

Figure A2 Percentage of the transfer voltage over the GPR for different sizes of grounding grid.

It can be concluded from the above analysis that the zone of influence of a grounding grid is much larger than that of a neutral/shield wire rod.

In an illustrative case, a neutral rod is buried 100m away from the center of a grounding grid. The rod has a diameter of 19.05mm and a length of 3.6m. The grounding grid has a diameter of 100m (i.e., A=7854m^2).

From the substation grounding grid to the grounding rod, the transfer voltage and the mutual impedance are:

$$\bar{V}_{transfer}^{grid} = 1.59\times10^{-3}\rho\bar{I} \quad \text{and} \quad \sigma_{grid} = \frac{\bar{V}_{transfer}^{grid}}{\bar{V}_{GPR}^{grid}} = 15.92\% \tag{A7}$$

$$Z_m^{grid-to-rod} = \frac{\bar{V}_{transfer}^{grid}}{\bar{I}} = 1.59 \times 10^{-3} \rho \tag{A8}$$

From the grounding rod to the substation grounding grid, the transfer voltage and the mutual impedance are:

$$\bar{V}_{transfer}^{rod} = 1.59 \times 10^{-3} \rho \bar{I} \quad \text{and} \quad \sigma_{rod} = \frac{\bar{V}_{transfer}^{rod}}{\bar{V}_{GPR}^{rod}} = 0.54\% \tag{A9}$$

$$Z_m^{rod-to-grid} = \frac{\bar{V}_{transfer}^{rod}}{\bar{I}} = 1.59 \times 10^{-3} \rho \tag{A10}$$

The mutual impedances between the grounding rod and the substation grounding grid are the same as shown in (A8) and (A10). However, the percentage of the transfer voltage from the rod over the GPR is significantly lower (29 times in this case) than that of the substation grounding grid as compared in (A7) and (A9).

Appendix B: Analysis Results for the Implementation Scenario 2 in Feeders of the Multiwire Technique

In the network of a typical multi-grounded neutral shown in Figure B1, the currents are generated by two power sources at 3rd harmonics, i.e., the voltage $\bar{e}$ on each neutral span induced from the phase currents on the feeder and the equivalent current injection $\bar{I}_S$ at the substation grounding grid from all 3rd harmonic sources in the system. The current distributions on neutral wires and grounding rods for a realistic case are achieved from simulations and shown in Table B1, where the subscript "k" in the variables $\bar{I}_{nk}$ and $\bar{I}_{gk}$ represents the kth segment of the neutral.

This study case contains eight feeders. Since comparative relations rather than absolute values of the neutral currents are used to show their inequality among adjacent spans, assume that the equivalent current $\bar{I}_S$ injection into the grounding grid from all the feeders is $1\angle 0°$ p.u. The focused feeder has a 3rd harmonic current of $1/8\angle 0°$ p.u. in three phases flowing to the substation grounding grid from a load at the far end. The total impedance of the substation grounding grid in parallel with neutrals of all feeders except the one under analysis is denoted as $Z_{SubG} = 0.15\Omega$. The neutral is 6km with a span length of $L = 0.1km$. At the 3rd harmonics, the self-impedance of the neutral wire is $Z_s = 0.91 + j2.84\Omega/km$ and the mutual impedance to each phase conductor is $Z_m = 0.0058 + j1.42\Omega/km$. The neutral grounding rod resistance is $R_g = 15\Omega$.

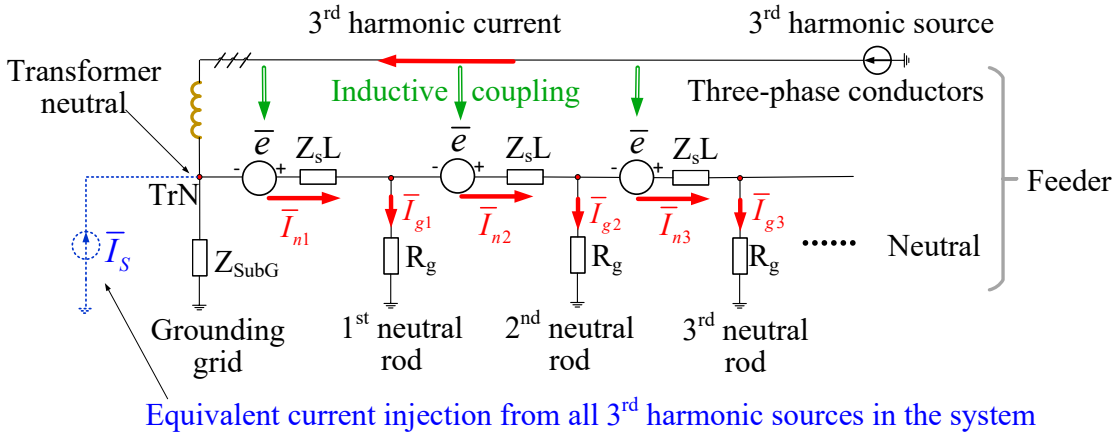

Figure B1 Network of the multi-grounded neutral with inductive interference and current injection

Table B1 Current distributions on the first three neutral segments for a realistic case

	1st segment	2nd segment	3rd segment
Neutral wire current (Unit: p.u.)	$\bar{I}_{n1}$=0.1065∠168.8°	$\bar{I}_{n2}$=0.0986∠168.1°	$\bar{I}_{n3}$=0.0915∠167.9°
Neutral rod current (Unit: p.u.)	$\bar{I}_{g1}$=0.0080∠176.6°	$\bar{I}_{g2}$=0.0071∠171.8°	$\bar{I}_{g3}$=0.0064∠167.0°
Ratio of $\lvert\bar{I}_{nk}/\bar{I}_{n1}\rvert$	$\lvert\bar{I}_{n1}/\bar{I}_{n1}\rvert$=100%	$\lvert\bar{I}_{n2}/\bar{I}_{n1}\rvert$=92.57%	$\lvert\bar{I}_{n3}/\bar{I}_{n1}\rvert$=85.90%
Ratio of $\lvert\bar{I}_{gk}/\bar{I}_{nk}\rvert$	$\lvert\bar{I}_{g1}/\bar{I}_{n1}\rvert$=7.5028%	$\lvert\bar{I}_{g2}/\bar{I}_{n2}\rvert$=7.2273%	$\lvert\bar{I}_{g3}/\bar{I}_{n3}\rvert$=6.9450%

It can be found from Table B1 that the neutral wire current on the 1st segment is higher than that on the downstream segments. Also, a fraction of neutral wire current flows into the grounding rod in each segment. The 1st segment experiences the highest ratio, i.e., the 1st and 2nd segments have the worst situation in terms of neutral wire current difference. This highest ratio is about 7.5% for this study case. It can be concluded that the neutral wire currents on the first several segments may experience some differences that may not always be negligibly small. As a result, this phenomenon is further investigated and understood from analytical studies in the following.

Since the two power sources in the neutral network of Figure B1 may have no fixed relationship in magnitudes or phase angles, the network is decomposed into two individual networks with one power source shown in Figures B2(a) and B2(b) according to the superposition theory. The neutral currents caused by each source are analyzed separately and then in a combined manner with the focus on the 1st segment (i.e., the worst situation) based on the equivalent networks presented in Figures B3(c) and B3(d). Such equivalent networks are transformed from Figures B2(a) and B2(b), respectively.

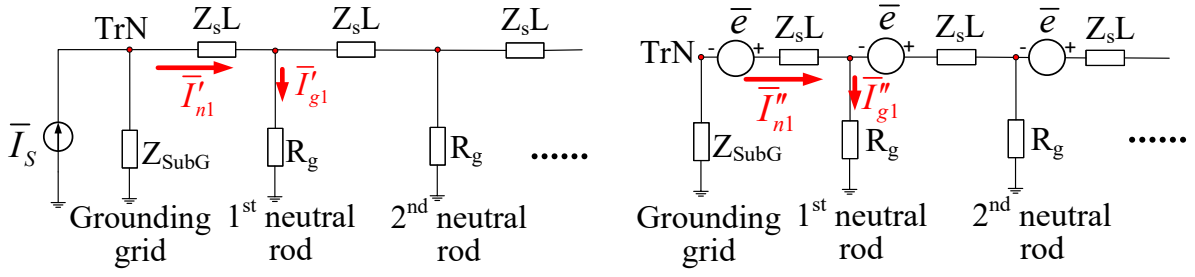

(a) Decomposed network for current injection $\bar{I}_S$ (b) Decomposed network for induced voltage $\bar{e}$

Figure B2 Decomposed networks of the multi-grounded neutral

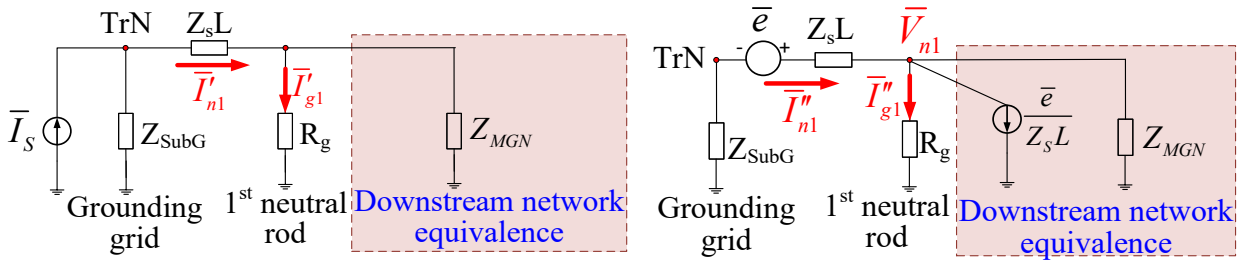

(a) Equivalent network for current injection $\bar{I}_S$ (b) Equivalent network for induced voltage $\bar{e}$

Figure B3 Equivalent networks of the multi-grounded neutral for analyzing the 1st segment

- Characteristics of the contribution of current injection $\bar{I}_S$

For the current injection $\bar{I}_S$, it is a straightforward process to obtain the current relationships from Figure B3(a) as follows:

$$\bar{I}'_{n1} = -\frac{Z_{SubG}}{Z_{SubG} + Z_s L + R_g \,\|\, Z_{MGN}} \bar{I}_S = -\frac{Z_{SubG}}{Z_{SubG} + \sqrt{Z_s L R_g}} \bar{I}_S \tag{B1}$$

$$\bar{I}'_{g1} = \frac{Z_{MGN}}{Z_{MGN} + R_g} \bar{I}'_{n1} = -\frac{\sqrt{Z_s L}}{\sqrt{Z_s L} + \sqrt{R_g}} \frac{Z_{SubG}}{Z_{SubG} + \sqrt{Z_s L R_g}} \bar{I}_S \tag{B2}$$

$$\left|\frac{\bar{I}'_{g1}}{\bar{I}'_{n1}}\right| = \left|\frac{\sqrt{Z_s L}}{\sqrt{Z_s L} + \sqrt{R_g}}\right| < \sqrt{\frac{Z_s L}{R_g}} \tag{B3}$$

where the symbol "||" means the two components are in parallel. $Z_s L + R_g \,\|\, Z_{MGN} = Z_{MGN}$ and $Z_{MGN} \cong \sqrt{Z_s L R_g}$ when the neutral is sufficiently long.

One can see from equation (B1) that the neutral wire current $\bar{I}'_{n1}$ accounts for a fraction of the current injection $\bar{I}_S$ as the injected current primarily flows into the substation grounding grid with a small Z_{SubG}. This fraction (i.e., $|\bar{I}'_{n1}/\bar{I}_S|$) is typically less than 15% for various neutrals, and it decreases with the increase of R_g and L of the neutral. For example, $|\bar{I}'_{n1}/\bar{I}_S| = 12.6\%$ when $R_g = 5\Omega$ and $L = 75m$, and $|\bar{I}'_{n1}/\bar{I}_S| = 4.3\%$ when $R_g = 25\Omega$ and $L = 150m$. Moreover, the ratio of $|\bar{I}'_{g1}/\bar{I}'_{n1}|$ in equation (B3) is in a typical range of 10%~25% for various neutrals,

independent of the current $\bar{I}_S$. Hence, one can conclude that the current injection $\bar{I}_S$ is a significant influencing factor on the neutral wire current differences among the first several segments.

- Characteristics of the contribution of induced voltage $\bar{e}$

For the induced voltage $\bar{e}$ at the 3rd harmonics in Figure B3(b), one can have the nodal voltage equation for the node above the 1st neutral rod as follows:

$$\left(\frac{1}{Z_{SubG}+Z_sL}+\frac{1}{R_g}+\frac{1}{Z_{MGN}}\right)\bar{V}_{n1}=\frac{\bar{e}}{Z_{SubG}+Z_sL}-\frac{\bar{e}}{Z_sL} \tag{B4}$$

The voltage can be calculated as

$$\bar{V}_{n1}=-\frac{Z_{SubG}R_gZ_{MGN}}{\left[\left(Z_{SubG}+Z_sL+R_g\right)Z_{MGN}+\left(Z_{SubG}+Z_sL\right)R_g\right]Z_sL}\cdot\bar{e} \tag{B5}$$

Consequently, the current relationships in Figure B3(b) can be determined as follows:

$$\begin{aligned}\bar{I}''_{n1}&=-\frac{\bar{V}_{n1}-\bar{e}}{Z_{SubG}+Z_sL}\\&=\frac{\left[\left(Z_{SubG}+Z_sL+R_g\right)Z_{MGN}+\left(Z_{SubG}+Z_sL\right)R_g\right]Z_sL+Z_{SubG}R_gZ_{MGN}}{\left(Z_{SubG}+Z_sL+R_g\right)Z_{MGN}+\left(Z_{SubG}+Z_sL\right)R_g}\frac{1}{\left(Z_{SubG}+Z_sL\right)Z_sL}\bar{e}\end{aligned} \tag{B6}$$

$$\bar{I}''_{g1}=\frac{\bar{V}_{n1}}{R_g}=-\frac{Z_{SubG}Z_{MGN}}{\left(Z_{SubG}+Z_sL+R_g\right)Z_{MGN}+\left(Z_{SubG}+Z_sL\right)R_g}\frac{1}{Z_sL}\bar{e} \tag{B7}$$

$$\left|\frac{\bar{I}''_{g1}}{\bar{I}''_{n1}}\right|=\left|\frac{-Z_{SubG}}{Z_SL+R_g+\sqrt{Z_SLR_g}}\right|<\frac{Z_{SubG}}{R_g} \tag{B8}$$

One can see from equation (B8) that the ratio of $\left|\bar{I}''_{g1}/\bar{I}''_{n1}\right|$ is always less than Z_{SubG}/R_g. The ratio is relatively small in a typical range of less than 2%. For example, $\left|\bar{I}''_{g1}/\bar{I}''_{n1}\right|$<1% when $R_g=$

15Ω and $Z_{grid} = 0.15\Omega$. This ratio is independent of the induced voltage $\bar{e}$ and the neutral currents $\bar{I}''_{n1}$ and $\bar{I}''_{g1}$. It decreases with the increase of R_g and L of the neutral. Hence, one can conclude that the induced voltage $\bar{e}$ is an insignificant influencing factor on the neutral wire current differences among the first several segments.

The analytical study results of the case shown in Figure B1 are presented in Table B2. They are almost the same as the simulation results, which prove the correctness of the analytical studies.

Table B2 Analytical study results of the currents in the 1st segment of the study case (Unit: p.u.)

Analytical Study Results			Simulation Results
$\bar{I}'_{n1}$=0.0634∠143.72°	$\bar{I}''_{n1}$=0.0559∠−162.40°	$\bar{I}_{n1} = \bar{I}'_{n1} + \bar{I}''_{n1}$ =1.065∠168.83°	$\bar{I}_{n1}$=0.1065∠168.77°
$\bar{I}'_{g1}$=0.0085∠177.49°	$\bar{I}''_{g1}$=0.0005∠12.82°	$\bar{I}_{g1} = \bar{I}'_{g1} + \bar{I}''_{g1}$ =0.0080∠176.55°	$\bar{I}_{g1}$=0.0080∠176.56°

- Characteristics of the combined contribution of current injection $\bar{I}_S$ and induced voltage $\bar{e}$

Under the contributions of both sources of $\bar{I}_S$ and $\bar{e}$, the currents in the 1st segment are as follows:

$$\begin{aligned}\bar{I}_{n1} &= \bar{I}'_{n1} + \bar{I}''_{n1} \\ &= -\frac{Z_{SubG}}{Z_{SubG} + \sqrt{Z_s L R_g}}\bar{I}_S + \frac{\left(Z_{SubG} + Z_s L + R_g\right)Z_s L + \left(Z_{SubG} + Z_s L\right)\sqrt{Z_s L R_g} + Z_{SubG} R_g}{\left(Z_{SubG} + Z_s L + R_g\right)\sqrt{Z_s L} + \left(Z_{SubG} + Z_s L\right)\sqrt{R_g}} \frac{1}{\left(Z_{SubG} + Z_s L\right)\sqrt{Z_s L}}\bar{e}\end{aligned} \tag{B9}$$

$$\begin{aligned}\bar{I}_{g1} &= \bar{I}'_{g1} + \bar{I}''_{g1} \\ &= -\frac{\sqrt{Z_s L}}{\sqrt{Z_s L} + \sqrt{R_g}} \frac{Z_{SubG}}{Z_{SubG} + \sqrt{Z_s L R_g}}\bar{I}_S - \frac{Z_{SubG}}{\left(Z_{SubG} + Z_s L + R_g\right) + \left(Z_{SubG} + Z_s L\right)\sqrt{R_g}} \frac{1}{\sqrt{Z_s L}}\bar{e}\end{aligned} \tag{B10}$$

Substituting equations (B9) and (B10) into the following equation (B11), one can determine the ratio of the neutral wire current difference between the 1st and 2nd segments. The results of equation

(B11) for the induced voltage $\bar{e}$ in various magnitudes and phase angles with respect to the current injection $\bar{I}_S = 1\angle 0°$ p.u. are shown in Figure B4.

$$\left|\frac{\bar{I}_{n1}-\bar{I}_{n2}}{\bar{I}_{n1}}\right| = \left|\frac{\bar{I}_{g1}}{\bar{I}_{n1}}\right| = \left|\frac{\bar{I}'_{g1}+\bar{I}''_{g1}}{\bar{I}'_{n1}+\bar{I}''_{n1}}\right| = \left|\frac{\mathrm{A}\cdot\bar{I}_S+\mathrm{B}\cdot\bar{e}}{\mathrm{C}\cdot\bar{I}_S+\mathrm{D}\cdot\bar{e}}\right| \tag{B11}$$

where

$$\mathrm{A} = -\frac{\sqrt{Z_s L}}{\sqrt{Z_s L}+\sqrt{R_g}}\cdot\frac{Z_{SubG}}{Z_{SubG}+\sqrt{Z_s L R_g}};$$

$$\mathrm{B} = -\frac{Z_{SubG}}{\left(Z_{SubG}+Z_s L+R_g\right)+\left(Z_{SubG}+Z_s L\right)\sqrt{R_g}}\cdot\frac{1}{\sqrt{Z_s L}};$$

$$\mathrm{C} = -\frac{Z_{SubG}}{Z_{SubG}+\sqrt{Z_s L R_g}};$$

$$\mathrm{D} = \frac{\left(Z_{SubG}+Z_s L+R_g\right)Z_s L+\left(Z_{SubG}+Z_s L\right)\sqrt{Z_s L R_g}+Z_{SubG}R_g}{\left(Z_{SubG}+Z_s L+R_g\right)\sqrt{Z_s L}+\left(Z_{SubG}+Z_s L\right)\sqrt{R_g}}\cdot\frac{1}{\left(Z_{SubG}+Z_s L\right)\sqrt{Z_s L}}.$$

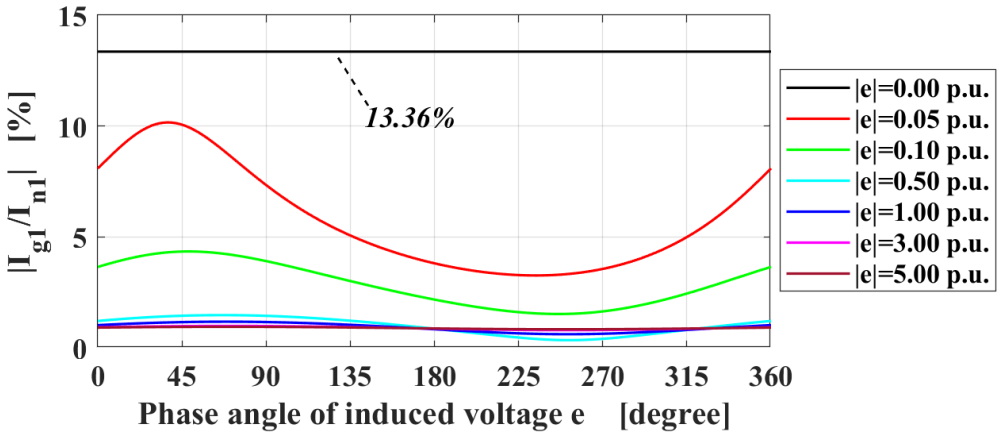

Figure B4 Ratio of $\left|\bar{I}_{g1}/\bar{I}_{n1}\right|$ for the induced voltage $\bar{e}$ in various magnitudes and phase angles

It can be seen from Figure B4 that the increase of $|\bar{e}|$ regardless of the phase angle can reduce the ratio of $|\bar{I}_{g1}/\bar{I}_{n1}|$, i.e., the neutral wire current difference between the 1st and 2nd segments. The minimum ratio of $|\bar{I}_{g1}/\bar{I}_{n1}|$ may be negligible, calculated at less than 1% for this study case. On the other hand, the ratio of $|\bar{I}_{g1}/\bar{I}_{n1}|$ reaches the maximum (13.36% for this study case) when $|\bar{e}| = 0$p.u., i.e., there are no 3rd harmonic EMFs on the neutral but a comparatively large current injection $\bar{I}_S$. The maximum ratio is governed by equation (B3), and it decreases with the increase of the neutral's grounding resistance R_g or with the decrease of the neutral's span length L.

One can conclude that large variations of $|\bar{I}_{g1}/\bar{I}_{n1}|$ may be expected for time-variant 3rd harmonic currents in power systems and different feeder neutrals in various parameters. Consequently, the unequal neutral currents on these adjacent spans within the measuring wires may not always be too small and negligible to affect the multiwire technique's performance of inductive interference reduction.

Appendix C: List of Publications

The following is a list of publications by the author during doctoral studies.

X. Wang, T. Ding, and W. Xu, "An open conductor condition monitoring scheme using natural voltage and current disturbances," *IEEE Transactions on Power Delivery*, vol. 34, no. 3, pp. 1193-1202, Jun. 2019.

X. Wang, and W. Xu, "A 3rd harmonic power based open conductor detection scheme," *IEEE Transactions on Power Delivery*, vol. 36, no. 2, pp. 1041-1050, Apr. 2021.

X. Wang, J. Yong, and L. Li, "Investigation on the implementation of the single-sheath bonding method for power cables," *IEEE Transactions on Power Delivery*, vol. 37, no. 2, pp. 1171-1179, Apr. 2022.

X. Wang, J. Yong, and W. Xu, "An online method for monitoring substation grounding grid impedances - Part I: Methodology," *IEEE Transactions on Power Delivery*, Accepted for publication.

X. Wang, J. Yong, and W. Xu, "An online method for monitoring substation grounding grid impedances - Part II: Verifications and applications," *IEEE Transactions on Power Delivery*, Accepted for publication.